



Universitat Autònoma de Barcelona

ADVERTIMENT. L'accés als continguts d'aquesta tesi doctoral i la seva utilització ha de respectar els drets de la persona autora. Pot ser utilitzada per a consulta o estudi personal, així com en activitats o materials d'investigació i docència en els termes establerts a l'art. 32 del Text Refós de la Llei de Propietat Intel·lectual (RDL 1/1996). Per altres utilitzacions es requereix l'autorització prèvia i expressa de la persona autora. En qualsevol cas, en la utilització dels seus continguts caldrà indicar de forma clara el nom i cognoms de la persona autora i el títol de la tesi doctoral. No s'autoritza la seva reproducció o altres formes d'explotació efectuades amb finalitats de lucre ni la seva comunicació pública des d'un lloc aliè al servei TDX. Tampoc s'autoritza la presentació del seu contingut en una finestra o marc aliè a TDX (framing). Aquesta reserva de drets afecta tant als continguts de la tesi com als seus resums i índexs.

ADVERTENCIA. El acceso a los contenidos de esta tesis doctoral y su utilización debe respetar los derechos de la persona autora. Puede ser utilizada para consulta o estudio personal, así como en actividades o materiales de investigación y docencia en los términos establecidos en el art. 32 del Texto Refundido de la Ley de Propiedad Intelectual (RDL 1/1996). Para otros usos se requiere la autorización previa y expresa de la persona autora. En cualquier caso, en la utilización de sus contenidos se deberá indicar de forma clara el nombre y apellidos de la persona autora y el título de la tesis doctoral. No se autoriza su reproducción u otras formas de explotación efectuadas con fines lucrativos ni su comunicación pública desde un sitio ajeno al servicio TDR. Tampoco se autoriza la presentación de su contenido en una ventana o marco ajeno a TDR (framing). Esta reserva de derechos afecta tanto al contenido de la tesis como a sus resúmenes e índices.

WARNING. The access to the contents of this doctoral thesis and its use must respect the rights of the author. It can be used for reference or private study, as well as research and learning activities or materials in the terms established by the 32nd article of the Spanish Consolidated Copyright Act (RDL 1/1996). Express and previous authorization of the author is required for any other uses. In any case, when using its content, full name of the author and title of the thesis must be clearly indicated. Reproduction or other forms of for profit use or public communication from outside TDX service is not allowed. Presentation of its content in a window or frame external to TDX (framing) is not authorized either. These rights affect both the content of the thesis and its abstracts and indexes.



Universitat Autònoma of Barcelona
Postgraduate School
Physics Department

DOCTORAL THESIS

Mechanical and electromechanical properties
of ferroelectrics at the nanoscale studied by
Atomic Force Microscopy

submitted by:

Christina Stefani

*to apply for the Degree of DOCTOR OF PHILOSOPHY
at the UNIVERSITAT AUTONÒMA OF BARCELONA
in the PHYSICS PROGRAM*

Supervisor:

Neus Domingo Marimon

Tutor:

Jordi Sort Viñas

co-Supervisor:

Gustau Catalan Bernabe

*prepared in the OXIDE NANOPHYSICS GROUP
at the INSTITUT DE CATALÀ DE NANOCIÈCIA I NANOTECNOLOGIA (ICN2)*

April 9, 2022

The research work of this PhD thesis has been funded from the PREBIST Grant (European Union's Horizon 2020 research and innovation program under the Marie Skłodowska-Curie grant agreement No. 754558).

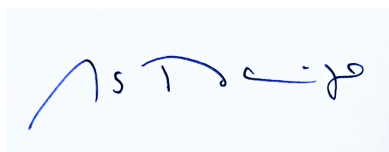
Bellaterra, 8 de abril del 2022

Dra. Neus Domingo Marimon, Prof. Gustau Catalan Bernabe, Profesor ICREA, ambos miembros del grupo **Oxide Nanophysics** en el **Institut Català de Nanociència i Nanotecnologia (ICN2)**, en calidad de directores de tesis y Prof. Jordi Sort Viñas, catedrático de la **Universitat Autònoma de Barcelona**, en calidad de tutor de tesis.

CERTIFICAN:

Que Christina Stefani, Bachiller en Física, ha realizado bajo su direccion el trabajo que lleva por titulo "*Mechanical and electromechanical properties of ferroelectrics at the nanoscale studied by Atomic Force Microscopy*". Dicho trabajo ha sido desarrollado dentro del programa de doctorado de Física y constituye su memoria de tesis doctoral, para optar por al grado de Doctor por la Universitat Autònoma de Barcelona.

Dra. Neus Domingo Marimon



Prof. Gustau Catalan Bernabe



Prof. Jordi Sort Viñas



Resumen

La microscopía de fuerza de piezorespuesta (PFM) es una poderosa herramienta para la caracterización electromecánica de materiales ferroeléctricos. En este modo de microscopía de fuerza atómica (AFM), un voltaje de CA externo excita la muestra y se mide su respuesta piezoeléctrica, proporcionando información sobre la magnitud, la orientación y el signo de la polarización ferroeléctrica. Sin embargo, como nuestro en esta tesis, la señal de frecuencia de resonancia de contacto de PFM no depende solo de las propiedades electromecánicas de los ferroeléctricos, sino que también se ve afectada por las propiedades mecánicas del material a nanoescala. La investigación desarrollada en esta tesis se centra en la identificación y cuantificación de la respuesta mecánica de materiales ferroeléctricos y su contribución en la respuesta electromecánica total.

Esta tesis muestra cómo la respuesta mecánica de los ferroeléctricos puede ser detectada y cuantificada de forma no destructiva utilizando Microscopía de Frecuencia de Resonancia de Contacto (CR-AFM). Esta técnica se ha utilizado para cuantificar la respuesta mecánica de los dominios, que depende tanto de la orientación como del signo de su polarización. Esta asimetría mecánica entre dominios de polarización opuesta permite el concepto de lectura mecánica de la polarización ferroeléctrica. Además de los dominios ferroeléctricos, también se investigaron las paredes de dominio. Las propiedades mecánicas de las paredes del dominio ferroeléctrico de 180° resultan ser claramente diferentes “más suaves” que los dominios adyacentes.

Después de haber medido las propiedades mecánicas tanto de los dominios ferroeléctricos como de las paredes del dominio utilizando CR-AFM, se implementó la técnica de excitación de banda de AFM para comparar las mediciones mecánicas y electromecánicas en materiales ferroeléctricos. Los resultados muestran que la señal de frecuencia de resonancia de contacto de las mediciones de PFM se puede utilizar para extraer información sobre la respuesta puramente mecánica de los materiales ferroeléctricos, concluyendo que es posible medir las propiedades mecánicas de los ferroeléctricos a través de mediciones electromecánicas.

La estructura de ésta tesis es la siguiente:

El Capítulo 1 es una introducción a la física de los materiales ferroeléctricos, así como a los fenómenos físicos que afectan la respuesta mecánica y electromecánica de estos materiales a la nanoescala. El Capítulo 2 describe los métodos experimentales utilizados en esta tesis. Presenta

el principio de operación de la microscopía de fuerza atómica y describe todos los modos AFM utilizados. Además, este capítulo describe el modelo analítico utilizado para cuantificar los resultados de las mediciones mecánicas basadas en CR-AFM.

La caracterización mecánica de los dominios ferroeléctricos se muestra en el Capítulo 3. En este capítulo, se demuestra que los dominios con la polarización fuera del plano con signo opuesto tienen una respuesta nanomecánica diferente, siendo los dominios con la polarización hacia arriba siempre mecánicamente más suaves que los dominios con la polarización hacia abajo. Este contraste surge del acoplamiento de flexoelectricidad y piezoelectricidad. Mi estudio se ha realizado en diferentes muestras ferroeléctricas, desde monocristales hasta películas delgadas de diferentes materiales, lo que lleva a tres resultados significativos: en primer lugar, que el efecto parece ser universal; en segundo lugar, que es posible utilizarlo para leer mecánicamente la polarización ferroeléctrica de forma no destructiva y, finalmente, que la respuesta nanomecánica de los dominios ferroeléctricos opuestos depende del espesor de la película.

El capítulo 4 es un estudio extenso de las propiedades mecánicas de las paredes del dominio ferroeléctrico. Usando CR-AFM, se muestra que las paredes de dominio ferroeléctricas de 180° tienen una respuesta nanomecánica diferente a la de los dominios. El efecto se ha vuelto a observar en diferentes materiales ferroeléctricos (LiNbO_3 , BaTiO_3 y PbTiO_3) y con diferentes morfologías (desde monocristales hasta películas delgadas), lo que sugiere su universalidad. Además, las mediciones no destructivas basadas en AFM han permitido cuantificar las propiedades mecánicas en las paredes del dominio. El capítulo también presenta un marco teórico que identifica dos mecanismos diferentes y complementarios que contribuyen a la respuesta mecánica de las paredes del dominio. Estos mecanismos son intrínsecos y, por lo tanto, el ablandamiento mecánico debería ser común a las paredes de dominio de todos los ferroeléctricos.

El Capítulo 5 analiza la contribución de las propiedades mecánicas a la respuesta electromecánica de los ferroeléctricos. Se utiliza la técnica de excitación de banda de AFM para investigar la diferencia en la frecuencia de resonancia de contacto entre la caracterización electromecánica y mecánica del material. En este capítulo mostramos que las propiedades mecánicas de los ferroeléctricos se pueden extraer de las mediciones electromecánicas.

Finalmente, esta tesis se concluye en el Capítulo 6 con un resumen de los resultados.

Abstract

Piezoresponse force microscopy (PFM) is a powerful tool for the electromechanical characterization of ferroelectric materials. In this atomic force microscopy (AFM) mode, an external *ac* voltage excites the sample and its piezoelectric response is measured, providing information about the magnitude, orientation and sign of ferroelectric polarization. However, as I show in this thesis, the PFM contact resonance frequency signal does not depend only on the electromechanical properties of ferroelectrics, but is also affected by the mechanical properties of the material at the nanoscale. The research developed in this thesis focuses on the identification and quantification of mechanical response of ferroelectric materials and their contribution on the total electromechanical response.

This thesis shows how the mechanical response of ferroelectrics can be detected and quantified in a non-destructive way using Contact Resonance Atomic Force Microscopy (CR-AFM). This technique has been used to quantify the mechanical response of domains, which depends both on the orientation and on the sign of their polarization. This mechanical asymmetry between oppositely-polarized domains enables the concept of mechanical reading of ferroelectric polarization. In addition to ferroelectric domains, domain walls were also investigated. The mechanical properties of 180° ferroelectric domain walls are found to be distinctly different -softer- than the adjacent domains.

After having measured the mechanical properties both of ferroelectric domains and domain walls using CR-AFM, Band Excitation AFM techniques are used to compare mechanical and electromechanical measurements on ferroelectric materials. The results show that the contact resonance frequency signal of PFM measurements can be used to extract information about the purely mechanical response of ferroelectric materials, concluding that it is possible to distinguish mechanical properties of ferroelectrics through electromechanical measurements.

The structure of the thesis is as follows:

Chapter 1 is an introduction on the physics of ferroelectric materials, as well as on the physical phenomena affecting the mechanical and electromechanical response of ferroelectric materials at the nanoscale. Chapter 2 describes the experimental methods used in this thesis. Introduces the principal operation of Atomic Force Microscopy and describes all AFM modes used. Additionally, this chapter describes the analytical model used to quantify the results of

mechanical measurements based on CR-AFM.

The mechanical characterization of ferroelectric domains is shown on Chapter 3. In this chapter, it is demonstrated that out-of-plane polarized domains of opposite sign have different nanomechanical response, with up-polarized ferroelectric domains being always mechanically softer than down-polarized domains. This contrast arises from the coupling of flexoelectricity and piezoelectricity. My study has been done on different ferroelectric samples, from bulk single crystals to thin films of different materials, leading to three significant results: firstly, that the effect seems to be universal; secondly, that it is possible to exploit it to mechanically read the ferroelectric polarization in a non-destructive way, and, finally, that the nanomechanical response of opposite ferroelectric domains depends on the thickness of the film.

Chapter 4 is an extensive study of the mechanical properties of ferroelectric domain walls. Using CR-AFM, it is shown that 180° ferroelectric domain walls have nanomechanical response different from the domains. The effect has again been observed in different ferroelectric materials (LiNbO_3 , BaTiO_3 and PbTiO_3) and with different morphologies (from single crystals to thin films), suggesting its universality. In addition, the non-destructive AFM-based measurements have enabled quantifying the mechanical properties on domain walls. The chapter also presents a theoretical framework that identifies two different and complementary mechanisms contributing to the mechanical response of domain walls. These mechanisms are both intrinsic and therefore mechanical softening should be common to the domain walls of all ferroelectrics.

Chapter 5 analyses the contribution of mechanical properties to the electromechanical response of ferroelectrics. Band-excitation AFM techniques are used to investigate the difference in contact resonance frequency between electromechanical and mechanical characterization of the material. In this chapter I show that the mechanical properties of ferroelectrics can be extracted from electromechanical measurements.

Finally, this thesis is concluded in Chapter 6 with a summary of the results.

Contents

Resumen	i
Abstract	iii
Table of contents	v
List of figures	vii
1 Introduction	1
1.1 Piezoelectricity	2
1.2 Ferroelectricity	4
1.2.1 Origin of ferroelectricity	5
1.2.2 Hysteresis loops of ferroelectric materials	6
1.2.3 Ferroelectric domains and domain walls	7
1.2.4 Applications of ferroelectric materials	9
1.3 Flexoelectricity	9
1.4 Mechanical properties	11
1.4.1 Mechanical properties of ferroelectric materials	13
2 Experimental Methods	19
2.1 Atomic Force Microscopy	20
2.1.1 Basic components of an AFM	20
2.1.2 Operation modes of an AFM	23
2.2 Piezoresponse Force Microscopy	24
2.2.1 Operating principle	24
2.2.2 Lateral and Vertical PFM	25
2.2.3 DART PFM	25
2.2.4 Band Excitation PFM	26
2.2.5 Spectroscopy Switching PFM	27
2.3 Contact Kelvin Force Probe Microscopy	28
2.4 Contact Resonance Atomic Force Microscopy	30
3 Mechanical Properties of Ferroelectric Domains	37
3.1 Asymmetry in the mechanical properties of ferroelectric materials under inhomogeneous deformation	39
3.2 AFM tip induced strain gradients	41
3.3 Mechanical reading of ferroelectric polarization	44
3.3.1 Mechanical reading of ferroelectric polarization in BaTiO ₃ single crystals	44
3.3.2 Mechanical reading of ferroelectric polarization in BiFeO ₃ thin films	49
3.3.3 Mechanical reading of ferroelectric polarization in PbTiO ₃ thin films	54

3.3.4	Advantages of mechanical reading of ferroelectric polarization by CR-AFM	59
3.4	Size dependence of mechanical reading	59
3.4.1	Mechanical reading of ferroelectric polarization in PbTiO ₃ thin films as a function of thickness	62
4	Mechanical Properties of Ferroelectric Domain Walls	73
4.1	Ferroelectric domain walls	74
4.2	Experiments on domain wall elasticity	74
4.2.1	180° Domain Walls of LiNbO ₃ single crystal	75
4.2.2	180° Domain Walls of PbTiO ₃ thin films	78
4.2.3	180° Domain Walls of BaTiO ₃	81
4.3	Quantification of domain wall elasticity	84
4.4	The origin of domain wall softening	87
4.4.1	Domain wall softening due to different factors	87
4.4.2	Dynamic model for domain wall softening	90
4.4.3	Static model for domain wall softening	92
5	Mechanical Properties from Electromechanical Measurements	103
5.1	Electromechanical measurements of BaTiO ₃ single crystal	105
5.1.1	DART PFM and Band Excitation PFM on BaTiO ₃ Single Crystal	105
5.1.2	Data analysis of Band Excitation PFM measurements	107
5.1.3	Data analysis of Band Excitation by k-means clustering	108
5.2	Mechanical measurements of BaTiO ₃ single crystal	113
5.2.1	Band Excitation CR-AFM on BaTiO ₃ Single Crystal	113
5.2.2	Data analysis of Band Excitation CR-AFM measurements	115
5.3	Quantification of CR-AFM results	116
5.3.1	Calibration of the experimental factors	117
5.3.2	Antisymmetric flexoelectric coupling with ferroelectric polarization	121
5.3.3	Domain wall contribution of sub-resolution bubble domains	122
5.4	Comparison of Band Excitation PFM and CR-AFM	124
5.4.1	Contact KPFM on BaTiO ₃ Single Crystal	127
5.4.2	Calculation of the piezoelectric coefficient of BaTiO ₃ Single Crystal	130
5.5	Decoupling of mechanical, electrostatic and piezoelectric properties from electromechanical responses at the nanoscale	131
6	Conclusions	135
A	Quantification of tip-sample mechanical coupling	139
A.1	General equation of motion	139
A.2	Contact forces	142
A.3	Characteristic equation	144
B	Influence of cantilever stiffness on mechanical reading	151

List of Figures

1.1	Direct and converse piezoelectric effect diagram	2
1.2	Piezo-Pyro-Ferro relationship	3
1.3	Scheme dielectric - paraelectric - ferroelectric	5
1.4	Schematic representation of BaTiO ₃ unit cell	5
1.5	Ferroelectric hysteresis loop	6
1.6	Types of ferroelectric domain walls	8
1.7	Sketch of homogeneous and inhomogeneous deformation	9
1.8	Typical stress-strain curve diagram	13
2.1	Schematic representation of an AFM	21
2.2	SEM images of AFM cantilever	22
2.3	Depiction of PFM	25
2.4	DART PFM operating principle	26
2.5	Band excitation operating principle	27
2.6	PFM hysteresis loop	28
2.7	Scheme of voltage applied by the tip on cKPFM measurements	29
2.8	Scheme of CR-AFM mode	31
3.1	Flexoelectric field induced by AFM tip	41
3.2	Flexoelectric field induced by an AFM tip in contact with the sample	43
3.3	Electromechanical characterization of BaTiO ₃ single crystal in an area of 20x20 μ m	45
3.4	Electromechanical characterization of BaTiO ₃ single crystal in an area of 7x7 μ m	46
3.5	PFM phase and CR-AFM of BaTiO ₃ single crystal	47
3.6	Electromechanical characterization of BaTiO ₃ single crystal in an area of 2.7x2.7 μ m	48
3.7	PFM hysteresis loop of BiFeO ₃ (111)/LSMO/STO thin film	51
3.8	Electromechanical characterization of BiFeO ₃ (111)/LSMO/STO thin film	52
3.9	Electromechanical characterization of BiFeO ₃ thin film with domains opposite polarized out-of-plane.	53
3.10	PFM hysteresis loop of PbTiO ₃ thin film	55
3.11	PFM characterization of PbTiO ₃ thin film	56
3.12	Electromechanical characterization of PbTiO ₃ thin film	57
3.13	SEM images of AFM tips	60
3.14	Mechanical reading on PbTiO ₃ thin film with a thickness of 50 nm	62
3.15	Mechanical reading on PbTiO ₃ thin film with a thickness of 20 nm	63
4.1	DART PFM on PPLN single crystal	75
4.2	CR-AFM on PPLN single crystal	77
4.3	CR-AFM on PbTiO ₃ thin film	80
4.4	CR-AFM on BaTiO ₃ single crystal	83
4.5	Schematic representation of the cantilever in contact with the sample	84

4.6	CR-AFM on BaTiO ₃ single crystal whit a-domains	89
4.7	Theoretical approach for domain walls softening	91
4.8	Modeling of strain profiles	92
4.9	Schematic of the “in-plane” mechanism of the bound charge formation	93
4.10	Static model for domain wall softening	95
5.1	Schematic representation of BaTiO ₃ (100) single crystal	105
5.2	DART PFM characterizarion on BaTiO ₃ single crystal in an area of 5x5 μm . . .	107
5.3	Band Excitation PFMcharacterizarion on BaTiO ₃ single crystal in an area of 5x5 μm	107
5.4	SHO fit of Band Excitation PFM data of BaTiO ₃ single crystal	108
5.5	Clustering maps	110
5.6	Silhouette coefficient	111
5.7	k-means clustering map of Band Excitation PFM measurement	112
5.8	Band Excitation CR-AFM measurement on BaTiO ₃ single crystal	114
5.9	Contact resonance frequency image of Band Excitation CR-AFM measurement on BaTiO ₃ single crystal.	115
5.10	Contact resonance frequency of Band Excitation PFM	125
5.11	SHO fitting of Band Excitation PFM measurements on BaTiO ₃	126
5.12	cKPFM results on BaTiO ₃	128
5.13	cKPFM map of BaTiO ₃	129
A.1	Sketch of rectangular cantilever with triangularly shaped end.	140
A.2	Schematic representation of tilted tip in contact with sample	143
B.1	CRF images of PPLN crystal	153
B.2	CRF images of of PbTiO ₃ thin film l	154

CHAPTER 1

Introduction

The focus of this thesis is on the mechanical and electromechanical response of ferroelectric materials at the nanoscale, and how mechanical and electromechanical properties are inter-related and affect each-other. This chapter introduces the general physical properties of ferroelectrics and describes the basic concepts of piezoelectricity and flexoelectricity. Finally, it introduces the mechanical properties that are being discussed throughout the thesis.

1.1 Piezoelectricity

Piezoelectric materials generate an electric charge when subjected to mechanical stress, and the other way around, they can be deformed by the application of an electric field. The piezoelectric effect is thus a reversible process, meaning that materials that exhibit voltage as a result of mechanical stress, also internally generate a mechanical strain resulting from an applied electric field (converse piezoelectric effect). Direct and converse piezoelectric effects are shown schematically in **Figure 1.1**.

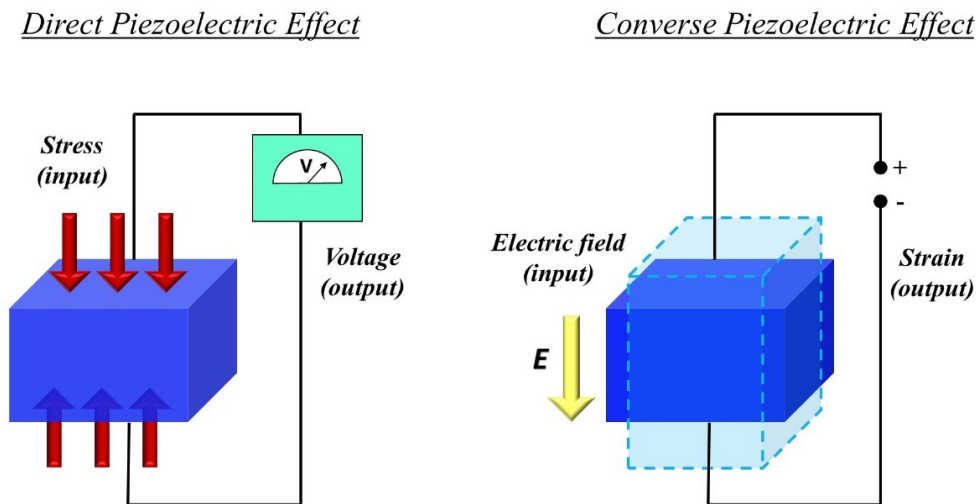


Figure 1.1: Diagram of direct and converse piezoelectric effect.

All piezoelectric materials have a non-centrosymmetric crystallographic structure. From the crystallographic perspective, crystals are classified into 32 classes, according to their point group symmetry. Only 21 of these are non-centrosymmetric, and 20 of these exhibit piezoelectric properties. 10 of these have only one unique direction axis. When such crystals display spontaneous polarization in the absence of mechanical stress in a certain temperature range, they are called polar crystals. These crystals exhibit pyroelectricity (the generation of a charge upon a thermal gradient) and when their spontaneous polarization is reversibly switchable with the application of an external electric field, they are also ferroelectrics. Consequently, all ferroelectric materials are also piezoelectric, although not all piezoelectrics are ferroelectrics. The relationship between piezoelectric, pyroelectric and ferroelectric materials is shown in **Figure 1.2**.

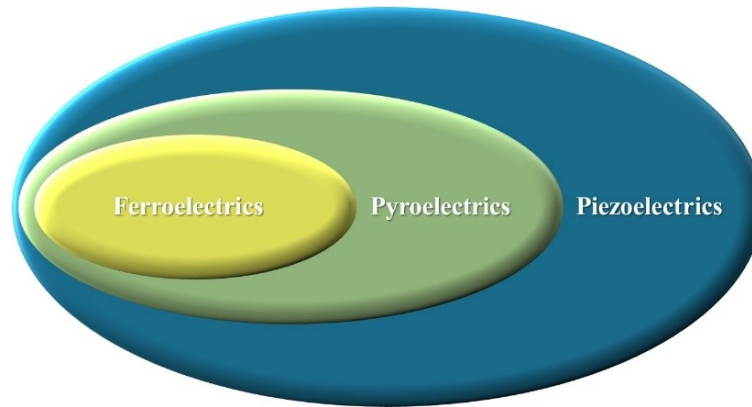


Figure 1.2: Relationship between piezoelectric, pyroelectric and ferroelectric materials.

Direct piezoelectric effect can be described by the following equation:

$$P_i = d_{ijk}\sigma_{jk} \quad (1.1)$$

where P_i is the polarization (C/m^2), d_{ijk} the direct piezoelectric coefficient (C/N), and σ_{jk} the applied stress (N/m^2). Polarization is a vector, while piezoelectric coefficient and stress are a third and a second-rank tensors respectively [1]. The subscripts refer to axis directions; i is the polar axis, parallel to the polarization vector, j is the direction of the force and k is the third direction, perpendicular to the other two.

Converse piezoelectric effect is described the following equation which correlates the strain (ε) with the electric field (E) as:

$$\varepsilon_{jk} = d_{ijk}E_k \quad (1.2)$$

The electric field vector is measured in V/m , the converse piezoelectric coefficient in m/V while the third-rank strain tensor is dimensionless. It is proven that direct piezoelectric coefficient and converse piezoelectric coefficient are equivalent. In both cases the coefficient correlates the stress and polarization and can be obtained by differentiating the same Gibbs free energy to both stress and electric field [2].

Although piezoelectricity is a third-rank tensor with $3^3 = 27$ components, only 18 are independent. The reason behind that is the symmetric behaviour of stress tensor ($\sigma_{jk} = \sigma_{kj}$), leading to a 6x3 matrix that describes the direct piezoelectric effect [2] (**Equation 1.3**). It should be mentioned that the subscripts of piezoelectric coefficient are usually expressed using the reduced Voigt matrix notation d_{im} , where i denotes the electric displacement or field ($i =$

1,2,3) and $m = 1, \dots, 6$ defines the mechanical stress or strain.

$$\begin{pmatrix} P_1 \\ P_2 \\ P_3 \end{pmatrix} = \begin{pmatrix} d_{11} & d_{12} & d_{13} & d_{14} & d_{15} & d_{16} \\ d_{21} & d_{22} & d_{23} & d_{24} & d_{25} & d_{26} \\ d_{31} & d_{32} & d_{33} & d_{34} & d_{35} & d_{36} \end{pmatrix} \begin{pmatrix} \sigma_1 \\ \sigma_2 \\ \sigma_3 \\ \sigma_4 \\ \sigma_5 \\ \sigma_6 \end{pmatrix} \quad (1.3)$$

Respectively, the converse piezoelectric effect is described by the following equation:

$$\begin{pmatrix} \varepsilon_1 \\ \varepsilon_2 \\ \varepsilon_3 \\ \varepsilon_4 \\ \varepsilon_5 \\ \varepsilon_6 \end{pmatrix} = \begin{pmatrix} d_{11} & d_{12} & d_{13} & d_{14} & d_{15} & d_{16} \\ d_{21} & d_{22} & d_{23} & d_{24} & d_{25} & d_{26} \\ d_{31} & d_{32} & d_{33} & d_{34} & d_{35} & d_{36} \end{pmatrix} \begin{pmatrix} E_1 \\ E_2 \\ E_3 \end{pmatrix} \quad (1.4)$$

The piezoelectric coefficient is being used to evaluate the piezoelectric response of a material as it correlates the electric charge per unit area under applied mechanical force [1,3]. In case the applied force is parallel to the polarization axis and is impressed on the same surface from which the charge is collected, then the corresponding component of piezoelectric coefficient is d_{33} .

1.2 Ferroelectricity

Ferroelectricity is the collective property of certain dielectric materials in the subgroup of pyroelectric materials that have spontaneous electric polarization, i.e., they naturally possess dipole moments aligned to form an electrically polarized material which can be switched with the application of an appropriate external electric field. In general, dielectric materials can be polarized by an externally applied field and the induced polarization (P_i) is linearly proportional to the applied field. The dielectric permittivity of the material is defined as the slope of the polarization curve (**Figure 1.3a**). In paraelectric materials, the proportion between polarization and external field is nonlinear (**Figure 1.3b**). The distinctive characteristic of ferroelectric

materials though, is that the induced polarization exhibits a hysteretic behaviour (**Figure 1.3c**), together with a remnant polarization at zero applied field.

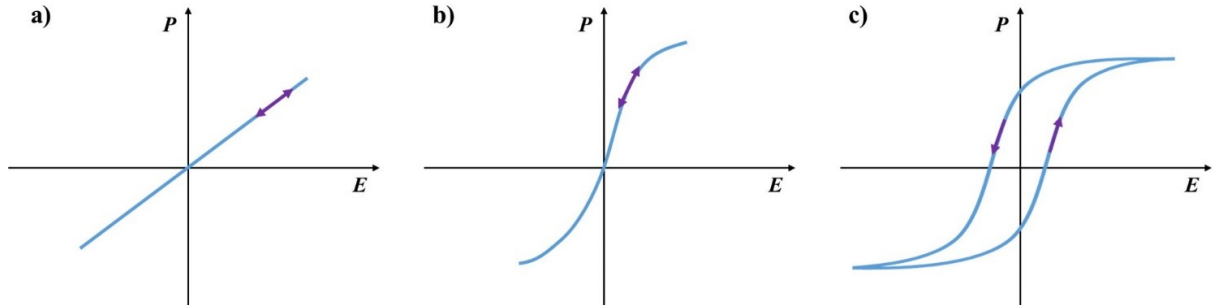


Figure 1.3: Schematic diagram of electric polarization as a function of externally applied electric field in case of dielectric (a), paraelectric (b) and ferroelectric (c) materials.

1.2.1 Origin of ferroelectricity

The structural symmetry of crystals depends on their lattice structure and affects both geometrical and physical properties of the crystal. As piezoelectric materials, its spontaneous polarization, which is the main characteristic of ferroelectrics, arises from the non-centrosymmetric structure of the lattice. In a certain range of temperatures where the crystallographic structure of the material is non-centrosymmetric, positive and negative ionic sublattices are displaced with respect to the centre of the lattice, and the centre of positive charge does not coincide with the centre of negative charge, creating electric dipoles. The collective signal of these dipoles creates the spontaneous polarization [4], which is defined as dipole moment per unit volume. Since ferroelectricity is defined by the crystal structure [5], the axis of spontaneous polarization is usually aligned to some crystal axis. To be able to visualize the asymmetry in ferroelectric crystal structure, **Figure 1.4** shows a schematic representation of the unit cell of barium titanate (BaTiO_3), an archetypal ferroelectric material.

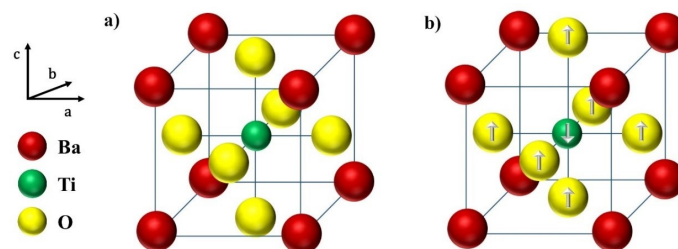


Figure 1.4: Schematic representation of BaTiO_3 unit cell in cubic structure (a) and tetragonal structure (b). Displacement of titanium along the c -axis is responsible for the ferroelectric properties of BaTiO_3 in tetragonal structure.

As a subtype of pyroelectric materials, the ferroelectric properties of crystals also depend on temperature. Ferroelectric materials have a spontaneous polarization below a certain phase transition temperature that is called Curie temperature (T_c). For temperatures higher than T_c , the crystal does not exhibit ferroelectric behaviour while at the Curie point the crystal undergoes a phase transition from paraelectric to ferroelectric phase. While it is possible that a ferroelectric material shows more than one ferroelectric phases in different temperature ranges, with different associated crystallographic structures, the Curie temperature specifies only the temperature at which a transition from paraelectric to ferroelectric phase takes place. In the case of BaTiO_3 this oxide perovskite has a cubic structure (**Figure 1.4a**) for temperatures higher than 130°C . For temperatures below the Curie temperature, the structure of BaTiO_3 becomes tetragonal (**Figure 1.4b**). Ferroelectricity in tetragonal BaTiO_3 originates from the displacement of titanium from its centrosymmetric position, along the c - axis [6].

1.2.2 Hysteresis loops of ferroelectric materials

The switching spectroscopy of the polarization of ferroelectric materials as a function of the applied electric field shows a typical ferroelectric hysteresis behaviour depicted in **Figure 1.5**.

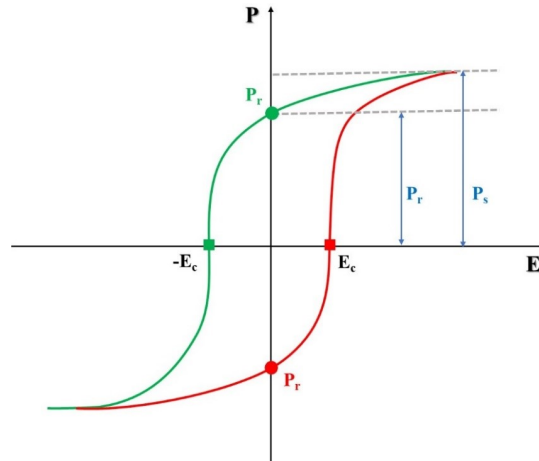


Figure 1.5: Schematic diagram of a typical hysteresis loop of ferroelectric material

When applying an electric field, the polarization of the material aligns with the external field until the point where the material cannot be further polarized (P_s : saturation polarization). As the electric field is removed, the material will be only partially misaligned. The remaining polarization is called remnant polarization (P_r). As a negative electric field is applied, the

polarization will decrease until the total polarization goes back to zero. The corresponding applied field is called coercive field (E_c). Continuing to strengthen the negative electric field, the polarization will align to the opposite direction. Repetition of this procedure leads to ferroelectric hysteresis loop which shows that polarization displays hysteresis with the external electric field.

1.2.3 Ferroelectric domains and domain walls

Uniform alignment of electric dipoles within certain regions of the ferroelectric material, thus showing a uniform ferroelectric polarization are called ferroelectric domains. Domains can be named after the crystal axis which is parallel to their ferroelectric polarization (e.g., a or c domains for tetragonal ferroelectric phases) or based on the polarization direction in comparison with the plane of the surface of the material (e.g., *in-plane* or *out-of-plane* domains).

Domains are formed in a configuration that minimizes the surface and boundary energies, as well as the sum of polarization and depolarization. Since in ferroelectric materials are areas that are uniformly polarized, that leads to accumulation of bound charges. These uncompensated bound charges, which can be on the surface or/and in the bulk of the material, generate an internal electric field that is pointed against the polarization. This electric field is called depolarization field and, in some cases, is strong enough to suppress the ferroelectric polarization. In bulk materials, the formation of domains with opposite polarization, or closure domains (domains with parallel and perpendicular polarity with a total zero polarization) is a sufficient way to screen the compensated bound charges. The surface bound charges can be screened by atmospheric adsorbates, metallic electrodes or free charges (in case of semiconducting ferroelectrics) [7–9]. Due to the need of managing depolarizing fields in ferroelectrics, boundary conditions play a significant role in the total behavior of ferroelectrics. There are two possible scenarios: close-circuit and open-circuit conditions. In close-circuited, a conductive material in contact with the ferroelectric provides free charges to the system, screening the depolarizing fields. In open-circuited systems there is no external source of free charges and accumulated bound charges can be screened only by atmospheric adsorbates or internal free charges.

The precise morphology of domains depends strongly on electrical and mechanical boundary conditions [10–13]. These restrictions, accompanied with size reduction, can also be responsible for the creation of different domain patterns, such as “bubble-like” domains [14] or even more complex configurations [15–17].

The boundaries between ferroelectric domains are called domain walls. There are different types of domain walls, based on the way the polarization direction or its magnitude alternates along them [18]. Most commonly, in ferromagnets, domain walls exhibit a gradual rotation of spins, leading to so-called Bloch or Néel type domain walls (**Figure 1.6**). In ferroelectrics though, since most ferroelectrics are also ferroelastic materials, the domain wall energy is dominated by the strong coupling between strain and polarization, and therefore polarization reversal occurs at a scale of few unit cells [19]. Commonly, these domain walls are named as a function of the angle shift of the ferroelectric polarization of the domains they separate: 180° domain walls separate antiparallel aligned domains; 71° or 109° domain walls are found in orthorhombic phases of ferroelectrics, and 90° domain walls separating a and c domains are characteristic of tetragonal ferroelectrics. Studies on 180° ferroelectric domain walls have shown that these types of walls consist of a combination of Bloch-Neél-Ising walls [20,21]. **Figure 1.6** summarizes the different configurations of the Ising, Bloch and Néel types of domain walls.

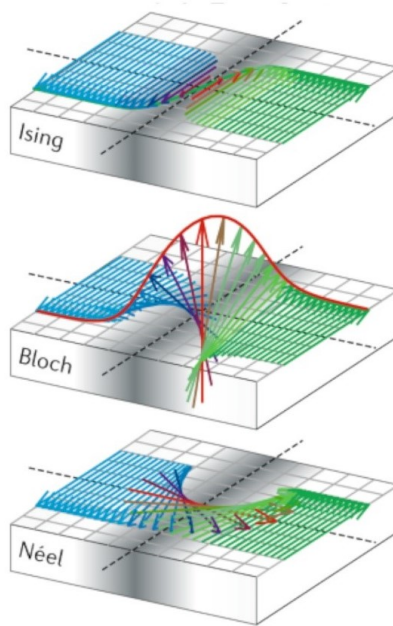


Figure 1.6: Types of ferroelectric domain walls, showing the alternation of ferroelectric polarization. Taken from [22].

Since polarization and strain are strongly coupled, any change in spontaneous polarization smaller than 180° must be associated with a change of spontaneous strain direction, called ferroelastic switching [23]. Contrarily, 180° switching does not alternate the direction of spontaneous strain. The type of domain walls studied in this thesis is 180° ferroelectric domain walls.

1.2.4 Applications of ferroelectric materials

Due to their switchable spontaneous polarization and the coupling between strain and polarization, ferroelectric materials have a wide range of technological applications. For example, ferroelectrics are used for non-volatile memories and integrated microelectronics, actuators, capacitors and many more, both in form of bulk materials or thin films [23–28]. These applications take advantage of the mechanical and electromechanical properties of ferroelectric materials. The present thesis delves into the fundamental knowledge of these properties and how they are sometimes coupled and uses advanced techniques of scanning force microscopy to study them.

1.3 Flexoelectricity

Flexoelectricity is another electrochemical property of dielectric materials whereby a spontaneous electrical polarization is induced by a strain gradient. Unlike piezoelectricity, flexoelectricity is a universal property present in all crystals, regardless of their symmetry (piezoelectricity, the coupling of polarization and strain, appears only in non-centrosymmetric crystals). Flexoelectricity can thus occur in centrosymmetric crystals as a non-uniform strain (or strain gradient) breaks the centrosymmetry. To further comprehend the mechanism of flexoelectricity, **Figure 1.7** shows the response of a centrosymmetric crystal under an applied homogeneous (strain) and inhomogeneous (strain gradient) deformation.

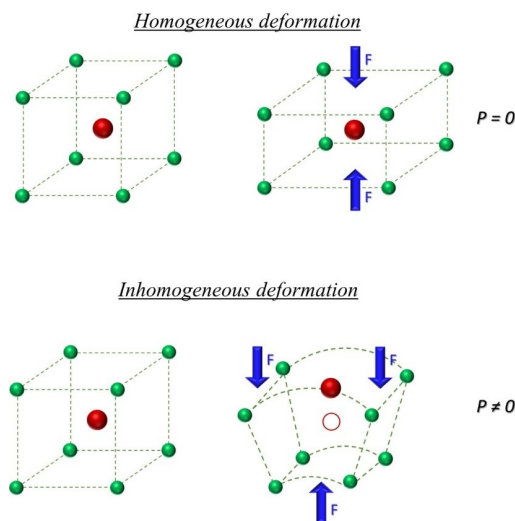


Figure 1.7: Sketch of centrosymmetric unit cell under deformation. Homogeneous deformation does not affect the symmetry while inhomogeneous deformation induces polarization.

In a centrosymmetric cell, under homogeneous deformation, the centers of positive and negative charges coincide with each other resulting to zero polarization. Under inhomogeneous deformation though, the displacement of positive and negative charges differs from each other, resulting in polarization inducing an output charge on the surfaces.

In solid dielectrics, the flexoelectric effect can be described by the following equation [29]:

$$P_i = \mu_{ijkl} \frac{\partial \varepsilon_{jk}}{\partial x_l}, \quad (1.5)$$

where P_i is the polarization, ε the strain tensor, x refers to the coordinates and μ_{ijkl} is the flexoelectric coefficient. **Equation 1.5** shows that the induced polarization is linearly proportional to strain gradient. Additionally, the flexoelectric coefficient is also linearly proportional to the dielectric susceptibility [30]:

$$\mu_{ijkl} = \chi_{ij} \gamma_{kl} \frac{e}{a}, \quad (1.6)$$

where χ_{ij} is the dielectric susceptibility, γ_{kl} a constant material parameter, e the charge of electron and a the atomic dimension of the unit cell.

Although flexoelectricity was first reported in the 60s, it did not arouse much interest in the following decades. Despite being a universal property, its small magnitude in simple dielectrics was limitative. However, almost two decades ago, studies revealed that ferroelectric materials with high dielectric permittivity could show giant flexoelectric coefficients [31–34]. These findings confirmed the linear proportionality between dielectric permittivity and flexoelectric coefficients and renewed the scientific interest on flexoelectricity.

Another advantage of flexoelectricity is that exhibits a scale effect. Strain gradients are size-dependent property that scales proportionally to size reduction, because strain gradients themselves can be larger at the nanoscale (a strain gradient ultimately is a difference in strain divided by a relaxation length, so the smaller the length the larger the gradient) Thus, since strain gradients can be huge at nanoscale, they can lead to gigantic flexoelectric phenomena [30, 35–36].

Being so, the universal character of flexoelectricity in combination with the development of nanoscale technologies have inspired a lot of novel research on the flexoelectric effect and its application in the recent decades. Indicatively, flexoelectric effect has been used for energy

harvesting [37,38], mechanical switch of ferroelectric polarization [39] or even to the flexo-photovoltaic effect, where flexoelectricity was used to enhance the photovoltaic response [40]. Finally, it is interesting to underscore that flexoelectric phenomena also show potential applications in biology and medical sciences [41–45].

1.4 Mechanical properties

The mechanical properties of materials determine how a material deforms under mechanical stress. The main mechanical properties used to describe this behaviour are elasticity, plasticity, stiffness, toughness or hardness, and are used to determine the stress level that the material can withstand and also its life expectancy. In this thesis focuses on the stiffness of materials, which is defined as the resistance of a material to elastic deformation.

Although strain and stress have been already mentioned in the introduction of this thesis, it is important to clarify their definition, as they both describe forces that cause deformation of the materials. Stress (σ) is defined as the ratio of the applied force (F) to the cross-sectional area of the material (A) [46]:

$$\sigma = \frac{F}{A} \quad (1.7)$$

Strain (ε) on the other hand can be calculated as the ratio of elongation of the material (Δl) to its initial length (l_0) due to the applied tensile force [46]:

$$\varepsilon = \frac{\Delta l}{l_0} \quad (1.8)$$

Deformation of materials can be plastic (reversible) or elastic (irreversible). When the applied load is small enough, the material deformation is maintained into the elastic region (see **Figure 1.8**), and can return to its initial form after removing the applied force. When the applied force is increased beyond the elastic limit, the materials undergo plastic deformation, which is irreversible and permanent. The critical point between elastic and plastic deformation is called yield point. After the yield point, increasing of stress leads to fracture and break down of the material.

When the deformation of the material is within the limits of elastic region, elasticity is the mechanical property that describes its behaviour. Elasticity is the ability of a deformed body to

return into its original shape and size, after the removal of the force that causes the deformation. Stress and strain are direction dependent quantities and therefore are described by tensors. The most general relationship that describes the connection between stress and strain, in the limits of elastic region where they behave linearly, is Hooke's law:

$$\sigma_{ij} = C_{ijkl}\varepsilon_{kl}, \quad (1.9)$$

where stress σ_{ij} and strain ε_{kl} tensors are related through the elastic constants C_{ijkl} . Alternatively, the relationship can be expressed as:

$$\varepsilon_{ij} = S_{ijkl}\sigma_{kl} \quad (1.10)$$

where S_{ijkl} is the elastic moduli of the material. The stiffness of materials is evaluated by the Young's modulus (E) which is known as the modulus of elasticity and measures the material's resistance to elastic deformation under mechanical load. It is defined as the ratio of stress over strain:

$$E = \frac{\sigma}{\varepsilon} = \frac{(F/A)}{(\Delta L/L_0)} \quad (1.11)$$

where F is the applied force, A is the cross-sectional surface area and L is the length of the material (L_0 is the initial length and ΔL the change in length). The Young's modulus is measured in Pa and lower values of E correspond to softer materials. Comparing **Equations 1.9-1.11** one can derive the relation between Young's modulus, elastic constants and elastic moduli.

Young's modulus also depends on the orientation of a material. Mechanical properties in isotropic materials are not orientation depended but anisotropic materials have different Young's modulus values, as a function of the direction of the applied force. Furthermore, despite Young's modulus is known as the "elastic modulus", it only describes elasticity along a line of opposing applied forces. Elasticity in bulk materials is measured by bulk modulus (K) which measures volumetric elasticity. When shear forces are applied on the material, elastic response is measured by modulus of rigidity (G) which is defined as shear stress over shear strain.

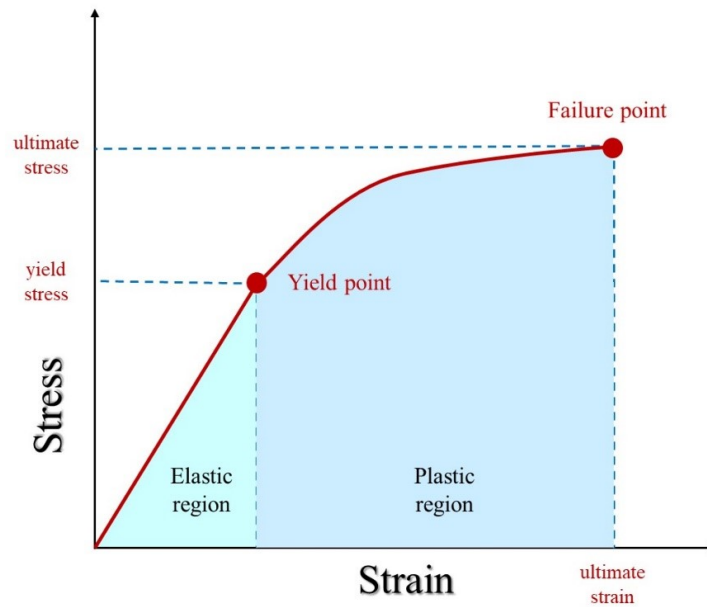


Figure 1.8: Typical diagram of stress-strain curve showing the elastic and plastic regions, as well as the yield point and the failure point of a material under mechanical force.

During this thesis, mechanical properties of ferroelectric materials are defined by Young's modulus. More specifically, the difference in nanomechanical response of materials is translated into changes of Young's modulus of the materials.

1.4.1 Mechanical properties of ferroelectric materials

This thesis focuses on the study of mechanical and electromechanical responses of ferroelectrics at the nanoscale. In ferroelectric materials, mechanical and electromechanical properties are not independent. When a ferroelectric material, which is also piezoelectric, is subjected to a mechanical stress (σ), the material is polarized due to direct piezoelectric effect. This polarization generates an electric field that is used to transform the mechanical energy into electrical energy. When a ferroelectric material is subjected to a strain (ε) (homogeneous deformation), this strain will cause two effects: initially, it will generate a stress (σ) proportional to it, as described on **Equation 1.9** and secondly, it will induce a piezoelectric polarization proportional to this stress (**Equation 1.1**). This induced polarization and the associated electric field produces a stress that is opposite to the initial stress, making the mechanical response of the material stiffer.

Another way to better understand the connection of piezoelectric phenomenon with the elastic response of the material is to consider the cost of energy under a homogeneous deformation. In

case of non-piezoelectric materials, any deformation has an associated cost of energy (U) that is described by Hooke's law:

$$U = \frac{1}{2}C\varepsilon^2 \quad (1.12)$$

where C is elastic constant and ε the applied strain. In case of piezoelectric materials though, the associated cost of energy will consist of an extra term that includes the induced piezoelectric polarization:

$$U = \frac{1}{2}C\varepsilon^2 + \frac{1}{2}\frac{P^2}{\chi} \quad (1.13)$$

where χ is the electric susceptibility. Since the second term in **Equation 1.13** is positive, then it is clear that piezoelectric phenomenon causes an increase in material's stiffness since it increases the energy needed to deform it.

Equation 1.13 shows that the energy cost of deformation depends on the induced polarization, meaning that the mechanical response of a ferroelectric material will indeed also depend on the polarization induced by the deformation. In the case of close-circuited boundary conditions (see **Section 1.1.3**), a flow of free charges between the surfaces can screen this polarization reducing its magnitude. Consequently, the induced polarization is smaller and the mechanical response of the material is softer. Oppositely, in open-circuit conditions, the induced polarization is not screened and the total mechanical response of the material is stiffer. This thesis investigates how this coupling affects nanoscale measurements in ferroelectric materials leading to new phenomena, by taking into account the dependence of mechanical and electromechanical properties.

References

- [1] A. American, N. Standard. *IEEE Standard on Piezoelectricity: An American National Standard*, ANSI/IEEE Std 176-1987 (1988).
- [2] D. Damjanovic. *Ferroelectric, dielectric and piezoelectric properties of ferroelectric thin films and ceramics*, Rep. Prog. Phys. **61**(9) (1998).
- [3] B. Jaffe, W.R. Cook, H. Jaffe. *Piezoelectric Ceramics*, 1st ed., Elsevier, 1971.
- [4] Y. Xu. *Ferroelectric Materials and Their Applications*, 1st Edition, North Holland, 1991.
- [5] M. Bachmann, W.L. Gordon, S. Weinhold, J.B. Lando. *The crystal structure of phase IV of poly(vinylidene fluoride)*, J. Appl. Phys. **51**(10) (1980).
- [6] M.B. Smith, K. Page, T. Siegrist, P.L. Redmond, E.C. Walter, R. Seshadri, L.E. Brus, M.L. Steigerwald. *Crystal Structure and the Paraelectric-to-Ferroelectric Phase Transition of Nanoscale BaTiO₃*, J. Am. Chem. Soc. **130**(22) (2008).
- [7] R. Kretschmer, K. Binder. *Surface effects on phase transitions in ferroelectrics and dipolar magnets*, Phys. Rev. B **20**(3) (1979).
- [8] V. Fridkin, S. Ducharme. *Ferroelectricity At The Nanoscale: Basics And Applications*, Springer, Heidelberg New York Dordrecht London, 2013.
- [9] C. Lichtensteiger, P. Zubko, M. Stengel, P. Aguado-Puente, J.M. Triscone, P. Ghosez, J. Junquera. *Ferroelectricity in Ultrathin-Film Capacitors*, Oxide Ultrathin Film. (2012).
- [10] T. Shimada, S. Tomoda, T. Kitamura. *Ab initio study of ferroelectric closure domains in ultrathin PbTiO₃ films*, Phys. Rev. B - Condens. Matter Mater. Phys. **81**(14) (2010).
- [11] S. Prosandeev, L. Bellaiche. *Asymmetric screening of the depolarizing field in a ferroelectric thin film*, Phys. Rev. B - Condens. Matter Mater. Phys. **75**(17) (2007).
- [12] B.K. Lai, I. Ponomareva, I. Kornev, L. Bellaiche, G. Salamo. *Thickness dependency of 180° stripe domains in ferroelectric ultrathin films: A first-principles-based study*, Appl. Phys. Lett. **91**(15) (2007).
- [13] P. Aguado-Puente, J. Junquera. *Ferromagneticlike closure domains in ferroelectric ultrathin*

- films: First-principles simulations*, Phys. Rev. Lett. **100**(17) (2008).
- [14] I. Kornev, H. Fu, L. Bellaiche. *Ultrathin films of ferroelectric solid solutions under a residual depolarizing field*, Phys. Rev. Lett. **93**(19) (2004).
- [15] S. O'Brien, L. Brus, C.B. Murray. *Synthesis of monodisperse nanoparticles of barium titanate: Toward a generalized strategy of oxide nanoparticle synthesis*, J. Am. Chem. Soc. **123**(48) (2001).
- [16] A. Schilling, D. Byrne, G. Catalan, K.G. Webber, Y.A. Genenko, G.S. Wu, J.F. Scott, J.M. Gregg. *Domains in ferroelectric nanodots*, Nano Lett. **9**(9) (2009).
- [17] C. Liu, B. Zou, A.J. Rondinone, Z.J. Zhang. *SolGel Synthesis of Free-Standing Ferroelectric Lead Zirconate Titanate Nanoparticles*, J. Am. Chem. Soc. **123**(18) (2001).
- [18] D. Meier, J. Seidel, M. Gregg, R. Ramesh. *Domain walls: From fundamental properties to nanotechnology concepts* Oxford University Press, 2020.
- [19] G. Catalan, N. Domingo. *Physical properties inside domain walls: Basic principles and scanning probe measurements*, *Domain Walls: From Fundamental Properties to Nanotechnology Concepts*, Oxford University Press, 2020, pp.
- [20] D. Lee, H. Xu, V. Dierolf, V. Gopalan, S.R. Phillpot. *Structure and energetics of ferroelectric domain walls in LiNbO₃ from atomic-level simulations*, Phys. Rev. B - Condens. Matter Mater. Phys. **82**(1) (2010).
- [21] D. Lee, R.K. Behera, P. Wu, H. Xu, S.B. Sinnott, S.R. Phillpot, L.Q. Chen, V. Gopalan. *Mixed Bloch-Néel-Ising character of 180°ferroelectric domain walls*, Phys. Rev. B - Condens. Matter Mater. Phys. **80**(6) (2009).
- [22] G.F. Nataf, M. Guennou, J.M. Gregg, D. Meier, J. Hlinka, E.K.H. Salje, J. Kreisel. *Domain-wall engineering and topological defects in ferroelectric and ferroelastic materials*, Nat. Rev. Phys. **2**11 (2020).
- [23] S.C. Hwang, C.S. Lynch, R.M. McMeeking. *Ferroelectric/ferroelastic interactions and a polarization switching model*, Acta Metall. Mater. **43**(5) (1995).
- [24] L.W. Martin, A.M. Rappe. *Thin-film ferroelectric materials and their applications*, Nat.

Rev. Mater. **22** 2(2) (2016).

- [25] J.F. Scott. *Applications of Modern Ferroelectrics*, Science **315**(5814) (2007).
- [26] C.H. Ahn, K.M. Rabe, J.M. Triscone. *Ferroelectricity at the Nanoscale: Local Polarization in Oxide Thin Films and Heterostructures*, Science **303**(5657) (2004).
- [27] S.E. Park, T.R. Shrout. *Ultrahigh strain and piezoelectric behavior in relaxor based ferroelectric single crystals*, J. Appl. Phys. **82**(4) (1998).
- [28] J.F. Scott. *Ferroelectric memories*, Springer, Berlin; New York, 2000.
- [29] R. Resta. *Towards a bulk theory of flexoelectricity*, Phys. Rev. Lett. **105**(12) (2010).
- [30] A.K. Tagantsev. *Piezoelectricity and flexoelectricity in crystalline dielectrics*, Phys. Rev. B **34**(8) (1986).
- [31] W. Ma, L.E. Cross. *Flexoelectric effect in ceramic lead zirconate titanate*, Appl. Phys. Lett. **86**(7) (2005).
- [32] W. Ma, L.E. Cross. *Flexoelectricity of barium titanate*, Appl. Phys. Lett. **88**(23) (2006).
- [33] W. Ma, L.E. Cross. *Observation of the flexoelectric effect in relaxor $Pb(Mg_{1/3}Nb_{2/3})O_3$ ceramics*, Appl. Phys. Lett. **78**(19) (2001).
- [34] W. Ma, L.E. Cross. *Strain-gradient-induced electric polarization in lead zirconate titanate ceramics*, Appl. Phys. Lett. **82**(19) (2003).
- [35] M.S. Majdoub, P. Sharma, T. Cagin. *Enhanced size-dependent piezoelectricity and elasticity in nanostructures due to the flexoelectric effect*, Phys. Rev. B - Condens. Matter Mater. Phys. **77**(12) (2008).
- [36] W. Ma. *A study of flexoelectric coupling associated internal electric field and stress in thin film ferroelectrics*, Phys. Status Solidi **245**(4) (2008).
- [37] U.K. Bhaskar, N. Banerjee, A. Abdollahi, Z. Wang, D.G. Schlom, G. Rijnders, G. Catalan. *A flexoelectric microelectromechanical system on silicon*, Nat. Nanotechnol. **11**3 11(3) (2015).
- [38] Q. Deng, M. Kammoun, A. Erturk, P. Sharma. *Nanoscale flexoelectric energy harvesting*,

Int. J. Solids Struct. **51**(18) (2014).

[39] G. Lu, Bark , Esque de los Ojos, Alcalá, Eom, Catalan. *Mechanical Writing of Ferroelectric Polarization*, Stress Int. J. Biol. Stress **59**(April) (2012).

[40] M.M. Yang, D.J. Kim, M. Alexe. *Flexo-photovoltaic effect*, Science **360**(6391) (2018).

[41] A.G. Petrov. *Flexoelectricity of model and living membranes*, Biochim. Biophys. Acta - Biomembr. **1561**(1) (2002).

[42] F. Vasquez-Sancho, A. Abdollahi, D. Damjanovic, G. Catalan. *Flexoelectricity in Bones*, Adv. Mater. **30**(9) (2018).

[43] R. Núñez-Toldrà, F. Vasquez-Sancho, N. Barroca, G. Catalan. *Investigation of The Cellular Response to Bone Fractures: Evidence for Flexoelectricity*, Sci. Reports **10** 10(1) (2020).

[44] K.D. Breneman, W.E. Brownell, R.D. Rabbitt. *Hair Cell Bundles: Flexoelectric Motors of the Inner Ear*, PLoS One **4**(4) (2009).

[45] Q. Deng, F. Ahmadpoor, W.E. Brownell, P. Sharma. *The collusion of flexoelectricity and Hopf bifurcation in the hearing mechanism*, J. Mech. Phys. Solids **130** (2019).

[46] J. Pelleg. *Mechanical properties of materials*, Solid Mech. Its Appl. **190** (2013).

CHAPTER 2

Experimental Methods

To study the mechanical and electromechanical responses of ferroelectric materials I used Atomic Force Microscopy. This chapter introduces the operational principle of Atomic Force Microscopy and provides a detailed description of every operation mode that is used for the experiments presented in this thesis. Finally, the quantification method used to quantify the experimental results is presented in **Appendix A**.

2.1 Atomic Force Microscopy

The introduction of scanning tunnelling microscope (STM) in 1981 by Gerd Binnig and Heinrich Rohrer was a breakthrough in the ability to investigate matter at the atomic scale. Its spatial resolution in combination with its intriguing simplicity allowed imaging individual atoms and it immediately became a useful tool in surface science. STM uses the tunnelling current between a biased tip and a sample and thus, it is applicable only on conducting samples. STM is at the basis of the invention of atomic force microscope (AFM) in 1986 by G. Binnig [1], where it was used to detect small deflections of a cantilever with a sharp end sensing surface forces. The basic concept of AFM is that a sharp tip at the end of a cantilever can sense forces and interactions between tip and the sample, ranging from short range Van der Waals repulsive interactions used to building up a map of sample's surface topography to long range electrostatic or magnetostatic interactions, use to map sample's functional properties, such as magnetic domains. AFM expanded the application of scanning probe microscopies to all types of surfaces including non-conductive materials and nowadays is being used in multiple fields of science such as physics, chemistry, biology, medicine and more.

2.1.1 Basic components of an AFM

In force microscopy a sharp ended tip is attached at the end of a cantilever, which acts like a spring and senses the forces between the tip and the sample. These interaction forces produce a deflection of the cantilever that is measured, most commonly using optical techniques. All force microscopes have five essential components: the cantilever with the sharp tip, the sensor for cantilever's deflection, a feedback system to monitor and control cantilever's motion, a mechanical stage to move the sample with respect to the tip and finally, a computational system that converts the electronic signals obtained from the static and dynamic deflection of the cantilever into an image. A sketch of an AFM is presented in **Figure 2.1**.

There is a variety of AFM cantilevers, developed to optimize different type of measurements. The main characteristic of a cantilever is its stiffness, i.e., the spring constant that defines the ability to bend the cantilever. The stiffness of the cantilever depends on the material from which it is fabricated, and on its geometrical characteristics (length, width etc.). Different applications will also require the cantilevers to be coated with an extra layer of material, depending on the

desirable properties of the cantilever and the tip. For example, to measure the magnetic response of a sample, a tip with a magnetic coating is needed and in order to apply electric fields or pick up electric currents, the cantilever and the tip need to be coated with a conductive film, which is typically based on Pt. The radius of the tip varies from a few nm to tens of nm and determines the spatial resolution of AFM measurement.

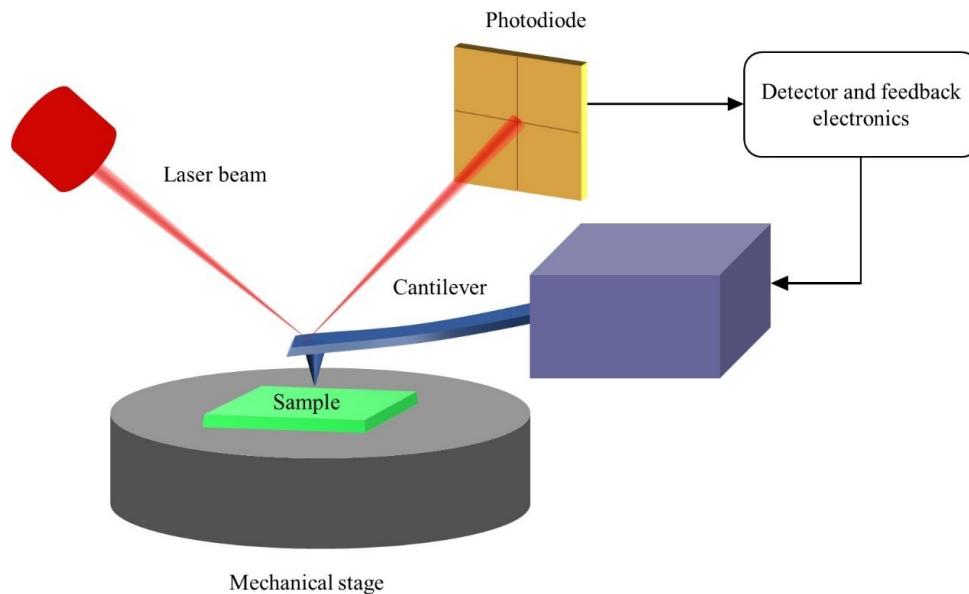


Figure 2.1: Schematic representation of the basic components of an AFM

The cantilevers can be used in static or dynamic mode. In static or constant force mode, the cantilever is brought in contact with a surface until a certain degree of bending, and thus force between the cantilever and the sample is achieved. Then, the cantilever is scanned over the surface while the feedback loop of the system keeps this force constant by adjusting the z-scanner position.

In dynamic or non-contact mode, the cantilever is oscillated following a single harmonic oscillation (SHO) movement close to the surface using different methodologies: i) mechanically, by using a piezo shaker that is placed in the base of the cantilever holder which is excited at a certain frequency and ii) thermally by photothermal actuation, where an alternate laser beam is focused at the base of the cantilever and the thermal expansion and contraction of the material causes a vibration of the cantilever [2]. The advantages of photothermal actuation, as compared to piezo vibration is a more stable and clean vibration of the cantilever, away from mechanical vibration noise of other parts of the holder, and in a wider range of frequencies. **Figure 2.2**

shows scanning electron microscopy images (SEM) of a type of cantilever used in the experiments presented in this thesis. Finally, depending on the characteristic geometry, material and stiffness, the cantilevers show different resonant frequencies associated to the different mechanical bending modes of the cantilever.

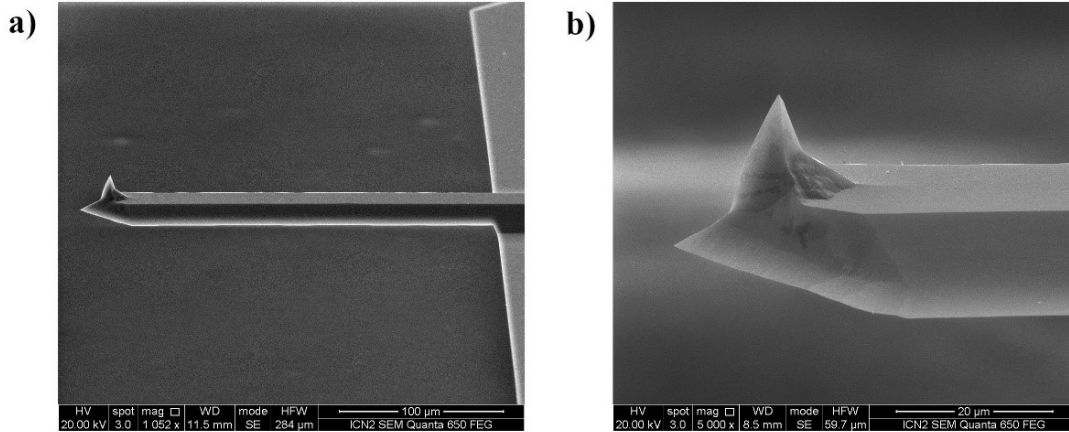


Figure 2.2: SEM images of AFM cantilever. The cantilever is a PPP-NCL type (Nanosensors; Schaffhausen, Switzerland) with cantilever stiffness $k \sim 45$ N/m and no coating. The nominal values for length, thickness and width of the cantilever are 225 μ m, 7 μ m and 38 μ m respectively.

The motion of the cantilever gives information about the forces between the tip and the sample. This motion can be detected in different ways. The first one, commonly used in ambient AFM platforms, is Optical Beam Deflection (OBD) [3]. In this case, a laser beam is reflected on the back side of the cantilever at its free end to a photodiode. Changes in the cantilever deflection angle $\Delta\theta$ turn into changes of the laser position on the photodiode. For small angles of deflection, the $\Delta\theta$ is linearly proportional to the z displacement of the cantilever, and thus the photodiode signal records the motion of the cantilever in the z direction. While this turns to be a good approach for non-contact AFM or dynamic mode, its use to detect vibrations of the cantilever in contact mode becomes more controversial since the change of angle of the cantilever strongly depends on the measuring point along its axis [4]. Additionally, the laser beam must be calibrated both with respect to the cantilever and the photodiode, inserting errors in the detection of cantilever's motion. To overcome some of this hindrances, a second detection method based on interferometry [5] is starting to be used to directly track z -displacements of the cantilever. In the case of the interferometer, a laser is being partially deflected on the back side of the cantilever and conducted back to the interferometer. The phase difference between the deflected beam and the reference beam give information about the deflection of the cantilever

directly [6,7]. Theoretical studies have shown that both detection methods can reach same levels of sensitivity [8], but interferometers are more accurate precisely because they detect the direct deflection of the cantilever, and become more convenient for contact mode measurements. AFM systems used for experiments of this thesis are based on OBD detection.

2.1.2 Operation modes of an AFM

There are two main modes to operate an AFM: contact or force constant mode, and dynamic mode, also called tapping or non-contact mode depending on the level of tip sample interaction. Dynamic mode can be operated in amplitude modulation or AM-AFM, [9] generally used in ambient conditions, or frequency modulation or FM-AFM, [10] most convenient for high vacuum condition where the resonance of the cantilevers are sharper and show higher quality (Q) values. Indeed, FM-AFM was the first AFM mode that allowed atomic resolution in ultra-high vacuum [11]. In all cases, the cantilever is scanning over the sample's surface and its motion is detected, monitored and analysed, creating an image of the surface.

In contact mode, the tip is in contact with the sample and is “dragging” over the surface while scanning. This mode, which is also called constant force mode, senses short-range interatomic repulsive forces between the tip and the sample (van der Waals) and is the first mode developed for AFM and conceptually the most basic. The tip is brought into contact with the sample and bends due to an applied force. The feedback loop maintains the deflection of the cantilever constant, creating the image of the surface's topography. The first AFM images of atomic resolution were obtained in contact mode. The contact area between the tip and the sample, and consequently the resolution of the image, is defined by the applied force which must be lower than the inter-atomic forces. Contact mode can provide high resolution topography images but at the same time is not appropriate for all type of samples since soft samples can be damaged by the force applied by the tip on the sample.

In dynamic mode the tip is not in contact with the sample but is oscillating at a certain height above the sample, using a frequency close to a resonant vibration mode. When vibrating close to the surface, the tip can still sense the van der Waals short range interactions. When vibrating far away from the surface, the tip is sensitive to long-range forces such as electrostatic, magnetostatics. In both cases, when the tip is oscillating at or near resonance frequency and approaches the surface of the sample, this oscillation changes due to the interaction forces

damping the SHO behavior and turning into a frequency shift of the characteristic vibration or an amplitude decrease of the oscillation. Then, the feedback loop acting on the z-scanner is used to maintain a certain distance of tip from the surface by trying to maintain the resonance frequency constant in the FM-AFM mode or a constant oscillation amplitude (setpoint) $A_{sp} < A_0$ smaller than the free oscillation amplitude in AM-AFM.

2.2 Piezoresponse Force Microscopy

Piezoresponse force microscopy (PFM) is a contact AFM mode which is used to image ferroelectric materials by exploiting the inverse piezoelectric effect. It was first applied in 1996 by Gruverman, Auciello and Tokumoto to study the ferroelectric domain structure in thin films, and immediately followed by different groups [12–16]. Advances in PFM over the last decade have made this technique one of the most essential and mainstream in the field of nanoferroics [17] and have paved the way for exploring new emergent phenomena.

2.2.1 Operating principle

In PFM a conductive tip is brought into contact with the sample and excites it with an *ac* voltage. Due to the converse piezoelectric phenomenon, the sample is deformed and this deformation is recorded by the deflection of the cantilever. PFM can detect deformations smaller than picometers, while its lateral resolution is of few nanometers. The feedback loop keeps constant the deflection of the cantilever. In mapping of ferroelectric materials, the applied *ac* voltage is smaller than the coercive field of the sample, so that no change in ferroelectric polarization is caused. **Figure 2.3** shows the deflection of the cantilever in a PFM measurement due to deformation of the sample.

PFM has three main observable magnitudes: amplitude, phase and frequency. Amplitude is proportional to the magnitude of polarization, while phase denotes the orientation of polarization: a phase shift of 0° between the electric *ac* excitation signal and the sample deformation is characteristic of down polarization (which tends to expand the sample under a positive voltage) and a phase shift of 180° denotes the presence of up oriented polarization (which promotes a sample contraction under positive voltages). If the driving frequency is brought close to the contact resonance frequency of the cantilever in contact with the sample, then the amplitude of

oscillation is naturally amplified by the Q factor of the resonance of the cantilever. In this case, the contact resonance frequency strongly depends mainly on the electromechanical properties of the material. The interaction between material ferroelectric and nanomechanical properties and the cantilever, will be deeply discussed through this thesis.

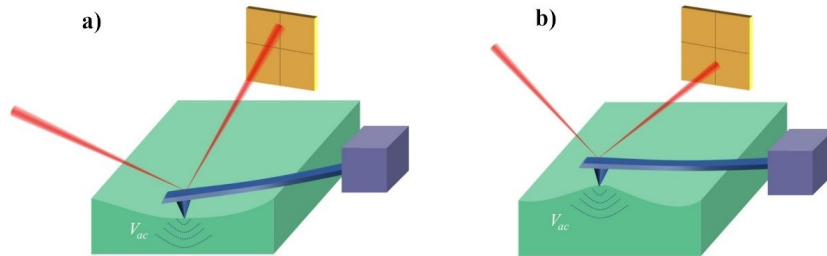


Figure 2.3: Depiction of PFM. Deformation of the sample due to applied voltage results in deflection of the cantilever in opposite directions for contraction (a) and expansion (b) of the sample.

2.2.2 Lateral and Vertical PFM

The direction of the ferroelectric polarization defines the volume change of the sample under a certain applied voltage. In a ferroelectric material with polarization pointing perpendicular to the surface's plane, changes in the volume will be also out-of-plane. This will cause deflection of the cantilever. But in case of in-plane polarized domains, inverse piezoelectric effect will deform the material in the direction parallel to the surface's plane. This type of deformation will cause a torsion of the cantilever when the in-plane direction of the polarization is perpendicular to the cantilever axis, and a buckling movement when the in-plane deformations is parallel to the cantilever axis. Indeed, the bucking excitation will turn into a cross-talk on the out of plane direction of the cantilever motion. In PFM measurements, the detection system can be sensitive to both types of movements of the cantilever, depending on the photodiode detection signal. Consequently, PFM can be in vertical or lateral mode, depending on the type of cantilever motion that is being detected and altogether, a vectorial image of the polarization orientation can be obtained.

2.2.3 DART PFM

Even in materials with high piezoelectric coefficient, the deformation of the material due to applied voltage is usually lower than the sensitivity of an AFM system. For that reason, amplification of the signal is required. One way is by using a lock-in amplifier. The detected deflection of the

cantilever is the internal signal of a lock-in amplifier, which compares it with a reference signal, amplifies it and sends it back to AFM operating system. Another way to amplify the response of the material is by using the natural amplification of the contact resonance frequency. In that case, the frequency of the *ac* voltage sent to the sample is set close to the contact resonance frequency of the cantilever-sample system and the response of the material is naturally amplified. The contact resonance frequency though depends not only on the cantilever but also on the material, the mechanical contact between the tip and the sample and the forces between them. Thus, contact resonance frequency can significantly change during a scan.

A way to track contact resonance frequency is dual-amplitude resonance-tracking (DART) PFM [18]. In this mode the cantilever is driven at two frequencies simultaneously, one slightly above and one slightly below the contact resonance frequency (see **Figure 2.4**). Then, a feedback loop acting on the contact resonance frequency acts to keep the amplitude of oscillation of both vibrations equal over the scan, thus tracking the changes induced by the alteration of the tip-sample mechanical coupling during the scan.

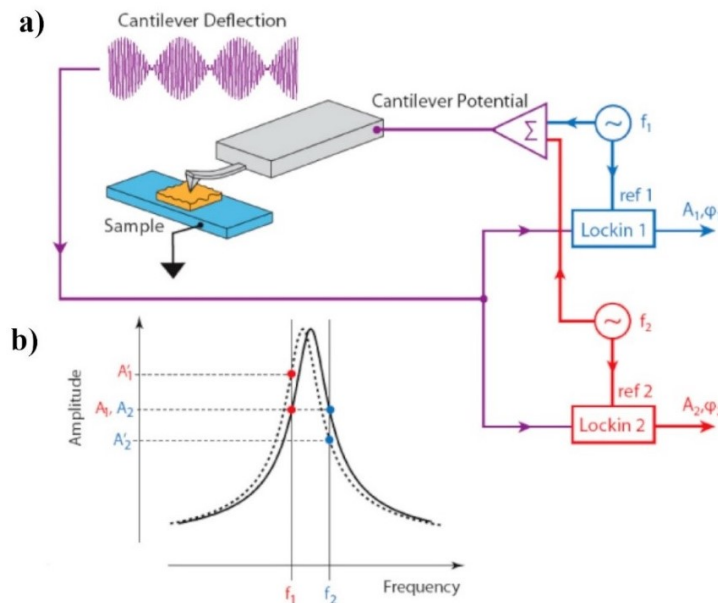


Figure 2.4: a) Schematic diagram of experimental set up for DART PFM. b) Principle of DART PFM. Figure is taken from [18].

2.2.4 Band Excitation PFM

Besides single frequency or frequency-track methods, there is an alternative method that does not require tracking of resonance frequency called Band Excitation PFM. In this method the

system is excited simultaneously not in a defined frequency but in a range of frequencies covering the contact resonance frequency by sending an ac pulse and analysing its fourier transformed signal. Its response is recorded in the same or wide range of frequencies [19]. The data acquired from Band Excitation method is usually analysed by fitting a single harmonic oscillator (SHO) function to the resonance to extract the corresponding parameters of the cantilever's behaviour. The operating principle of this method is presented in Figure **Figure 2.5**.

Band excitation method is a universal data-acquisition method applied to different AFM modes with numerous advantages. The fact that the cantilever's response is recorded in a range of frequencies and analysed afterwards allows to identify non-linear responses. Additionally, it allows the decoupling of dissipating and conservative interactions and removes the topographic crosstalk. Finally, Band Excitation PFM, in contrast with DART PFM, provides accurate information about quality factor (Q factor) of the oscillation of the tip (Q factor measures the width of SHO peak and is a factor of energy dissipation of the oscillation).

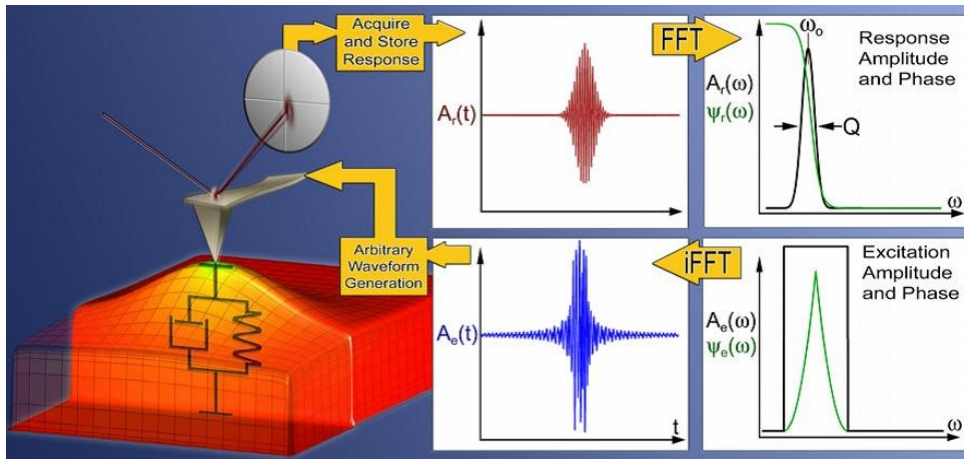


Figure 2.5: Operating principle of Band Excitation method. Figure is taken from [19].

2.2.5 Spectroscopy Switching PFM

PFM allows to study the dynamics of ferroelectric polarization by spectroscopy switching PFM. Here, hysteresis loops are performed by applying a voltage following a square-triangular function: the voltage is applied on the sample through the AFM tip with values ranging from 9 Volts to -9 Volts, and the sample can be repeated several times (**Figure 2.6a**). The applied voltage function is a square-triangular collection of pulses that for most experiments in this thesis have a length of 37.8 ms and a cycling period of 5 s. The hysteretic behaviour of the film is built up using the

points measured at zero field, that is, at the remanence after the application of a voltage pulse, and in each case, we extract the PFM phase (**Figure 2.6b**) and amplitude (**Figure 2.6c**). Since the piezoresponse measurement is done using DART PFM, the PFM signals of the hysteresis loops are measured on resonance.

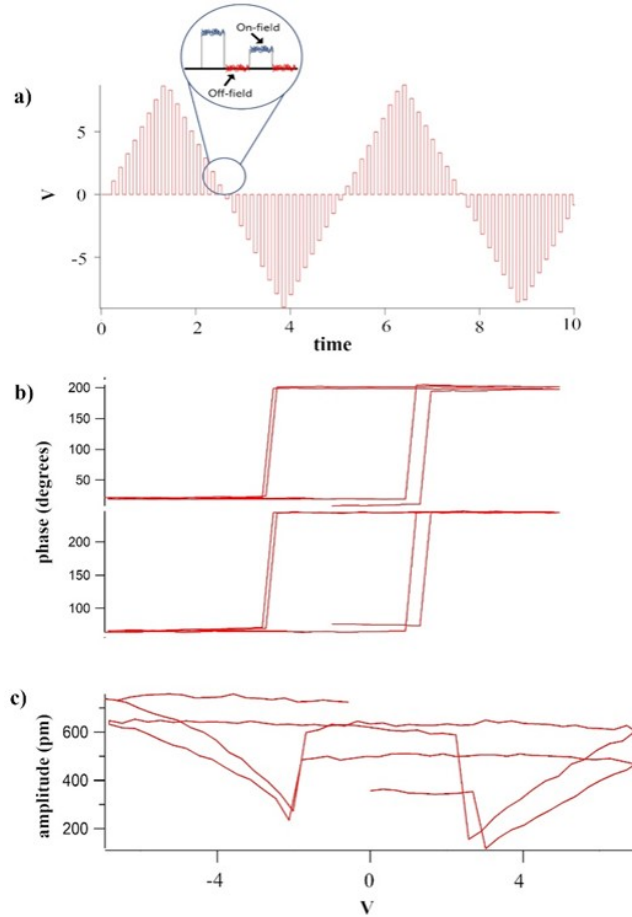


Figure 2.6: PFM hysteresis loop of PbTiO_3 (001) thin films obtained from spectroscopy switching DART PFM. a) Applied voltage during the hysteresis loop, as a function of time. b) PFM phase as a function of applied voltage, showing that the as grown state of the film is polarized down. c) PFM amplitude with the typical butterfly shape indicating the ferroelectric switching. The tip is a conductive with PtIr coating with cantilever stiffness ~ 45 N/m (PPP-NCHPt Nanosensors; Schaffhausen, Switzerland), while the applied force is ~ 630 nN.

2.3 Contact Kelvin Force Probe Microscopy

Kelvin probe force microscopy (KPFM) is a non-contact AFM technique that was developed to measure the contact potential difference (CPD) between the sample surface and a conductive tip [20,21]. In cases where the fermi energy levels between tip and sample are different, then when the tip approaches the sample's surface an electrical force is generated between them. This force

affects the oscillation of the tip and feedback loop is used to cancel it by applying an external voltage to compensate for the contact potential difference between the tip and surface. Knowing the work function of the tip, the work function of the sample can be calculated. However, KPFM is a non-contact technique and surface and tip are always separated by air or vacuum. When moving the cantilever towards the contact limit, KPFM-like measurements in contact mode (a mode so called contact Kelvin force probe microscopy (cKPFM) [22]) lead to the determination of what is called junction contact potential difference (jCPD) across the junction of tip-sample. Although in some cases CPD and jCPD are equal, this is not always true.

Calculation of jCPD is achieved with CKPFM, where the tip oscillates near contact resonance frequency or in a range of frequencies (Band Excitation method) while an *ac* and *dc* voltage are applied to the sample's surface. Specifically, an *ac* voltage is applied to excite the sample while the deflection of the cantilever is being measured. At the same time a *dc* voltage is being ramped (V_{read}). Nullification of this voltage allows the detection of jCPD. There are two types of *dc* voltage used, as shown in **Figure 2.7**. In the first scenario (**Figure 2.7a**) a *dc* voltage consists of a small amplitude sweep. This voltage sweep is suitable to measure the junction potential but excludes the track of fast potential changes since voltage sweep is time consuming. The second scenario is to apply subsequent series of *dc* voltage (**Figure 2.7b**). This way enables fast reading of jCPD but is not appropriate for samples dependent on measurement history. Finally, to investigate the charge injection on the sample's surface, an extra *dc* voltage pulse (V_{write}) is applied before reading the sample's response, allowing to capture relaxation dynamics.

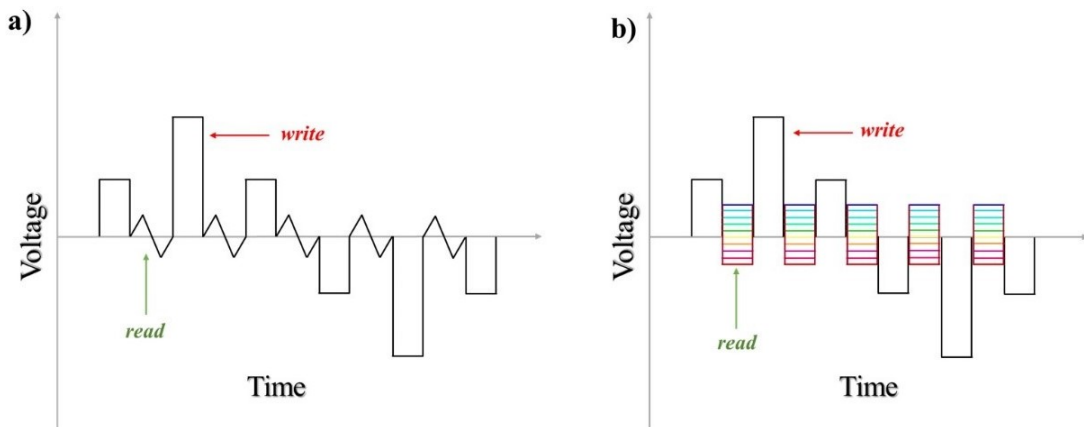


Figure 2.7: Scheme of voltage applied by the tip on cKPFM measurements. Pulsed *dc* voltage is applied to inject charges (V_{write}) and *ac* voltage with combination of *dc* voltage (V_{read}) is used to measure the response of the sample. V_{read} can be voltage sweep (a) or subsequential values of *dc* voltage (b).

CKPFM provides images containing a big amount of information and is an AFM mode that can be extremely time consuming. A way to speed up this type of measurement and still be able to extract information about jCPD is to apply only Vac while reading the response of the sample, with no additional Vread. In this case, jCPD can be calculated by the slope of cKPFM curves.

Finally, it is worth mentioning that while jCPD can be calculated through cKPFM, its nature may remain unknown since charges can have physical, chemical or electrochemical origin. Nevertheless, cKPFM can be an insightful method to investigate charge injection, especially in cases of ferroelectric materials with different polarity over the sample's surface.

2.4 Contact Resonance Atomic Force Microscopy

Contact resonance atomic force microscopy (CR-AFM) is an advanced AFM mode based on acoustic force atomic force microscopy (AFAM). AFAM was first developed by Ute Rabe in 1994 [23] and combines the high resolution of scanning probe microscopy with the ability of acoustics to image elastic properties. In AFAM the tip is in contact with the sample while an ultrasonic transducer placed under the sample is vibrating. High frequency vibrations of the ultrasonic stage are transmitted into cantilever due to the tip-sample interaction forces. Adhesive and repulsive forces between tip and sample give information about the energy dissipation of the system (tip-sample) and thus, information about elastic properties of the sample. In a similar way, in ultrasonic atomic force microscopy (UAFM)[24] the cantilever is vibrated at ultrasonic frequencies, revealing subsurface features of the sample [24].

In CR-AFM the cantilever in contact with the sample is excited mechanically at a contact resonance frequency [25] of the cantilever-sample system. A schematic representation of CR-AFM is shown in **Figure 2.8**, where the system of tip-sample in contact is oscillated under mechanical excitation. Its resonant vibrations depend on both geometrical characteristics and material properties of the cantilever and also tip-contact mechanical characteristics. During scanning, the force applied by the tip is being kept constant while contact resonance frequency of the system is being tracked. Considering that the geometrical characteristics of the tip do not vary during scanning, then the mechanical coupling between the tip and sample strongly dominates the contact resonance frequency: since changes in the contact resonance frequency of the system are related with changes in the mechanical contact between the tip and sample and since mechanical

contact is affected by stiffness of the material, shifts in contact resonance frequency of CR-AFM measurements are proportional to changes in the stiffness of the material.

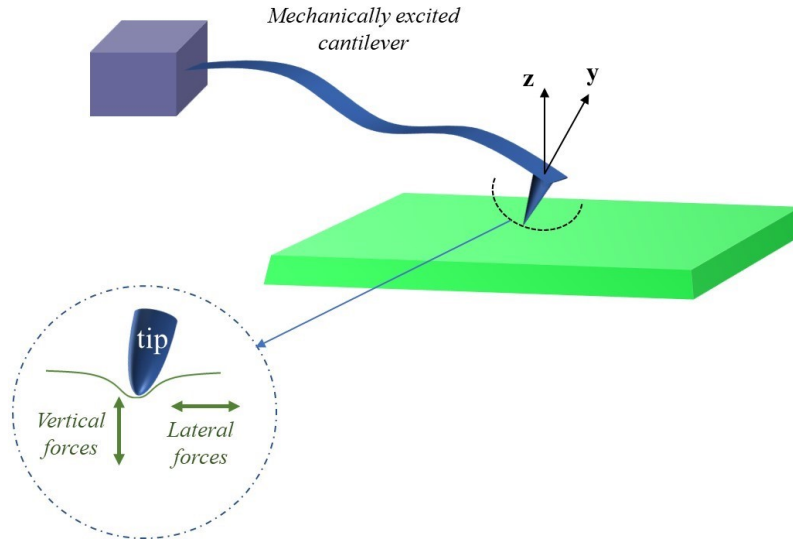


Figure 2.8: Scheme of CR-AFM mode. The tip is in contact with the surface and the cantilever is mechanically excited at its clamped end, promoting flexural vibrations.

Here, the mechanical excitation of the cantilever can be achieved in two ways. The first way is by applying *ac* voltage at the piezo element that is placed at the base of the cantilever, promoting mechanical vibration of the cantilever, or using an acoustic stage in which a piezo element excites the sample. The second way is by photothermal actuation [26,27], in which the cantilever is irradiated by a laser close to its clamped end, thereby the induced thermal expansion promoting the cantilever's vibration. This technique provides a wide frequency range of excitation as well as a cleaner cantilever resonance spectrum.

CR-AFM is based on tracking and recording contact resonance frequency of the system. In a similar way as for PFM, contact resonance frequency can be tracked either using DART or Band Excitation method.

Apart from high resolution topographic images of elastic properties of materials, CR-AFM measurements can provide quantitative results. The theoretical approach and appropriate models concerning quantification of CR-AFM results are presented in **Appendix A**. The ability to map and quantify the elastic properties of materials has established CR-AFM as an effective tool in the field of nanotechnology [28,29], with a broaden application in polymers [30,31], ferroelectric ceramics [32,33], and thin films [34].

References

- [1] G. Binnig, C.F. Quate, C. Gerber. *Atomic force microscope*, Phys. Rev. Lett. **56**(9) (1986).
- [2] N. Umeda, S. Ishizaki, H. Uwai. *Scanning attractive force microscope using photothermal vibration*, J. Vac. Sci. Technol. B Microelectron. Nanom. Struct. Process. Meas. Phenom. **9**(2) (1998).
- [3] G. Meyer, N.M. Amer. *Novel optical approach to atomic force microscopy*, Appl. Phys. Lett. **53**(12) (1998).
- [4] A. Labuda, R. Proksch. *Quantitative measurements of electromechanical response with a combined optical beam and interferometric atomic force microscope*, Appl. Phys. Lett. **106**(25) (2015).
- [5] R. Erlandsson, G.M. McClelland, C.M. Mate, S. Chiang. *Atomic force microscopy using optical interferometry*, J. Vac. Sci. Technol. A Vacuum, Surfaces, Film. **6**(2) (1998).
- [6] N. V. Andreeva. *Atomic force microscopy with interferometric method for detection of the cantilever displacement and its application for low-temperature studies*, Ferroelectrics **525**(1) (2018).
- [7] A. von Schmidsfeld, T. Nörenberg, M. Temmen, M. Reichling. *Understanding interferometry for micro-cantilever displacement detection*, Beilstein J. Nanotechnol. **7**(1) (2016).
- [8] C.A.J. Putman, B.G. de Groot, N.F. van Hulst, J. Greve. *A theoretical comparison between interferometric and optical beam deflection technique for the measurement of cantilever displacement in AFM*, Ultramicroscopy **42**(44) (1992).
- [9] Y. Martin, C.C. Williams, H.K. Wickramasinghe. *Atomic force microscope-force mapping and profiling on a sub 100-Å scale*, J. Appl. Phys. **61**(10) (1998).
- [10] T.R. Albrecht, P. Grütter, D. Horne, D. Rugar. *Frequency modulation detection using high-Q cantilevers for enhanced force microscope sensitivity*, J. Appl. Phys. **69**(2) (1998).
- [11] F.J. Giessibl. *Advances in atomic force microscopy*, Rev. Mod. Phys. **75**(3) (2003).
- [12] L.M. Eng, M. Abplanalp, P. Gunter. *Ferroelectric domain switching in tri-glycine sulphate*

and barium-titanate bulk single crystals by scanning force microscopy, *Appl. Phys. A Mater. Sci. Process.* **66**(S1) (1998).

[13] J.A. Christman, R.R. Woolcott, A.I. Kingon, R.J. Nemanich. *Piezoelectric measurements with atomic force microscopy*, *Appl. Phys. Lett.* **73**(26) (1998).

[14] G. Zavala, J.H. Fendler, S. Trolier-McKinstry. *Characterization of ferroelectric lead zirconate titanate films by scanning force microscopy*, *J. Appl. Phys.* 81(11) (1998).

[15] A. Gruverman, O. Auciello, H. Tokumoto. *Scanning force microscopy for the study of domain structure in ferroelectric thin films*, *J. Vac. Sci. Technol. B Microelectron. Nanom. Struct. Process. Meas. Phenom.* 14(2) (1996).

[16] A. Gruverman, O. Auciello, H. Tokumoto. *Imaging and control of domain structures in ferroelectric thin films via Scanning Force Microscopy*, *Annu. Rev. Mater. Sci.* **28**(1) (1998).

[17] A. Gruverman, M. Alexe, D. Meier. *Piezoresponse force microscopy and nanoferroic phenomena*, *Nat. Commun.* **10**(1) (2019).

[18] B.J. Rodriguez, C. Callahan, S. V. Kalinin, R. Proksch. *Dual-frequency resonance-tracking atomic force microscopy*, *Nanotechnology* **18**(47) (2007).

[19] S. Jesse, S. V. Kalinin, R. Proksch, A.P. Baddorf, B.J. Rodriguez. *The band excitation method in scanning probe microscopy for rapid mapping of energy dissipation on the nanoscale*, *Nanotechnology* 18(43) (2007).

[20] W. Melitz, J. Shen, A.C. Kummel, S. Lee. *Kelvin probe force microscopy and its application*, *Surf. Sci. Rep.* **66**(1) (2011).

[21] M. Nonnenmacher, M.P. O'Boyle, H.K. Wickramasinghe. *Kelvin probe force microscopy*, *Appl. Phys. Lett.* **58**(25) (1998).

[22] N. Balke, P. Maksymovych, S. Jesse, I.I. Kravchenko, Q. Li, S. V Kalinin. *Exploring Local Electrostatic Effects with Scanning Probe Microscopy: Implications for Piezoresponse Force Microscopy and Triboelectricity* *ACS Nano* **8**(10) (2014).

[23] U. Rabe, W. Arnold. *Acoustic microscopy by atomic force microscopy*, *Appl. Phys. Lett.*

64(12) (1994).

[24] K. Yamanaka, H. Ogiso, O. Kolosov. *Ultrasonic force microscopy for nanometer resolution subsurface imaging*, Appl. Phys. Lett. **64**(2) (1994).

[25] J.P. Killgore, F.W. Delrio. *Contact Resonance Force Microscopy for Viscoelastic Property Measurements: From Fundamentals to State-of-the-Art Applications*, Macromolecules **51**(18) (2018).

[26] N. Umeda, S. Ishizaki, H. Uwai. *Scanning attractive force microscope using photothermal vibration*, J. Vac. Sci. Technol. B Microelectron. Nanom. Struct. Process. Meas. Phenom. **9**(2) (1998).

[27] G.C. Ratcliff, D.A. Erie, R. Superfine, *Photothermal modulation for oscillating mode atomic force microscopy in solution*, Appl. Phys. Lett. **72**(15) (1998).

[28] U. Rabe, M. Kopycinska, S. Hirsekorn, W. Arnold. *Evaluation of the contact resonance frequencies in atomic force microscopy as a method for surface characterisation*, Ultrasonics **40**(1–8) (2002).

[29] U. Rabe, K. Janser, W. Arnold. *Vibrations of free and surface-coupled atomic force microscope cantilevers: Theory and experiment*, Rev. Sci. Instrum. **67**(9) (1996).

[30] P.A. Yuya, D.C. Hurley, J.A. Turner. *Contact-resonance atomic force microscopy for viscoelasticity*, J. Appl. Phys. **104**(7) (2008).

[31] S. Friedrich, B. Cappella. *Application of contact-resonance AFM methods to polymer samples*, Beilstein J. Nanotechnol. **11**(1) (2020).

[32] J.P. Killgore, D.G. Yablon, A.H. Tsou, A. Gannepalli, P.A. Yuya, J.A. Turner, R. Proksch, D.C. Hurley. *Viscoelastic Property Mapping with Contact Resonance Force Microscopy*, Langmuir **27**(23) (2011).

[33] U. Rabe, S. Amelio, E. Kester, V. Scherer, S. Hirsekorn, W. Arnold. *Quantitative determination of contact stiffness using atomic force acoustic microscopy*, Ultrasonics **38**(8) (2000).

[34] M. Kopycinska-Müller, R.H. Geiss, J. Müller, D.C. Hurley. *Elastic-property measurements of ultrathin films using atomic force acoustic microscopy*, Nanotechnology **16**(6) (2005).

CHAPTER 3

Mechanical Properties of Ferroelectric Domains

All ferroelectric materials are also piezoelectric, and therefore the ferroelectric polarization is intrinsically coupled to the deformation of the material. Likewise, the mechanical properties of ferroelectric materials are strongly entangled with their polarization, as the depolarization field generated by the piezoelectric polarization adds to the energy cost of deformation. This depolarization field is proportional to the square of polarization and therefore independent of the polar sign. This mechanical invariance under inversion symmetry, however, can break down in the presence of strain gradients.

Strain gradients induce polarization in any dielectric material (either centrosymmetric or not), due to flexoelectricity. The mechanical properties under non-uniform deformations, such as those appearing under an applied mechanical load with an AFM tip, depend on the coupling of the piezoelectric coefficient with the flexoelectric polarization; they may be parallel, and therefore summing contributions, or antiparallel and therefore decreasing the overall electromechanical response. When considering ferroelectric materials with out-of-plane polarization, this interplay leads to a mechanical asymmetry to the system that enables the distinction of oppositely polarized domains based on their nanomechanical response.

In this chapter I present how this emergent asymmetry can be exploited to mechanically read the sign of ferroelectric polarization in a non-destructive way by characterizing the mechanical properties of ferroelectric materials. Using Contact Resonance Atomic Force Microscopy, I show how mechanical reading of ferroelectric polarity (i.e., sign of ferroelectric polarization) is feasible in a variety of ferroelectric materials with domains of opposite out-of-plane polarization, from single crystals to thin films. According to the physical basis of this effect, the distinction of

ferroelectric polarity based on the nanomechanical response of the domains must indeed be a universal phenomenon, a hypothesis supported here by measurements on ferroelectrics and multiferroics of different families.

Additionally, I demonstrate that this phenomenon is size dependent: the nanomechanical response of ferroelectric materials under inhomogeneous deformation is enhanced when the size of the material is reduced to the nanoscale, for example in thin films. Finally, at Appendix B I discuss how the sensitivity in mechanical reading is affected by the mechanical properties of the sensing probe.

3.1 Asymmetry in the mechanical properties of ferroelectric materials under inhomogeneous deformation

As a subtype of piezoelectrics, any ferroelectric material generates a polarization P in response to a deformation, and this has an associated energy cost as discussed in **Section 1.4.1**. This energy cost U is given by:

$$U = \frac{1}{2}k\varepsilon^2 + \frac{1}{2}\frac{P_h^2}{\chi} \quad (3.1)$$

where k is the elastic constant, ε is the strain field, P_h is the polarization induced by the homogeneous deformation and χ the electric susceptibility. The total energy cost of the deformation has two components: an elastic one and an electrostatic one. The elastic cost is given by the first term of the equation and is associated with the deformation itself and is described by Hooke's law; the electrostatic cost is given by the second term and is associated with the polarization change induced by the deformation.

In ferroelectrics, the total cost of energy of a homogeneous deformation is symmetric with respect to space inversion. The elastic term is symmetric because the deformation due to polarization is identical for both directions of the polarization. The electrostatic term is also symmetric as it is proportional to the square of the polarization, and thus independent of the sign of polarization. That means that the cost of energy associated with a *homogeneous* deformation (a strain) does not depend on the direction of the polarization.

Under *inhomogeneous* deformation though, the scenario becomes more complex. Now the resultant polarization induced by the inhomogeneous deformation has two sources: the strain itself, via piezoelectricity, and the strain gradient arising from the inhomogeneity, via flexoelectricity. The equation of energy cost now becomes:

$$U = \frac{1}{2}k\varepsilon^2 + \frac{1}{2}\frac{P_{inh}^2}{\chi} \quad (3.2)$$

where

$$P_{inh} = \left| \vec{P}_{piezo} + \vec{P}_{flexo} \right| \quad (3.3)$$

The coupling of piezoelectricity and flexoelectricity now affects the electrostatic term of **Equation 3.2**, as the induced polarization due to inhomogeneous deformation has two com-

ponents (**Equation 3.3**), the induced polarization due to piezoelectricity and the one due to flexoelectricity. The two components of the electrostatic term can be parallel or antiparallel, depending on the sign of the piezoelectric coefficient of the material. Consequently, the same inhomogeneous deformation can induce an enhanced polarization, when piezoelectricity and flexoelectricity are parallel ($P_{inh} \uparrow \uparrow = +P_{piezo} + P_{flexo}$), and a reduced polarization when piezoelectricity and flexoelectricity are antiparallel ($P_{inh} \downarrow \uparrow = -P_{piezo} + P_{flexo}$). The electrostatic cost of deformation still depends on the square of the polarization (P_{inh}^2), but now, the magnitude of the polarization itself changes, depending on the sign of the piezoelectric polarization. This difference in the magnitude of the polarization implies an asymmetry under space inversion, meaning that the mechanical response of ferroelectric materials to inhomogeneous strains depends on the sign of their ferroelectric polarization [1]. This induced asymmetry in the cost of energy under inhomogeneous deformation is the key element that enables to read the ferroelectric polarization by probing the mechanical response of ferroelectric domains.

Several works have already addressed some aspects of the effect of flexoelectricity on the mechanical response. Nanoindentation experiments on ferroelectrics have shown a strong size-dependent stiffening [2,3]. Later, Abdollahi et al., predicted theoretically that such stiffening should be asymmetric with respect to the polarity of the ferroelectric [4], and Cordero-Edwards et al., performed the first experiments that confirmed the existence of a mechanical asymmetry in uniaxial ferroelectrics [1]; the asymmetry in the free energy for oppositely-polarized ferroelectric domains of LiNbO_3 was explored by performing nanoindentation measurements, in which the impact of the flexoelectric field created by the sharp indenter while measuring the mechanical response (both plastic and elastic) of the material was evaluated. The total mechanical energy generated by the deformation of the material consists of the plastic and the elastic energy. Plastic energy concerns the material properties related to energy dissipation while elastic energy is related with the elasticity of the material; in other words, plastic deformation is energy-dissipating and therefore irreversible, while elastic deformation is energy-conservative and therefore reversible. The total energy generated by the deformation was found to be symmetric with respect to the direction of polarization, as expected, since the energy provided by the indenter is independent of the sample polarity. Yet, both plastic and elastic energy were found to be individually asymmetric meaning that all mechanical responses are in principle polarity dependent.

Although these results demonstrate unambiguously that stiffness of uniaxial ferroelectrics

depend on the sign of ferroelectric polarization, they were obtained by nanoindentation, an invasive and destructive technique that literally involves making indents in the sample. In the present thesis, the mechanical response of ferroelectric domains is being studied and exploited in a non-destructive way by contact-resonance atomic force microscopy (CR-AFM).

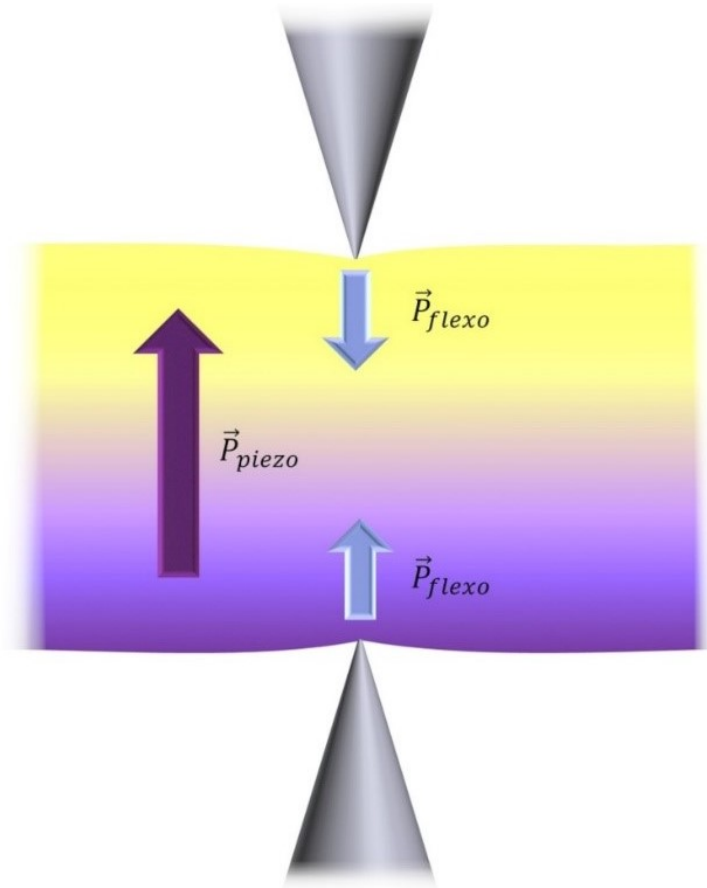


Figure 3.1: Schematic representation of a ferroelectric single crystal. Flexoelectric field induced by AFM tip is oriented towards the tip. The induced asymmetry in mechanical properties of ferroelectric domains depends on the direction of induced flexoelectricity with respect to the ferroelectric polarization's direction.

3.2 AFM tip induced strain gradients

AFM tips can induce very high mechanical loads locally. Stress induced by an AFM tip can cause deformation of the material [5] and lead to changes on its functional properties [6]. Even though the range of applied forces in which AFM operate is between some few pN to some tens of μN , it is applied over a nanometric contact area and thus the resulting loads, meaning the force over the tip-sample contact area, can be huge. Additionally, the geometric characteristics of the tip with

such a reduced nanoscale contact point creates localized enormous strain gradients [5]. Indeed, such strain gradients induced by an AFM tip are sufficiently large to mechanically switch the ferroelectric polarization of a thin film [7], and have been applied, for example, for the mechanical gating of FET transistors [8]. The aim here is to exploit the strain gradients generated by an AFM tip to create flexoelectric fields on ferroelectric materials while simultaneously measuring the associated induced asymmetry in their nanomechanical response.

The geometrical characteristics of a tip apex lead to strain gradients with radial orientation towards the surface of the sample, as shown in **Figure 3.2.a**. Some previous works [5,9] already investigated the tip-induced strain gradients, as well as the associated flexoelectric fields for thin films of BaTiO₃. There, the distribution of the flexoelectric field was calculated using finite-element methods, and it was demonstrated that for a tip radius of 30 nm and an applied mechanical load of 500 nN, the maximum magnitude of flexoelectric field is 3.8 MV/cm for an insulating tip and 4.8 MV/cm for a conductive tip (**Figure 3.2.b** and **3.2.c**). The different magnitudes as a function of the conductivity of the tip reflect the importance of the depolarizing fields generated by the flexoelectric polarization: these are partially screened when a metallic tip is used, resulting in a larger flexoelectric polarization and internal flexoelectric field, whereas they are unscreened with fully insulating tips, resulting in smaller flexoelectricity.

If we concentrate on the out-of-plane direction of the sample and consider a sample with a positive flexoelectric coefficient, the application of a strain gradient under an AFM tip induces a net polarization down, equivalent to the generation of a positive electric field emanating from the tip apex (see **Figure 3.1** and **3.2.a**). Lu et al., [7] demonstrated that the tip-induced flexoelectric field can overcome the coercive field and cause switching of ferroelectric polarization from pointing up to pointing down directions, completely analogous to the application of a positive external voltage. Particularly, in the case of BaTiO₃ thin films with thickness of 12-unit cells and coercive voltage of 2 V, a tip with a contact radius of 10 nm and an applied force above 1 μ N can achieve full mechanical switching of the ferroelectric polarization. The induced flexoelectric field created under these conditions was calculated to be 2 MV/cm.

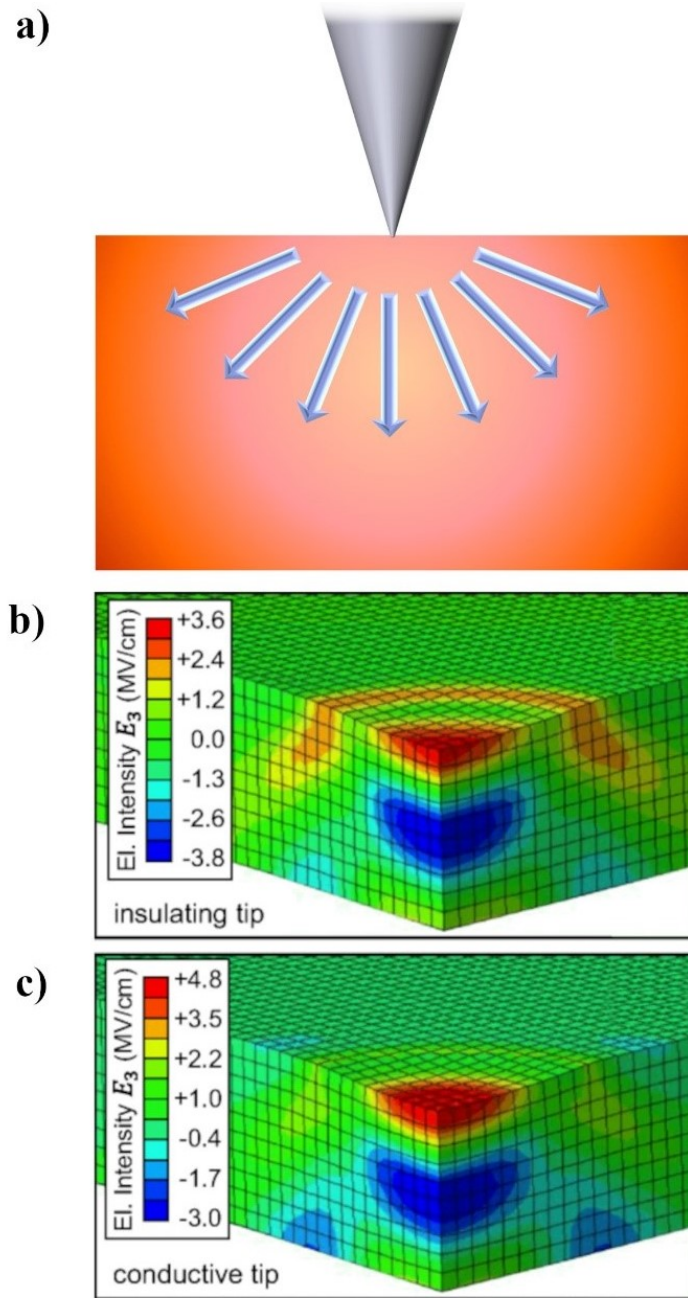


Figure 3.2: a) Schematic representation of the flexoelectric field induced by an AFM tip in contact with the sample. Flexoelectric field distribution under the tip in case of insulating (b) and conductive (c) tip, as calculated by finite element simulations, reproduced from [5]. The sample is BaTiO₃ ultra-thin film (5nm thickness) grown on a SrTiO₃ substrate with a La_{0.67}Sr_{0.33}MnO₃ buffer electrode. The isocontours show the total field in the vertical direction for an applied mechanical load of 500 nN. Areas where strain gradients are opposing to domain switching are noted with red color, while blue color represents the maximum value of the flexoelectric field.

3.3 Mechanical reading of ferroelectric polarization

As previously described, the flexoelectrically-modulated total induced polarization under inhomogeneous deformation has consequences on the mechanical response of the material as a function of the domain's polarization. More specifically, when ferroelectric polarization is pointing down, the flexoelectric and piezoelectric polarization have the same orientation (parallel) resulting into an increase of the total ferroelectric polarization. The increase of the total energy cost of deformation ensuing from this parallel orientation, compels down-polarized domains to show a stiffer response. Conversely, in ferroelectric domains with polarization pointing up, the piezoelectric coefficient is inversed and the piezoelectric and flexoelectric polarization have opposite orientation (antiparallel). In this case, the magnitude of the total induced polarization is decreased, leading to a lower energy cost of deformation. Consequently, ferroelectric domains that are polarized up appear to be softer [1]. This phenomenon paves the way for non-destructive mechanical reading of ferroelectric polarization, whereby the polarity of ferroelectric domains can be determined only by mechanical means as long as strain gradients are applied, similar to those exerted by an AFM tip.

Contact Resonance Atomic Force Microscopy (CR-AFM) is an AFM mode that allows mapping differences in materials' stiffness in a non-invasive way and, at the same time, it also meets the criterion of applying inhomogeneous strain. As explained in Section 2.4, this CR-AFM mode probes the local elasticity of a material by measuring the resonance frequency of an AFM tip brought into strong mechanical coupling with the material. The resonance frequency of the system changes accordingly with the stiffness of the tip-sample contact: stiffer contacts lead to higher resonance frequencies while softer contacts lead to lower resonance frequencies. To perform CR-AFM, the whole system is excited mechanically (vibrated), while ensuring that the applied force by the AFM tip is low enough to avoid mechanical switching of the polarization. Here, all experiments were performed by an MFP – 3D Asylum AFM (Asylum Research – Oxford Instruments).

3.3.1 Mechanical reading of ferroelectric polarization in BaTiO_3 single crystals

Barium titanate is an archetypal ferroelectric material with well-known elastic constants and associated functional properties. The sample chosen for this study is a BaTiO_3 (100) single

crystal (CrysTec GmbH) which, after a phase transition in environmental conditions, shows a distribution of a/c domains on the surface as observed from PFM. Most of the observed ferroelectric domains are out-of-plane (c-domains), separated by diagonal stripes of in-plane polarization (a-domains). Full electromechanical characterization of BaTiO₃ single crystal is shown in **Figure 3.3** and **Figure 3.4**.

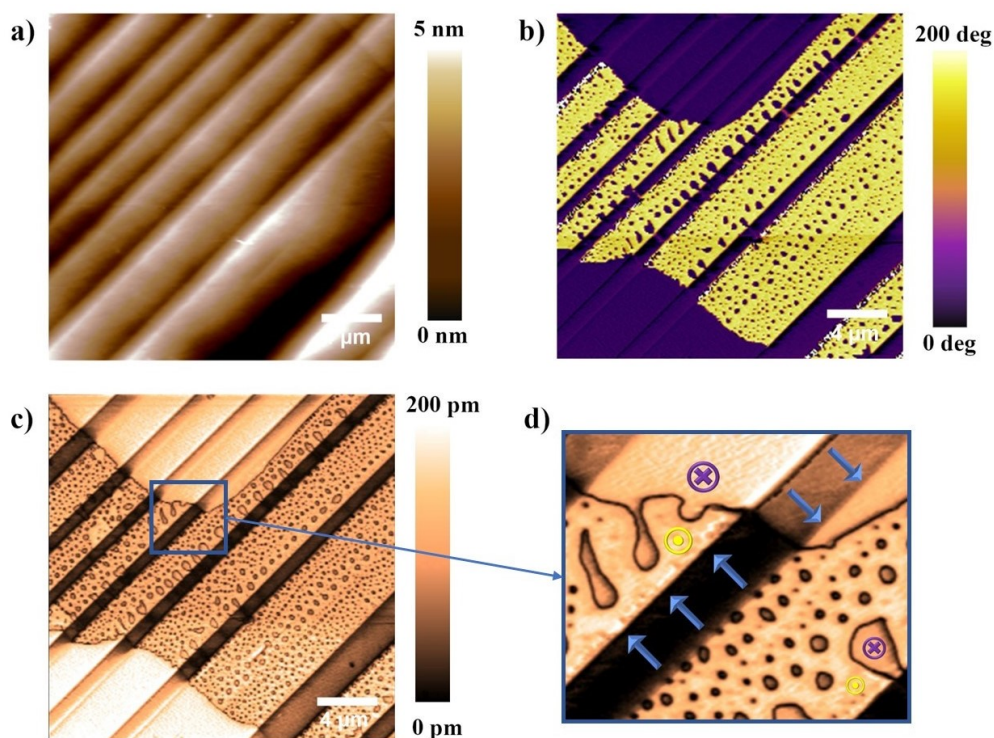


Figure 3.3: a) Topography in contact mode of BaTiO₃ single crystal in an area of 20x20 μm . b) PFM phase image where yellow color corresponds to domains with polarization pointing up and purple color denotes domains with polarization pointing down. Diagonal stripes correspond to in-plane polarization and are presented by arbitrary phase value. c) PFM amplitude image of the same area. C domains are presented with orange color while a domains with dark brown since the corresponding amplitude is almost zero. Domain walls, both ferroelectric and ferroelastic, are denoted with dark brown color. d) Zoomed area of PFM amplitude image where the polarization of the crystal is schematically presented. The tip used for this measurement is PPP-NCL type (Nanosensors; Schaffhausen, Switzerland) with a cantilever stiffness of $k \sim 45 \text{ N/m}$ and no coating. The ac voltage that excited the sample was 1V and the applied force was $\sim 1.12 \text{ N}$.

Figure 3.3 spans over a 20x20 μm area while **Figure 3.4** is a zoomed in scan of 7x7 μm . **Figure 3.3.a** shows the topography of the sample, measured in contact-mode AFM, which has a topography height variation of 5 nm resulting from the slope of the facets of the ferroelastic domains [10]. **Figure 3.3.b** shows the PFM phase of the sample. Out-of-plane polarized domains with opposite polarization show a phase difference of 180^o. Specifically, up-polarized domains correspond to yellow color and down-polarized domains to purple color. Diagonal stripes

correspond to in-plane polarized areas. Since the image corresponds to a vertical DART PFM measurement, the cantilever motion is only sensitive to vertical displacements, corresponding to sample expansion and contraction due to the electromechanical response of out-of-plane polarization. Hence, this measurement is insensitive to the lateral torsion of the cantilever that results from the electrical excitation of in-plane polarized domains and thus a-domains show an arbitrary PFM phase. Figure 3.3.c is the PFM amplitude of the same area. Amplitude gives information about the magnitude of the ferroelectric polarization; thus, domain walls with total zero polarization give null PFM amplitude and are observed as almost black lines in this figure. Additionally, in-plane polarized a domains will display low or null PFM amplitude in the out-of-plane direction (except for some cross-talk effects emerging from cantilever buckling motion), and consequently appear as dark brown in the amplitude PFM image, in contrast with the orange color of the out-of-plane c domains.

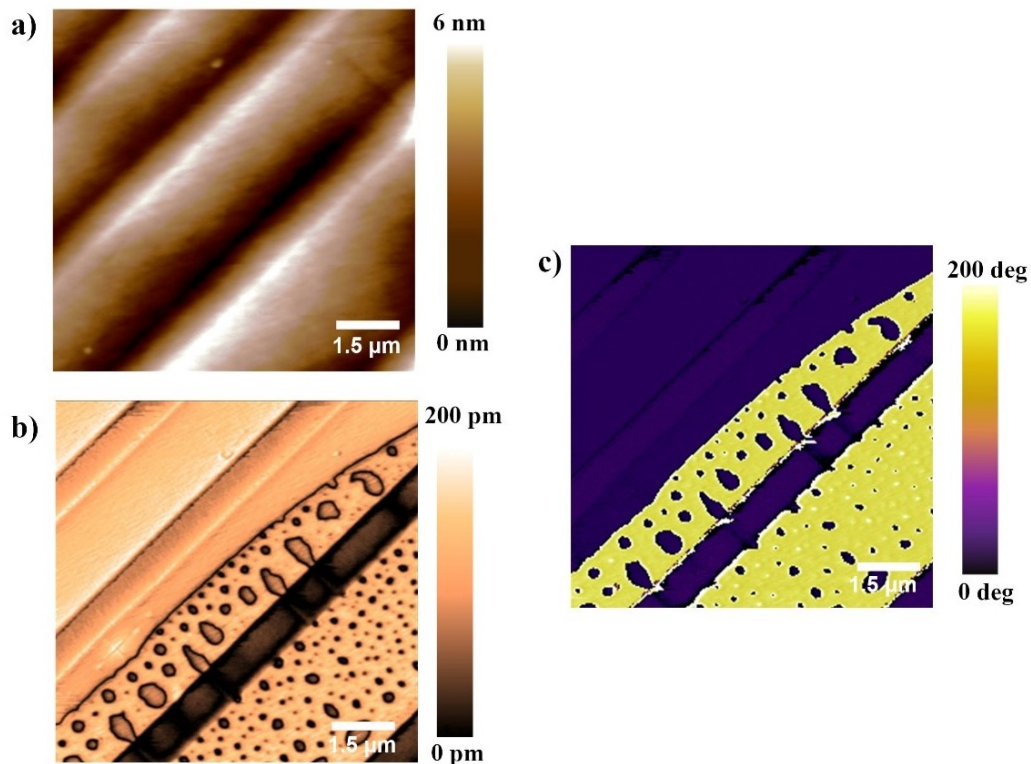


Figure 3.4: a) Topography in contact mode of BaTiO_3 single crystal in an area of $7 \times 7 \mu\text{m}$. b) PFM amplitude image of the same area. Domain walls, both ferroelectric and ferroelastic, are denoted with dark color. c) PFM phase image. Up-polarized domains are plotted in yellow color while down-polarized domains are purple. The image is obtained with vertical PFM, meaning that is insensitive to in-plane polarized domains. The tip used for this measurement is PPP-NCL type (Nanosensors; Schaffhausen, Switzerland) with a cantilever stiffness of $k \sim 45 \text{ N/m}$ and no coating. The ac voltage that excited the sample was 1V and the applied force was $\sim 1.12 \text{ N}$.

Figure 3.3.d shows a small part of the PFM amplitude image, where the different polarization domains are schematically represented. **Figure 3.4.a** to **Figure 3.4.c** correspond respectively to topography, amplitude, and phase of PFM measurements of the same material, in a smaller scan area. Altogether, both figures give a full electromechanical mapping of the domain orientation of a BaTiO₃ single crystal as the first step towards the complete functional characterization of any ferroelectric material.

Once the domain configuration is fully characterized, the next step is the measurement of the mechanical properties of oppositely-polarized c domains. As described previously mapping of mechanical properties is done by CR-AFM mode, where contact resonance frequency is proportional to the stiffness of the material, meaning that softer material correspond to lower values of contact resonance frequency. **Figure 3.5.a** shows the PFM phase of the area already shown in **Figure 3.3** and **Figure 3.5.b** shows the same area, as measured by CR-AFM.

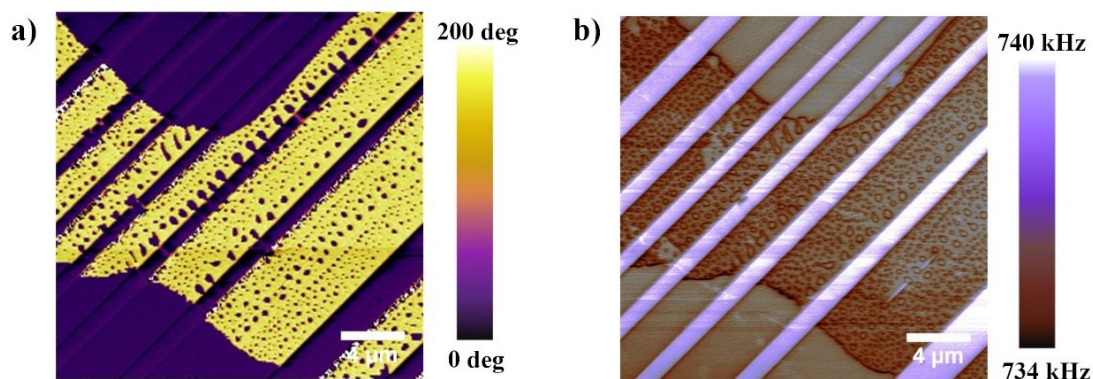


Figure 3.5: (a) PFM phase image of BaTiO₃ single crystal where yellow and purple color correspond to up and down-polarized ferroelectric domains respectively. b) Contact resonance frequency as measured by CR-AFM of the same area where differently polarized domains corresponding to different values of contact resonance frequency. The tip used for this measurement is PPP-NCL type (Nanosensors; Schaffhausen, Switzerland) with a cantilever stiffness of $k \sim 45$ N/m and no coating. The ac voltage that excited the sample was 1V and the applied force was ~ 1.12 N.

Figure 3.5.b shows that domains with different polarization orientation and direction lead to different values of contact resonance frequency, meaning that they have different mechanical stiffness. Diagonal stripes corresponding to a domains polarized in-plane, appear with the highest values of contact resonance frequency, meaning that they are indeed stiffer in the vertical direction (i.e., perpendicular to their polar direction). This result is expected as BaTiO₃ is known to be about 150% stiffer in the direction perpendicular to the polarization [11], and the phenomenon has been studied elsewhere [12]. In order to focus on the difference in stiffness between up and

down c domains, **Figure 3.6** depicts the same characterization of the BaTiO₃ single crystal, but in a scan area of 2.7x2.7 μ m.

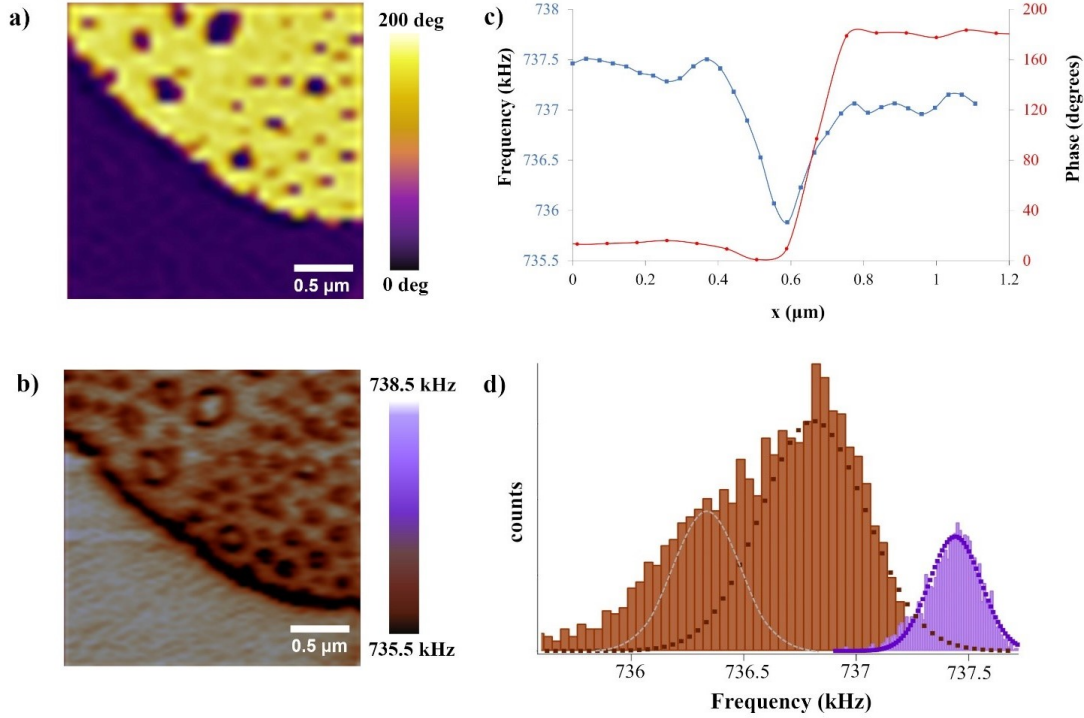


Figure 3.6: (a) PFM phase image of BaTiO₃ single crystal over a scan area of 2.7x2.7 μ m. Yellow color corresponds to ferroelectric domains with polarization pointing up and purple to polarization pointing down. b) CR-AFM image of the same area. c) Diagonal sections of images (a) and (b), demonstrating that shifts in contact resonance frequency of CR-AFM measurement coincides with the alternation of the ferroelectric polarization from pointing down (0 degrees) to pointing up (180 degrees). d) Histogram of image (b) showing the two mean values of contact resonance frequency for oppositely-polarized domains as well as a third peak that corresponds to domain walls. The tip used for this measurement is PPP-NCL type (Nanosensors; Schaffhausen, Switzerland) with a cantilever stiffness of $k \sim 45$ N/m and no coating. The ac voltage that excited the sample was 1V and the applied force was ~ 1.12 N.

Figure 3.6.a shows the PFM phase of BaTiO₃ single crystal. Following the regular code here, yellow color denotes domains with orientation of polarization up while oppositely-polarized domains are presented with purple color. **Figure 3.6.b** shows the contact resonance frequency of the same area, measured by CR-AFM, mapping the mechanical properties of the domains. The constant applied force during the experiment (as calculated on the basis of the calibrated elastic constant of the cantilever (k) and the deflection setpoint) was again ~ 1.12 μ N which should lead to relevant flexoelectric fields. The histogram of the CR-AFM shown in **Figure 3.6.d**, indicates that the distribution of values of contact resonance frequency is centered around two distinguishable positions; a first peak at 737.46 kHz which corresponds to domains with

polarization pointing down and a second one at 736.81kHz associated to up-polarized domains (although over imposed to a background tail at lower frequencies). The calculation of the mean values was done by fitting the distribution of values with a Gaussian equation. This shift in contact resonance frequency arises from the different nanomechanical properties of the domains, with down-polarized domains being stiffer than up-polarized domains. It is worth commenting that the peak of **Figure 3.6.d** corresponding to up-polarized domains is asymmetric due to a third peak with even lower mean value that corresponds to domain walls (as seen in **Figure 3.6.b**). This behavior is addressed in **Chapter 4** of this thesis. **Figure 3.6.c** shows the values of a diagonal section on the images of PFM phase (**Figure 3.6.a**) and CR-AFM contact resonance frequency (**Figure 3.6.b**). In the section of PFM phase, 0° correspond to c-down domains and 180° to c-up domains. The two sections show that shifts in contact resonance frequency of CR-AFM coincide with the switching of polarization from down to up and also that lower values of contact resonance frequency correspond to up-polarized domains, confirming the softness of c-up domains as compared with c-down domains.

The CR-AFM measurements of BaTiO₃ single crystal shown here indicate a difference in the nanomechanical response of oppositely-polarized ferroelectric domains, as well as they demonstrate the possibility of mechanical reading ferroelectric polarity in a non-destructive way. Now, the universality of this phenomenon and the performance range of this technique will be explored by studying the nanomechanical response of different ferroelectric materials with different morphologies.

3.3.2 Mechanical reading of ferroelectric polarization in BiFeO₃ thin films

The next material tested in this thesis was a BiFeO₃, one of the most extensively investigated material of the past decade due to its unique properties: it has both ferroelectric and antiferromagnetic ordering thus exhibiting multiferroic properties at room temperature[13–15] and moreover it is a lead-free piezoelectric material. Because of its high Curie temperature ($T_c \approx 850^\circ\text{C}$) and a giant polarization value confirmed theoretically and experimentally [16–18], BiFeO₃ is a promising material for device applications [19–21]. From the point of view of generalizing our observations and conclusion, BiFeO₃ was deemed a good complementary material because, whereas the ferroelectric polarization of BaTiO₃ comes from an off-centering of the B-site cation (Ti^{+4}), the polarization of BiFeO₃ comes from an off-centering of the A-site cation (Bi^{+3}). Should

the mechanical asymmetry be observed in both cases, it would indicate that the origin of the effect is independent of the origin of ferroelectric polarization.

The ferroelectric properties of BiFeO_3 arise from its unit cell structure [22,23]. The structure of BiFeO_3 is characterized by two distorted perovskite unit cells connected along their body diagonal. A displacement of the Bi ions with respect of the FeO_6 octahedral is responsible for the non-centrosymmetric structure, and consequently the ferroelectric behavior [24]. The epitaxial strain in BiFeO_3 thin films is responsible for phases with different symmetries [25,26] and the orthorhombic phase is stabilized in BiFeO_3 thin films with strain engineering [27,28]. The ferroelectric polarization lies along [111] with eight possible variants [29]. The samples tested in this thesis, were BiFeO_3 (111) thin films of 20 nm grown by pulsed laser deposition (PLD) on a LaSrMnO_3 buffer layer on SrTiO_3 substrate.ⁱ Their structure is rhombohedral and, due to the epitaxial clamping to the substrate, the only possible direction of the ferroelectric polarization is perpendicular to the surface plane.

In this case, the as-grown ferroelectric polarization of the film is homogeneous and pointing down, as confirmed by the ferroelectric hysteresis loops performed on the sample (**Figure 3.7**). Changes in the PFM phase as a function of the applied voltage measured by SS-PFM give information about the orientation of the ferroelectric polarization. In this case, the first branch of the hysteresis curve shows that by applying a positive voltage to the sample, the phase does not change value, meaning that the sample's polarization is pointing down. Additionally, PFM phase gives information about the coercive field of the material (4 V for this film) and the imprint of the film. In this film, the PFM phase is not fully symmetric with respect to the applied voltage, meaning that there is a favorable orientation of ferroelectric polarization: it is harder (more voltage needed) to switch the polarization from pointing down to pointing up as there is already a built-in bias in the film. We cannot exclude the possibility that this built-in bias does not insert an asymmetry in mechanical response of the material and thus flexoelectricity is not the only factor that contributes to a distinct mechanical behavior of oppositely-polarized domains. Finally, the PFM amplitude gives information about the magnitude of the piezoresponse of the material and has the typical butterfly shape indicating ferroelectric switching.

ⁱThe sample was grown by the group of Prof. Ramamoorthy Ramesh at Berkeley University of California, USA and provided by Prof. Gustau Catalan.

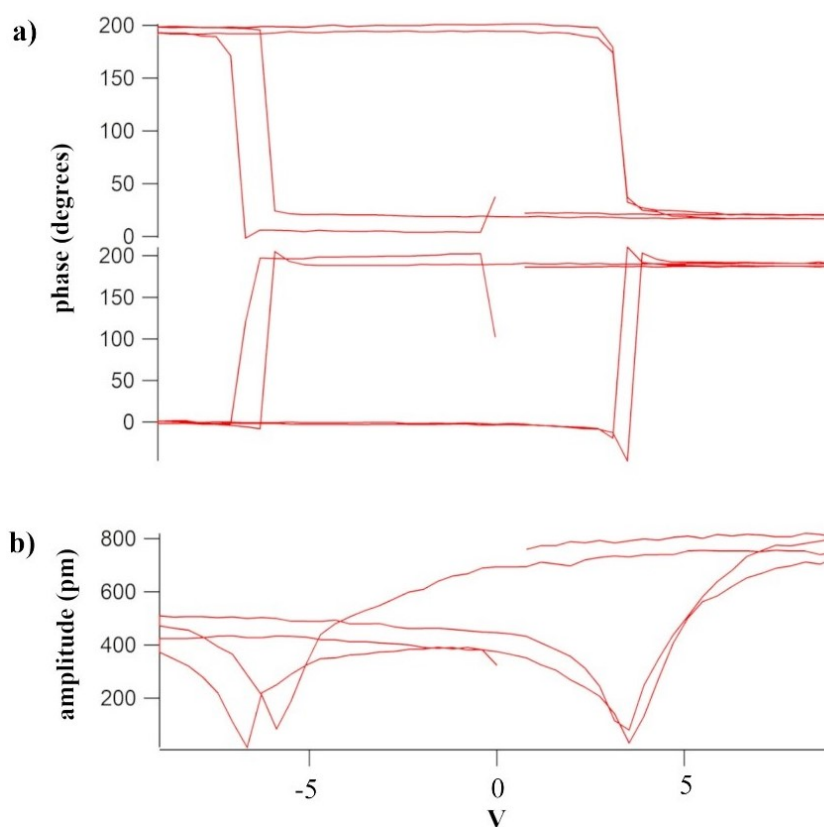


Figure 3.7: PFM hysteresis loop of BiFeO_3 (111)/LSMO/STO thin film of 70 nm as obtained by DART PFM. a) PFM phase as a function of applied voltage, showing that the as grown state of the film is polarized down. b) PFM amplitude with the typical butterfly shape indicating the ferroelectric switching. The tip is a conductive with PtIr coating with cantilever stiffness of ~ 45 N/m (PPP-NCHPt Nanosensors; Schaffhausen, Switzerland), while the applied force is ~ 630 nN.

In order to track the asymmetry of the mechanical properties as a function of the polarization direction, linear domains were written by ferroelectric lithography, i.e., by applying a *dc* voltage to tip while scanning in contact mode over the sample. **Figure 3.8** shows the full electromechanical characterization of the ferroelectric properties of the BiFeO_3 (111) thin film after the ferroelectric lithography.

Figure 3.8.a shows the topography of the film as measured in contact. The roughness of the film is ~ 800 pm and, despite the roughness, the topographical features are not correlated with the different ferroelectric domains. **Figure 3.8.b** shows the PFM amplitude as measured by DART PFM. Domain walls correspond to the lowest values of amplitude, as their total polarization is zero. Domains with opposite polarization in an ideal PFM measurement, should correspond to the same value, since the PFM amplitude is proportional to the magnitude of ferroelectric polarization, independently of its sign. However, there is a difference of few pm

between up and down domains (~ 10 nm as measured by the section of the image), also in agreement with the hysteresis cycles. Occasionally, this difference arises from technical artefacts modulated by the long-range electrostatic interactions between the body of the cantilever and the polarized domains that can insert asymmetries in the measurable values of amplitude [30,31]. Additionally, although this behavior can be eliminated by using stiffer cantilevers, the laser position on the back of the cantilever can significantly affect the amplitude measurements too [31]: in such cases, to nullify this effect the laser spot should be positioned as close as possible to the tip base position as possible, on the back of the cantilever, so that the detection of the cantilever motion corresponds to the net motion of the tip. Finally, the hysteresis loop of BiFeO_3 film (**Figure 3.7**) shows that there is a strong built-in bias in the film that may also contribute to this asymmetry in amplitude between oppositely-polarized domains. In any case, the observed asymmetry in the amplitude agrees with that measured by the hysteresis loops. **Figure 3.8.c** shows the PFM phase of the same area as measured by DART PFM. In this image, areas with opposite polarization correspond to a phase difference of 180° .

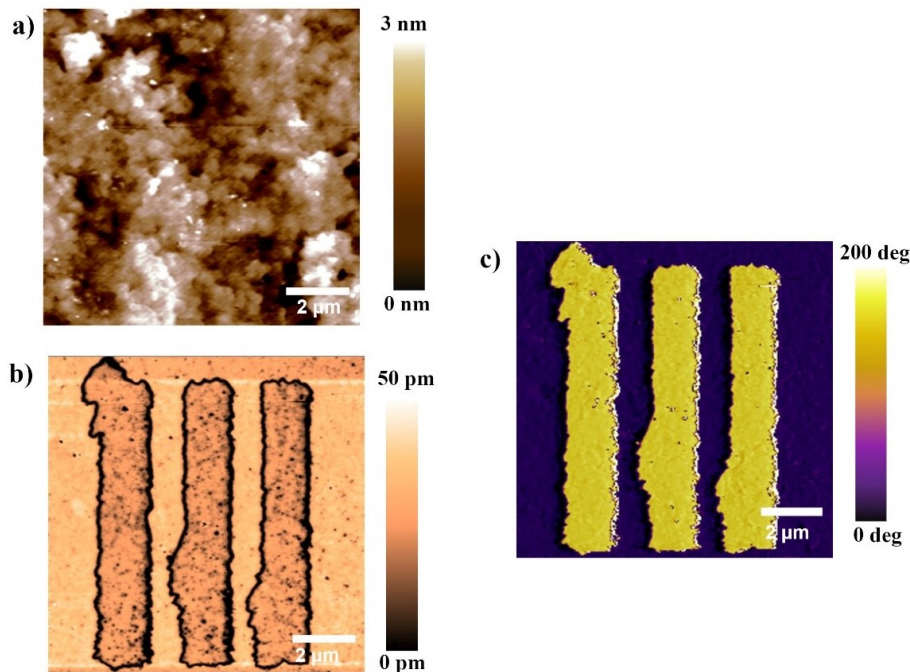


Figure 3.8: a) Topography in contact mode of BiFeO_3 (111)/LSMO/STO thin film of 20 nm. The scan area is 8×8 nm and the roughness of the film is ~ 800 nm. b) PFM amplitude of the same area. Three stripe - domains of opposite polarization were electrically written by applying -8 V through the AFM tip. c) PFM contact resonance frequency of the same area. d) PFM phase image. Opposite out-of-plane polarized domains are represented with yellow (up) and purple (down). This measurement was performed with the same tip as the hysteresis loops (**Figure 3.7**) (PPP-NCHPt Nanosensors; Schaffhausen, Switzerland), with ac voltage of 1 V and applied force of ~ 600 nN.

PFM phase image is used to map the electrically written ferroelectric domains of the film. To map the mechanical properties of the same domains, CR-AFM measurements were performed on the same area. **Figure 3.9** shows the electromechanical and mechanical measurements done on the electrically written ferroelectric domains of BiFeO₃, over a scan area of 5x8 μm .

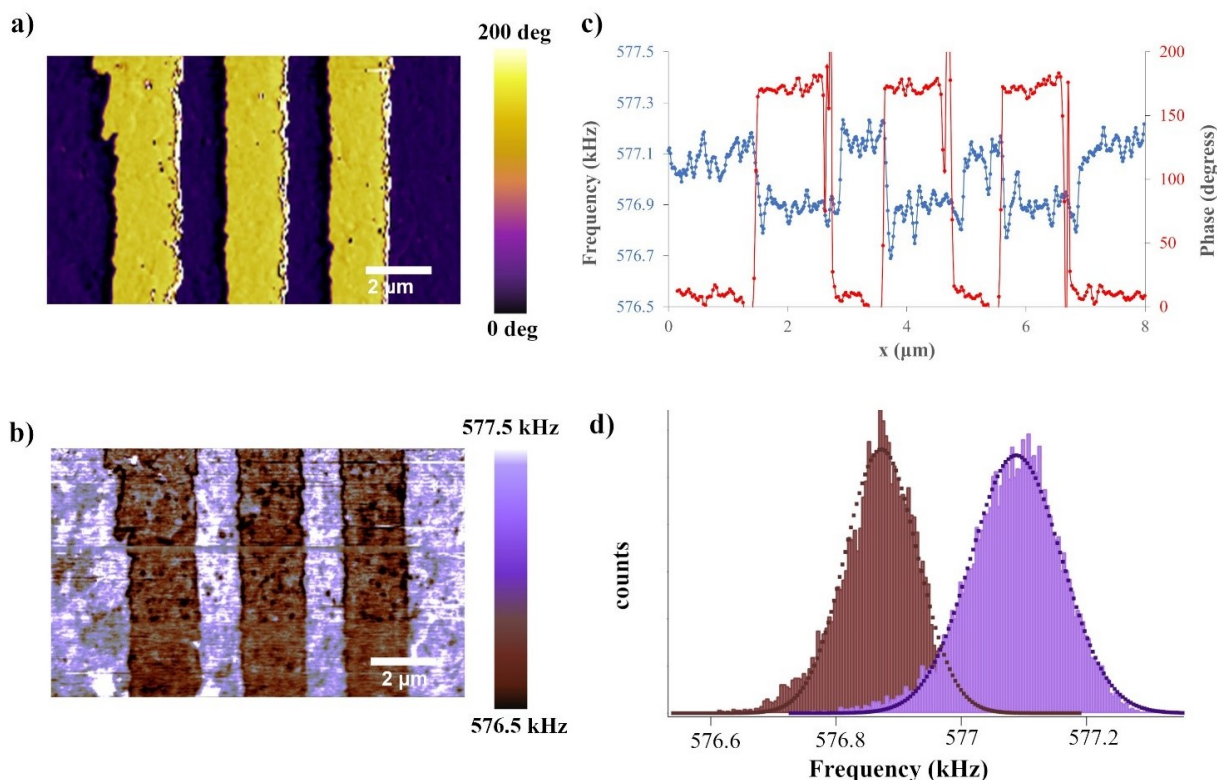


Figure 3.9: a) PFM phase image of BiFeO₃ thin film with domains opposite polarized out-of-plane. Yellow and purple color correspond to domains polarized up and down respectively. b) CR-AFM image of the same area, where domains with different polarization correspond to different contact resonance frequency values, meaning that they possess different mechanical properties. c) Cross section in red of PFM phase image (a) and in blue CR-AFM image (b) showing that changes in polarization, as measured by the PFM phase coincide with changes in the contact resonance frequency and consequently, mechanical properties of the domains. d) Histogram of CR-AFM measurement (c), demonstrating that contact resonance frequency has two mean values. The tip used for the CR-AFM measurement is a stiff tip with PtIr coating on the reflecting side of the cantilever (PPP-NCLR Nanosensors; Schaffhausen, Switzerland). The stiffness of the cantilever is ~ 45 N/m and the applied force ~ 1.12 μN .

Figure 3.9.a shows the PFM phase image, as measured by DART PFM, where yellow and purple correspond to domains polarized up and down respectively. **Figure 3.9.b** is the CR-AFM measurement of the same area. It is observed that ferroelectric domains with opposite polarization correspond to different values of contact resonance frequency. Specifically, up-domains correspond to lower values of contact resonance frequency, as compared with down-polarized domains, and thus they are softer.

To verify that changes in contact resonance frequency of CR-AFM are concurrent with changes in direction of ferroelectric polarization, sections of both images, PFM phase and CR-AFM, are shown in **Figure 3.9.c**. Sections are along the x-axis of the images, demonstrating that lower values of contact resonance frequency correspond to domains with polarization up, confirming that up-polarized domains have softer nanomechanical properties than down polarized domains. Finally, **Figure 3.9.c** is the histogram of the CR-AFM measurement (**Figure 3.9.b**). This histogram demonstrates that contact resonance frequency has two mean values, 576.85 kHz and 577.1kHz. Again, shifts in contact resonance frequency seem to be directly correlated with difference in mechanical properties of the material and therefore, it confirms the distinct mechanical properties of opposite polarized ferroelectric domains in a completely different scenario: artificially electrically switched multiferroic domains in rhombohedral thin films. Still, considering the observed asymmetry of the hysteresis cycles, one cannot rule out some additional contribution arising from some coupling with the build-in field or simply from the different total polarization magnitude for the electrically written up domains (about 20% smaller than for up domains) - which in this case it could also indicate an incomplete switching of the polarization through the thin film volume. Indeed, since the up-polarized domains are closer to coercivity they should therefore naturally appear softer since they might be “easier” to switch. On the other hand, trying to apply a dc voltage to the tip during the CR-AFM measurements to compensate for the build-in field could also lead to undesired electrostatic enhanced interactions perturbing tip dynamics. So the best option to evaluate the impact on this build-in field on the mechanical asymmetry of the ferroelectric domains, is to check the behavior in samples showing the opposite scenario, as the ones shown in the following section.

3.3.3 Mechanical reading of ferroelectric polarization in PbTiO_3 thin films

The last material used for the study of mechanical properties of ferroelectrics is PbTiO_3 thin films, in this case with a thickness of 20nm grown directly on a SrTiO_3 substrate by molecular-beam epitaxy (MBE).ⁱⁱ PbTiO_3 is a well-known ferroelectric material with a diverse range of applications, such as sensors and piezo actuators due to its exceptional structural and electrical properties [32]. It has a tetragonal perovskite structure at room temperature and Curie temperature above 490 °C [33,34]. In PbTiO_3 thin films, the orientation of their ferroelectric polarization is constrained by

ⁱⁱThe sample was kindly provided by Dr Eric Langenberg at Cornell University, USA.

the substrate [35] and in the case of SrTiO_3 substrate the polarization of the film is perpendicular to the surface of the film (out-of-plane polarization) [36].

The as grown ferroelectric state of the film was explored by PFM hysteresis loops. **Figure 3.10.a** shows the PFM phase as a function of the applied voltage. Shifts in phase of 180° degrees, which are indicative of ferroelectric switching, appear after the application of almost 4 Volts, showing that the as grown state of the ferroelectric film is pointing up and the coercive field is also 4 Volts. Shifts in phase are not symmetric with respect to the voltage showing that also in this film there is an imprint and an associated build-in field, in this case favoring an up-polarized state. Finally, **Figure 3.10.b** shows the changes in PFM amplitude, which are indicative to the magnitude of ferroelectric polarization.

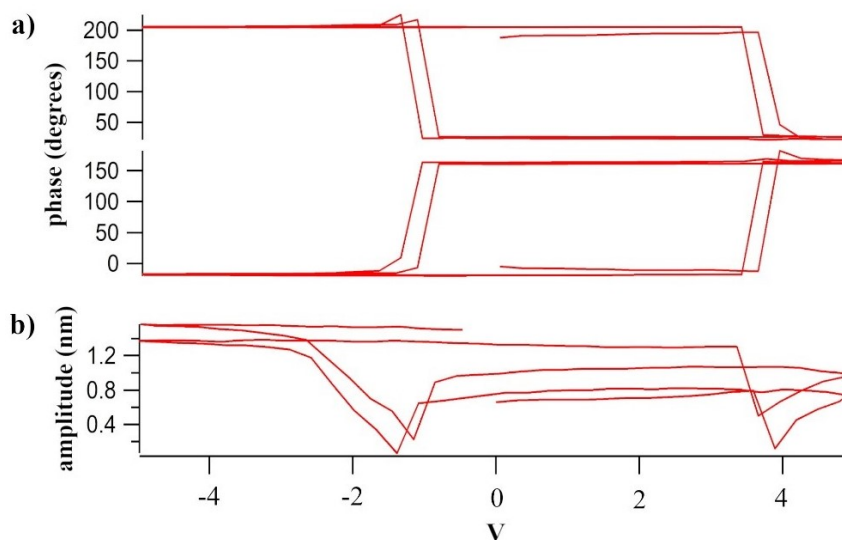


Figure 3.10: PFM hysteresis loop of PbTiO_3 thin film. a) PFM phase as a function of applied voltage, showing that the as grown state of the film is polarized up. b) PFM amplitude showing the piezoresponse magnitude for every state of polarization and indicating the ferroelectric switching. The tip used was a conductive tip with PtIr coating and contact stiffness $\sim 3 \text{ N/m}$ (PPP-EFM Nanosensors; Schaffhausen, Switzerland) and the total force applied on the sample was $\sim 80 \text{ nN}$.

Ferroelectric domains of opposite polarization were created by ferroelectric lithography after the application of an external dc voltage of 5 Volts through the tip. Afterwards, full electromechanical characterization of the film was performed by vertical DART PFM. **Figure 3.11.a** shows the topography of the sample as measured in contact in a scan area of $7 \times 7 \mu\text{m}$. The roughness of the film is calculated around 145 pm. PFM amplitude is shown in **Figure 3.11.b**. This image shows the pattern of the electrically written ferroelectric domains, with opposite polarization than the as grown film. Note that here, since the sample shows an as grown

up-polarized monodomain state, oppositely to the previous section, the domains are electrically switched to down polarization by applying a positive voltage. Domain walls have the smaller values of amplitude, as expected, as they correspond to zero ferroelectric polarization. However, similar to BiFeO₃ (111) thin films, here domains appear to have distinct response in PFM amplitude as well. As explained in the previous section, this effect can have different origins, including electrostatic artifacts. On one hand, since in this measurement the cantilever is softer than the one used for BiFeO₃ thin films, it is affected to a higher extent by the electrostatic forces leading to stronger artefacts if this is the case. On the other hand, the electrically written domains can trap some injected charge due to the ferroelectric lithographic process that enhances the PFM amplitude signal. Remarkably, the PFM amplitude of the switched domains in this sample is opposite to the one of the previous samples. **Figure 3.11.c** corresponds to the PFM phase image. Oppositely polarized domains correspond to areas with a phase difference of 180°, so phase image indicates that the domains shown here are oppositely polarized.

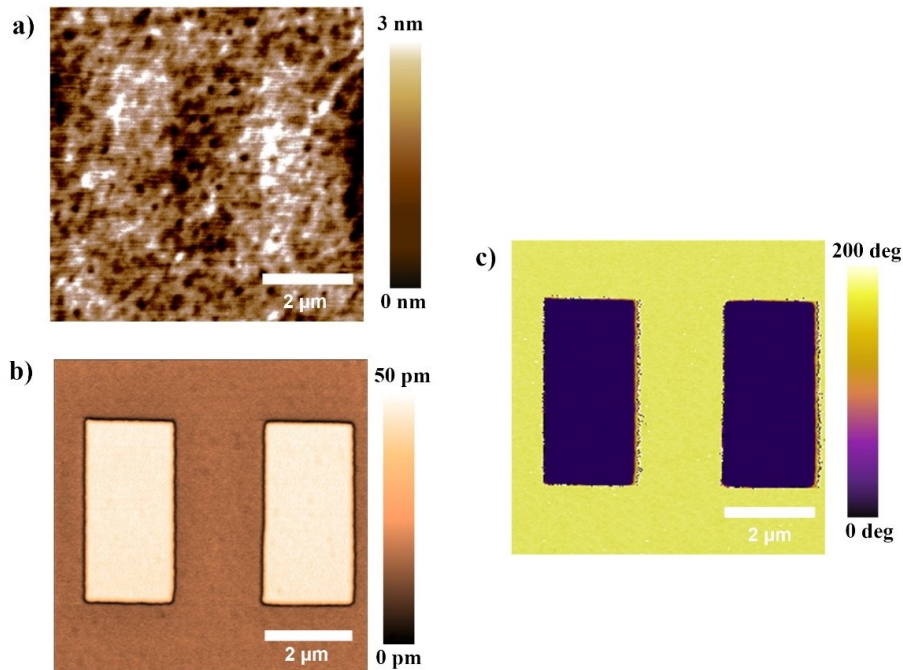


Figure 3.11: . a) Topography in contact of PbTiO₃ thin film on SrTiO₃ substrate and thickness of 20 nm. The roughness of the film is ~ 145 pm. The scan area is $7 \times 7 \mu\text{m}$. b) PFM amplitude showing the orthogonal domains created by ferroelectric lithography after the application of 5 Volts through the AFM tip. c) PFM phase image where domains with opposite polarization show a phase difference of 180 degrees. Yellow corresponds to polarization pointing up and purple to polarization pointing down. The measurement was performed with a conductive tip with PtIr coating and cantilever stiffness ~ 3 N/m (PPP-EFM Nanosensors; Schaffhausen, Switzerland), the total force applied on the sample was ~ 40 nN and the ac voltage used to excite the sample was 1.5 V.

The study of the mechanical properties of domains with opposite ferroelectric out-of-plane polarization by CR-AFM is performed at the same area of the PbTiO_3 thin film and is shown in **Figure 3.12**.

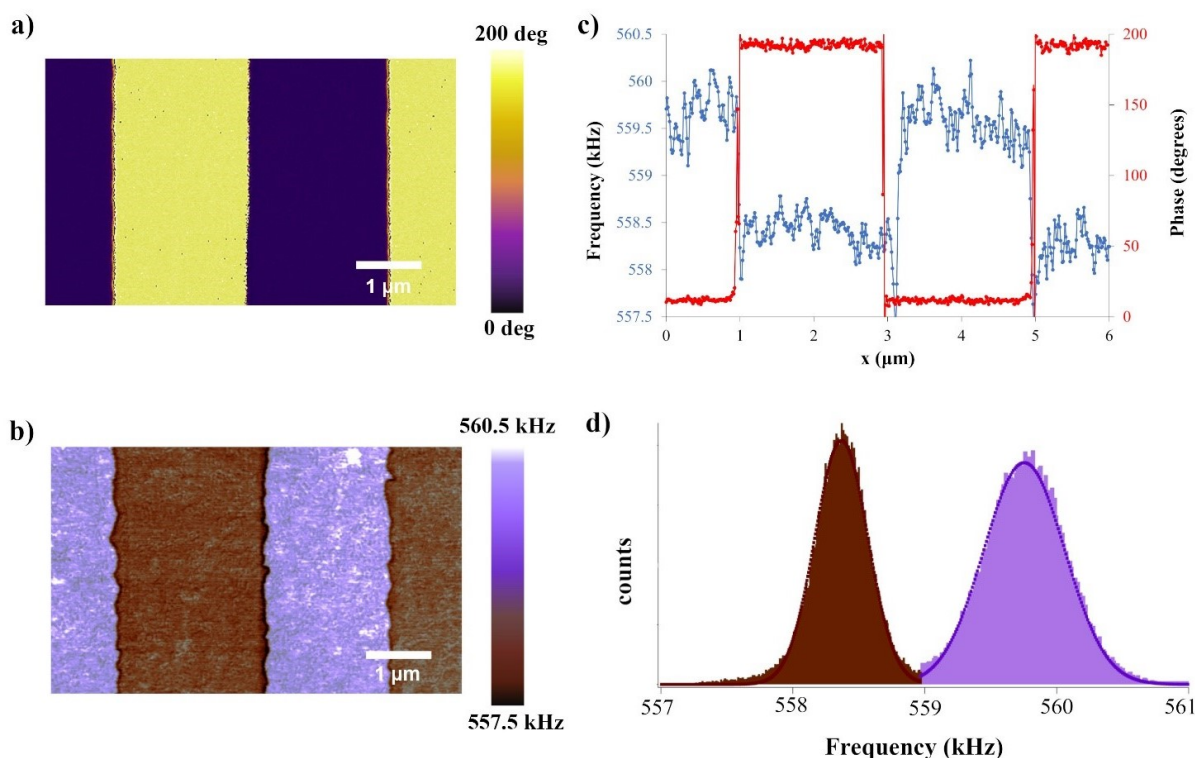


Figure 3.12: a) PFM phase image of a PbTiO_3 thin film on a SrTiO_3 substrate. PFM measurements were done with a conductive soft tip with PtIr coating (PPP-EFM Nanosensors; Schaffhausen, Switzerland). The cantilever stiffness was ~ 3 N/m, the applied force ~ 85 nN and the amplitude of the ac voltage was 1 V. Yellow color corresponds to ferroelectric polarization pointing up and purple color to ferroelectric polarization pointing down. b) CR-AFM image of the same area demonstrating the mechanical properties of the domains. The tip used for this measurement was a stiff conductive tip with PtIr only on the deflection side of the cantilever (PPP-NCLR Nanosensors; Schaffhausen, Switzerland). The stiffness of the cantilever, calculated through experimental calibration, was 38 N/m and the applied force on the sample was ~ 560 nN. Down-polarized domains correspond to higher values of resonance frequency denoting higher stiffness. c) Cross section of the PFM phase image (a) and CR-AFM image (b) demonstrating that down-polarized domains correspond to lower contact resonance frequency values, while down domains to higher values of frequency. d) Histogram of CR-AFM image (b), used to calculate the mean value of contact resonance frequency for each domain.

Figure 3.12.a shows the PFM phase image of the PbTiO_3 thin film, focused on an area including two domains with opposite out-of-plane polarization. Yellow corresponds to domains polarized up and purple to electrically written down polarized domains. **Figure 3.12.b** shows the CR-AFM image of the same area. In CR-AFM image (**Figure 3.12.b**) opposite domains correspond to different values of contact resonance frequency. Contact resonance frequency for up-domains is lower than contact resonance frequency for down-domains, and since frequency is

directly correlated with the mechanical properties of the sample, this change is translated into softer mechanical properties of up domains compared to down domains. Cross sections of both PFM and CR-AFM measurements, as shown in [Figure 3.12.c](#), demonstrate that the change in phase from 180 to 0 degrees (indicating a change of polarization direction from up to down) coincides with change in contact resonance frequency of CR-AFM, from lower values to higher, proving the correlation between polarization direction and mechanical stiffness. Finally, **Figure 3.12.d** shows the histogram of CR-AFM measurement of the film. From the histogram, by fitting the distribution of values with a Gaussian equation, the two mean values of contact resonance frequency are calculated. Domains with polarization pointing up have a mean contact resonance frequency of 558.45 kHz, while for down domains, the mean value is 559.83 kHz.

The above results on PbTiO_3 are in full agreement with the previous measurements obtained for BiFeO_3 , despite the different crystallographic structures and the different native polarization orientation and build-in fields. In this sense, this confirms that the bias observed in the hysteresis cycles created by the build-in field favoring a certain polarization orientation through the whole thin film thickness can be neglected in terms of its impact in the elastic mechanical properties at the surface. Moreover, it confirms that the inhomogeneous deformation induced asymmetry on oppositely-polarized ferroelectric domains results into distinct mechanical properties of the ferroelectric domains also for thin films of a ferroelectric materials with tetragonal crystallographic structure and electrically written domains with down polarization, steering towards a universal phenomenon: up-polarized domains as measured at the nanoscale with an AFM tip are softer than down-polarized domains, due to the coupling of flexoelectricity and piezoelectricity.

At this point, this phenomenon is well established as confirmed in three different materials. The materials have different morphology, from single crystal (BaTiO_3) to thin films (BiFeO_3 and PbTiO_3) as well as different origin of ferroelectric polarization: A-site off-centering for BaTiO_3 and B-site off-centering for BiFeO_3 . Additionally, the crystallographic orientation of the ferroelectric polarization in the thin films is also different between BiFeO_3 (111) and PbTiO_3 (001). Moreover, the observed behavior is consistent for spontaneously formed and electrically written domains in both directions, switched down in as grown-up domains and switched down in as-grown up-polarized thin films: in every case, the mechanical response of oppositely-polarized domains is distinct. So altogether, it is proven that this mechanism enables the mechanical reading of ferroelectric polarization in a non-destructive, non-invasive way, via CR-AFM.

3.3.4 Advantages of mechanical reading of ferroelectric polarization by CR-AFM

To summarize, the most common method to characterize the mechanical properties of ferroelectric materials is nanoindentation. This technique is simple and convenient; an indenter tip is pushed into the material and the load and displacement at the tip give information about the mechanical properties of the material, such as hardness and elastic modulus. However, the induced strain is large enough to cause not only elastic but also plastic deformation on the material, resulting to the destruction of the sample. On the other hand, in CR-AFM the applied strain is on the regime of elastic deformation, causing no damage on the sample, and moreover due to its nature, it is highly surface sensitive. Another advantage of CR-AFM technique is that there is no voltage applied on the sample. In ferroelectrics, polarization is manipulated by external voltage and thus, a characterization technique that applies voltage on the sample, endangers alternating the ferroelectric polarization or properties of the sample, while measuring. Nowadays, devices and memories are based on ferroelectrics, with domains polarized up and down to be used as information bits (“0” or “1”). In this chapter, it is demonstrated that mechanical reading of ferroelectric polarization is possible in a wide range of materials and backgrounds. Mechanical reading of ferroelectric polarization, with no voltage applied, combined with mechanical writing of ferroelectric polarization, can be revolutionary on these types of devices and may open further fascinating possibilities for mechanical treatment of ferroelectric materials.

3.4 Size dependence of mechanical reading

Scrutinizing the results shown in the previous section, one may notice that the contrast observed in the mechanical response between up and down-polarized domains strongly differs as a function of not only the sample but also the experimental parameters. While opposite polarized domains in BaTiO₃ single crystal display a shift in the contact resonance frequency of about 650 Hz, the difference in the contact resonance frequency observed for thin film of PbTiO₃, reaches about 1380 Hz. Since mechanical asymmetry emerges from the coupling of flexoelectricity with piezoelectricity, determination of the AFM tip-induced strain gradients in each case constitutes a primary concern to account for the flexoelectric coupling into the mechanical attributes. While

the magnitude of effect depends on the flexoelectric coefficient and the induced strain gradients as a function of the load, the total level of asymmetry (i.e., contrast over an observed magnitude) should depend on the relative volume of sample affected by flexoelectricity vs the total volume of sample sensed.

On the experimental front, in order to account for the magnitude of the phenomena, tip radius and applied force are the main factors that determine the induced strain gradients for a chosen material. Regarding tip radius, it is known that tip suffers severe wearing effects promoted by the continuous scanning over the surface in contact mode [37,38]. For tips used in CR-AFM measurements (PPP-NCL Nanosensors; Schaffhausen, Switzerland), stabilization of the tip radius is predicated in the order of ~ 70 nm, upon our observations. After AFM experiments in contact mode, tips were analyzed by scanning electron microscopy (SEM). **Figure 3.13** demonstrates an indicative image of an AFM tip before and after contact resonance experiments, as probed by SEM.

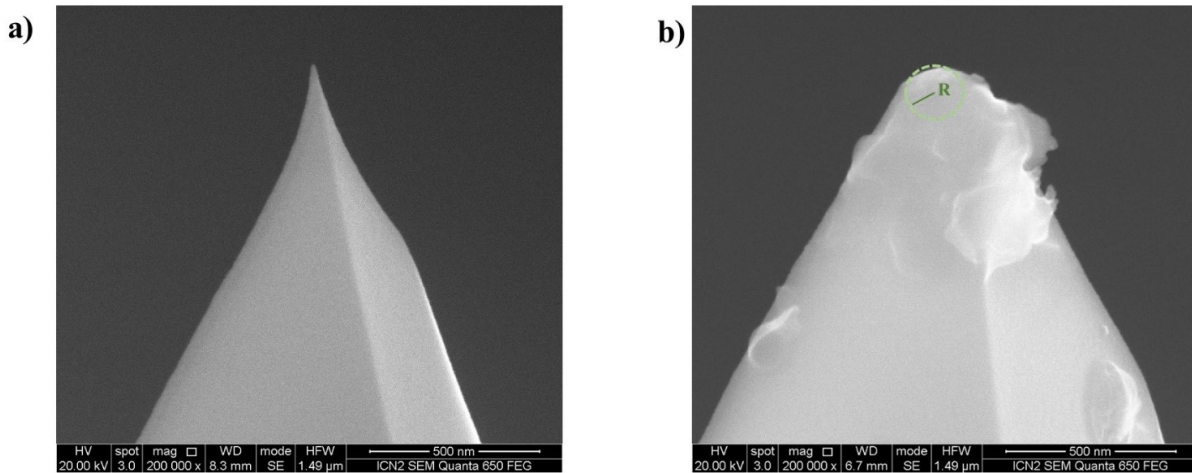


Figure 3.13: SEM image of AFM tip before (a) and after (b) performing series of experiments in contact mode, evidencing tip wearing. The radius of the unused tip is few nm while the contact radius of the tip after the experiments is calculated to be about ~ 70 nm. The type of cantilever is PPP-NCL (Nanosensors; Schaffhausen, Switzerland) with no coating and cantilever stiffness $k \sim 45$ N/m.

In this study, in order to minimize the tip effect, the same type of cantilevers was used for all experiments under the same applied forces in the range of $F \in [900 - 1000]$ nN, with a slight fluctuation among the different experiments. Taking into account all the above, it is considered that the load is very similar in all the experiments and, given that all materials studied here are perovskites with similar elastic constants (Young's moduli in the range of 100-170 GPa [11,39,40]), the induced strain gradients should be within the same order of magnitude for every

material studied.

Another major factor that should be taken into consideration to explain the observed difference in the mechanical responses of different materials, is the flexoelectric coefficient. The total induced flexoelectric field, under strain gradients, is defined as [41]:

$$E_{flexo} = f \frac{\partial s}{\partial z} \quad (3.4)$$

where f is the flexocoupling coefficient and $\partial s/\partial z$ the strain gradient. Assuming that the strain gradient is of the same order of magnitude in all cases, the flexocoupling coefficient should be examined. For BaTiO₃ single crystal at room temperature, a flexocoupling coefficient of $f = 7$ V has been reported [42]. For PbTiO₃ on the other hand, the reported flexocoupling coefficient is of about $f = 5$ V [43]. Although BaTiO₃ single crystal demonstrate higher flexocoupling coefficient, under the same magnitude of strain gradients, the induced asymmetry in mechanical response appears enhanced in case of PbTiO₃ thin film, which is the opposite of what would be expected from a comparison from their flexocoupling coefficients –and even more so if the flexoelectric coefficients (flexocoupling multiplied by permittivity) are considered, given that the permittivity of BaTiO₃ single crystals is orders of magnitude larger than that of PbTiO₃ thin films. Thus, possible differences in the flexocoupling coefficient and strain gradients cannot explain the observed contrast in the contact resonance frequency of about one order of magnitude, and further elements need to be considered.

In this sense, Abdollahi [4] had predicted that the asymmetry induced by the coupling of piezoelectricity and flexoelectricity is size dependent. Based on this, we could expect an enhancement of the contrast due to the reduction of the size of the sample. In order to investigate a possible sample size dependence of the observed effect, it is crucial to exclude the dependence of the mechanical response on the flexocoupling coefficient. Thereby, experiments are performed on thin films of the same material but with different thicknesses. More specifically, mechanical measurements were performed on PbTiO₃ thin films, deposited on SrTiO₃ substrates, with thicknesses of 20 nm and 50 nm respectively, under otherwise identical experimental parameters (i.e., same tip and same applied force for each case).

3.4.1 Mechanical reading of ferroelectric polarization in PbTiO_3 thin films as a function of thickness

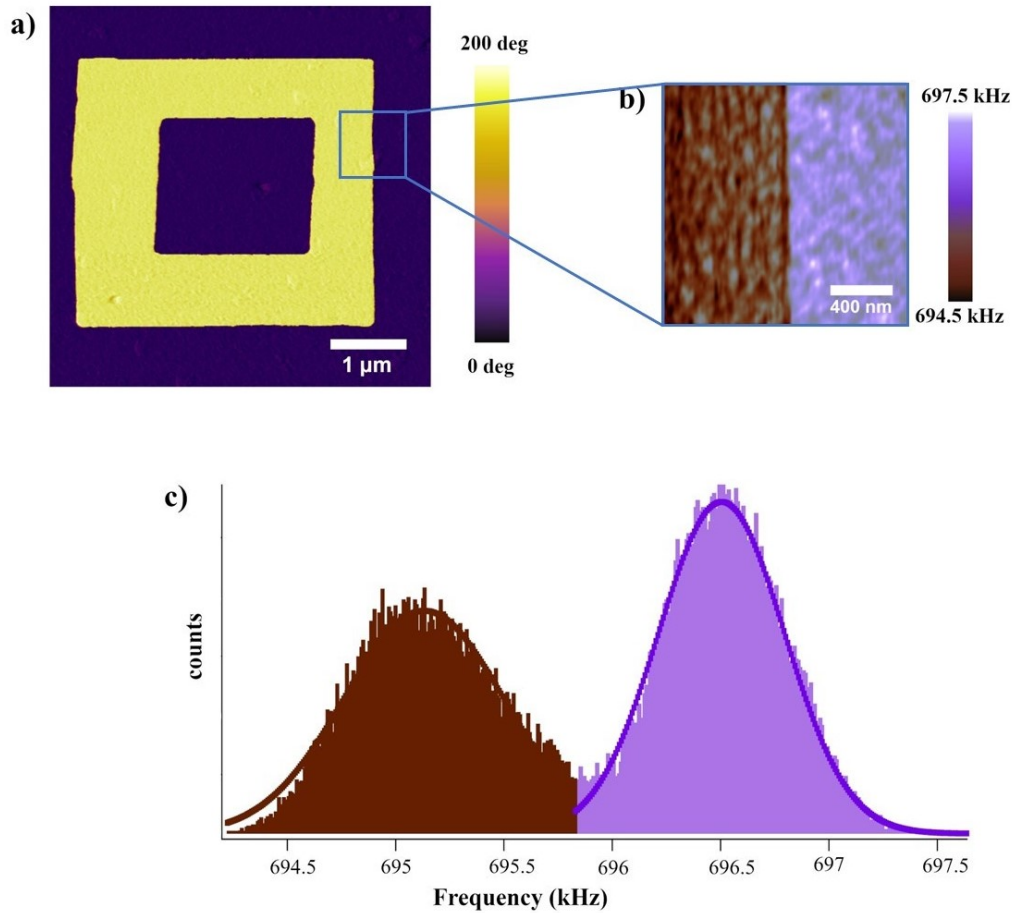


Figure 3.14: a) PFM phase image of a PbTiO_3 thin film grown on an SrTiO_3 substrate with a thickness of 50 nm, denoting the polarization direction. Areas polarised up and down are shown with yellow and purple color respectively. The tip used for the PFM measurement had stiffness of ~ 2 N/m (PPP-EFM Nanosensors; Schaffhausen, Switzerland), and an overall PtIr coating. The ac voltage was 1V and the applied force ~ 50 nN. b) The corresponding CR-AFM in a zoomed in area showing a significant shift of the measured contact resonance frequency to lower frequencies for up domains. CR-AFM experiments were done with a stiffer cantilever (PPP-NCL Nanosensors; Schaffhausen, Switzerland), with cantilever stiffness ~ 45 N/m and no coating. c) Histograms of the CR-AFM signal for the up and down domains respectively, denoting a relative shift of $\Delta f = 1.38$ kHz among opposite polarized domains.

Figure 3.14.a corresponds to a PFM phase image of a PbTiO_3 film of 50 nm thickness. As in the rest of this thesis, yellow and purple colors correspond to ferroelectric domains polarized up and down respectively. The domains were created electrically, through ferroelectric lithography, with the application of a dc voltage of ± 9 Volts through the tip. CR-AFM measurements were performed at the same area, and a corresponding zoom in is depicted in **Figure 3.14.b**. As expected, down-polarized domains show higher resonance frequencies, illustrating a stiffer

nanomechanical response as compared to up-polarized domains. To be able to quantify this difference in contact resonance frequency between oppositely polarized domains, histograms of the corresponding signal were analyzed. Histograms display the distribution of the values over the whole image and the mean value of them is calculated through Gaussian equations. As illustrated in **Figure 3.14.c**, contact resonance frequency values between up and down-polarized domains of 50 nm of thickness show a mean shift of 1,38 kHz.

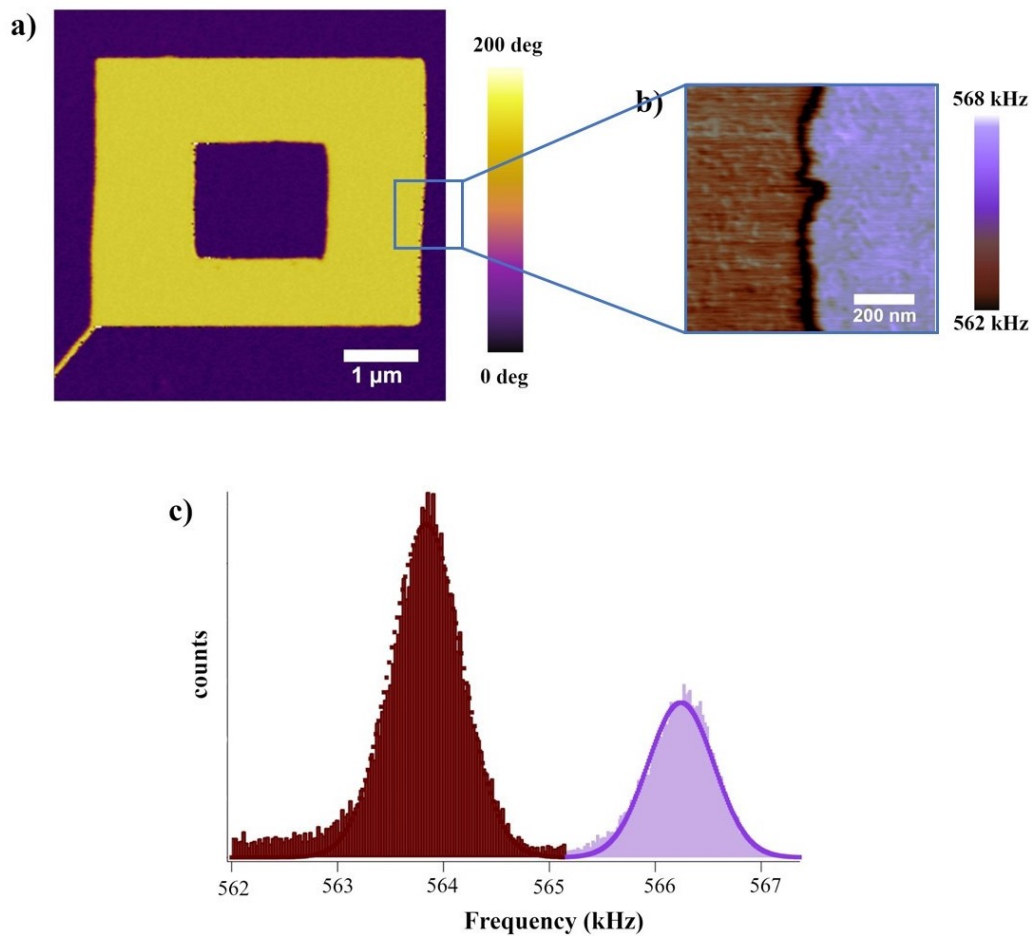


Figure 3.15: a) PFM phase image of PbTiO_3 thin film of 20 nm thickness grown on SrTiO_3 substrate. Yellow areas correspond to domains with polarization pointing up and purple areas to domains pointing down. PFM measurements were performed with a soft tip (PPP-EFM Nanosensors; Schaffhausen, Switzerland), with cantilever stiffness ~ 2 N/m, applied force of 50 nN and ac excitation voltage of 1 V. b) The corresponding CR-AFM image of a zoomed in area, where it is demonstrated that domains polarized up correspond to lower values of resonance frequency and consequently are softer. The mechanical characterization of the sample (CR-AFM) was performed with a stiffer tip (PPP-NCLR Nanosensors; Schaffhausen, Switzerland). The cantilever had Al coating only on its reflecting side and the stiffness was ~ 45 N/m. c) Histograms of CR-AFM image. The shift in resonance frequency between up and down-polarized domains is calculated, through the histograms, up to 2.4 kHz.

On the other hand, **Figure 3.15** illustrates the same type of measurements for a thinner PbTiO_3 film with a thickness of 20 nm. In a similar way, two squares with opposite polarization

as shown in **Figure 3.15.a** were poled by ferroelectric lithography after the application of a $V_{dc} = \pm 5$ V to the tip. CR-AFM measurement of a part of this area is presented in **Figure 3.15.b**. Down-polarized domains demonstrate consistently stiffer mechanical response than up-polarized domains, as they are correlated with higher resonance frequency values. The mean shift between opposite domains is again calculated through histograms, as shown in **Figure 3.15.c** and rises up to 2,4 kHz. This enhanced shift between opposite domains, under the same mechanical load, in the case of the thinner sample, confirms the presence of a size dependence of the flexoelectric induced asymmetry in the mechanical stiffness.

Besides the observed contrast in the contact resonance frequency of opposite domains, there is another key aspect that arises immediately from a first analysis of images: the domain walls separating the opposite polarization also appear to have different mechanical properties than the domains around them. In this case, it is worth to note that domain walls are mainly evident in the thinner film due to different resolution of the images. This phenomenon is discussed into detail in the next chapter and is not correlated with the coupling of flexoelectricity and piezoelectricity.

The experiments above on thin films of PbTiO_3 of different thicknesses, with the same expected order of magnitude of induced flexoelectricity, confirm that the asymmetry in mechanical stiffness of ferroelectric domains shows a remarkable size dependence. In this regard, Abdollahi et al. [4] have simulated the cracking behavior of BaTiO_3 thin films over a sample size reduction down to the nanoscale, stating that the asymmetry induced by flexoelectricity is a size-dependent property. They observed that, when flexoelectricity is introduced, the energy release decreases with the beam thickness. Decrease of film thickness from one hundred nanometers to few tens of nanometers can lead to an enhancement of the asymmetry factor of almost 80% in fracture toughness between up and down-polarized domains. They have demonstrated that BaTiO_3 thin films with the right thickness and a given polarity, would be twice easy to crack than in an opposite direction. This behavior arises from the fact that as the sample thickness decreases, the relative volume of the flexoelectrically polarized region around the tip increases. Following this argument, one can claim that the same mechanism can affect other mechanical properties, such as stiffness.

Although a numerical simulation of this mechanism is out of the scope of this thesis, the phenomenon can be regarded qualitatively using same considerations as in ref. [4]: the en-

hanced contrast can be explained by the comparison of the relative volumes impacted by strain (piezoelectricity) and strain gradients (flexoelectricity) within the ferroelectric volume. It is known that the consequences of flexoelectric effects are enhanced with size reduction [44–46] and for thin enough samples, they can even induce full ferroelectric switching [7]. In thinner materials, the relative volume fraction of the flexoelectrically polarized region by the tip increases and thus, becomes more relevant or even dominate over the piezoelectric polarization of the film, potentially being able to cause switching when both are antiparallel. Conversely, when piezoelectricity and flexoelectricity align parallel, the flexoelectric polarization can even double the total polarization. This enormous flexoelectric induced polar contrast of thin films is thus translated into an enhanced mechanical contrast and the amount of asymmetry, as observed for all the samples measured in this thesis.

References

- [1] K. Cordero-Edwards, N. Domingo, A. Abdollahi, J. Sort, G. Catalan. *Ferroelectrics as Smart Mechanical Materials*, Adv. Mater. (2017).
- [2] C.R. Robinson, K.W. White, P. Sharma. *Elucidating the mechanism for indentation size-effect in dielectrics*, Appl. Phys. Lett. 101(12) (2012).
- [3] M. Gharbi, Z.H. Sun, P. Sharma, K. White. *The origins of electromechanical indentation size effect in ferroelectrics*, Appl. Phys. Lett. 95(14) (2009).
- [4] A. Abdollahi, C. Peco, D. Millán, M. Arroyo, G. Catalan, I. Arias. *Fracture toughening and toughness asymmetry induced by flexoelectricity*, Phys. Rev. B - Condens. Matter Mater. Phys. 92(9) (2015).
- [5] J. Ocenasek, H. Lu, C.W. Bark, C.B. Eom, J. Alcala, G. Catalan, A. Gruverman. *Nanomechanics of flexoelectric switching*, Phys. Rev. B 92(3) (2015).
- [6] N. Domingo, L. Lopez-Mir, M. Paradinas, V. Holy, J. Zelezny, D. Yi, S.J. Suresha, J. Liu, C. Rayan Serrao, R. Ramesh, C. Ocal, X. Marti, G. Catalan. *Giant reversible nanoscale piezoresistance at room temperature in Sr₂IrO₄ thin films*, Nanoscale 7(8) (2015).
- [7] G. Lu, Bark, Esque de los Ojos, Alcala, Eom, Catalan. *Mechanical Writing of Ferroelectric Polarization*, Stress Int. J. Biol. Stress 59(April) (2012).
- [8] P. Sharma, S. Ryu, J.D. Burton, T.R. Paudel, C.W. Bark, Z. Huang, Ariando, E.Y. Tsybal, G. Catalan, C.B. Eom, A. Gruverman. *Mechanical tuning of LaAlO₃/SrTiO₃ interface conductivity*, Nano Lett. 15(5) (2015).
- [9] Y. Gu, Z. Hong, J. Britson, L.Q. Chen. *Nanoscale mechanical switching of ferroelectric polarization via flexoelectricity*, Appl. Phys. Lett. 106(2) (2015).
- [10] A.H.G. Vlooswijk, B. Noheda, G. Catalan, A. Janssens, B. Barcones, G. Rijnders, D.H.A. Blank, S. Venkatesan, B. Kooi, J.T.M. De Hosson. *Smallest 90° domains in epitaxial ferroelectric films*, Appl. Phys. Lett. 91(11) (2007).
- [11] D. Berlincourt, H. Jaffe. *Elastic and Piezoelectric Coefficients of Single-Crystal Barium*

Titanate, Phys. Rev. 111(1) (1958).

[12] U. Rabe, M. Kopycinska, S. Hirsekorn, J.M. Saldaña, G.A. Schneider, W. Arnold. *High-resolution characterization of piezoelectric ceramics by ultrasonic scanning force microscopy techniques*, J. Phys. D. Appl. Phys. 35(20) (2002).

[13] W. J, N. JB, Z. H, N. V, O. SB, L. B, V. D, V. V, S. DG, W. UV, S. NA, R. KM, W. M, R. R. *Epitaxial BiFeO₃ multiferroic thin film heterostructures*, Science 299(5613) (2003).

[14] R. R, S. NA. *Multiferroics: progress and prospects in thin films*, Nat. Mater. 6(1) (2007).

[15] D.G. Schlom, L.-Q. Chen, C.J. Fennie, V. Gopalan, D.A. Muller, X. Pan, R. Ramesh, R. Uecker. *Elastic strain engineering of ferroic oxides*, MRS Bull. 39(2) (2014).

[16] J. Wu, J. Wang. —textitBiFeO₃ thin films of (1 1 1)-orientation deposited on SrRuO₃ buffered Pt/TiO₂/SiO₂/Si(1 0 0) substrates, Acta Mater. 58(5) (2010).

[17] J. Li, J. Wang, M. Wuttig, R. Ramesh, N. Wang, B. Ruetter, A.P. Pyatakov, A.K. Zvezdin, D. Viehland. Dramatically enhanced polarization in (001), (101), and (111) BiFeO₃ thin films due to epitaxial-induced transitions, Appl. Phys. Lett. 84(25) (2004).

[18] J. Wang, J.B. Neaton, H. Zheng, V. Nagarajan, S.B. Ogale, B. Liu, D. Viehland, V. Vaithyanathan, D.G. Schlom, U. V. Waghmare, N.A. Spaldin, K.M. Rabe, M. Wuttig, R. Ramesh. *Epitaxial BiFeO₃ multiferroic thin film heterostructures*, Science 299(5613) (2003).

[19] J. Wu, J. Wang. *Orientation dependence of ferroelectric behavior of BiFeO₃ thin films*, J. Appl. Phys. 106(10) (2009).

[20] L.W. Martin, Y.H. Chu, R. Ramesh. *Advances in the growth and characterization of magnetic, ferroelectric, and multiferroic oxide thin films*, Mater. Sci. Eng. R Reports 68(4–6) (2010).

[21] G. Catalan, J.F. Scott. *Physics and Applications of Bismuth Ferrite*, Adv. Mater. 21(24) (2009).

[22] F. Kubel, H. Schmid. Structure of a ferroelectric and ferroelastic monodomain crystal of the

perovskite BiFeO₃, Acta Crystallogr. Sect. B 46(6) (1990).

[23] C. Michel, J.M. Moreau, G.D. Achenbach, R. Gerson, W.J. James. *The atomic structure of BiFeO₃*, Solid State Commun. 7(9) (1969).

[24] Y.H. Chu, L.W. Martin, M.B. Holcomb, R. Ramesh. *Controlling magnetism with multiferroics*, Mater. Today 10(10) (2007).

[25] Z. RJ, R. MD, Z. JX, H. AJ, H. Q, Y. CH, K. A, W. CH, M. A, A. C, S. G, C. YH, I. JF, E. R, E. C, G. V, C. LQ, S. DG, S. NA, M. LW, R. R. *A strain-driven morphotropic phase boundary in BiFeO₃* Science 326(5955) (2009).

[26] I. IC, L. S, D. B, B. M, F. S, J. E, G. G, P. S, C. A, J. J, B. L, B. A, D. B. *Bridging multiferroic phase transitions by epitaxial strain in BiFeO₃*, Phys. Rev. Lett. 105(5) (2010).

[27] J.X. Zhang, Y.L. Li, S. Choudhury, L.Q. Chen, Y.H. Chu, F. Zavaliche, M.P. Cruz, R. Ramesh, Q.X. Jia. *Computer simulation of ferroelectric domain structures in epitaxial BiFeO₃ thin films*, J. Appl. Phys. 103(9) (2008).

[28] J.C. Yang, Q. He, S.J. Suresha, C.Y. Kuo, C.Y. Peng, R.C. Haislmaier, M.A. Motyka, G. Sheng, C. Adamo, H.J. Lin, Z. Hu, L. Chang, L.H. Tjeng, E. Arenholz, N.J. Podraza, M. Bernhagen, R. Uecker, D.G. Schlom, V. Gopalan, L.Q. Chen, C.T. Chen, R. Ramesh, Y.H. Chu. *Orthorhombic BiFeO₃*, Phys. Rev. Lett. 109(24) (2012).

[29] I. Gross, W. Akhtar, V. Garcia, L.J. Martínez, S. Chouaieb, K. Garcia, C. Carrétéro, A. Barthélémy, P. Appel, P. Maletinsky, J.-V. Kim, J.Y. Chauleau, N. Jaouen, M. Viret, M. Bibes, S. Fusil, V. Jacques. *Real-space imaging of non-collinear antiferromagnetic order with a single-spin magnetometer*, Nat. 2017 5497671 549(7671) (2017).

[30] D.A. Scrymgeour, V. Gopalan. *Nanoscale piezoelectric response across a single antiparallel ferroelectric domain wall*, Phys. Rev. B 72(2) (2005).

[31] R. Proksch. *In-situ piezoresponse force microscopy cantilever mode shape profiling*, J. Appl. Phys. 118(7) (2015).

[32] P.T. Tue, Y. Takamura. *Lead Zirconium Titanate Films and Devices Made by a Low-*

Temperature Solution-Based Process, IntechOpen, 2018.

[33] J.S. Wright, L.F. Francis. Phase development in Si modified sol-gel-derived lead titanate, *J. Mater. Res.* 8(7) (1993).

[34] G. Burns, B.A. Scott. *Lattice Modes in Ferroelectric Perovskites: PbTiO₃ class*, *Phys. Rev. B* 7(7) (1973).

[35] K. Nishida, G. Matuoka, M. Osada, M. Kakihana, T. Katoda. *Effects of the substrate on properties of PTO thin film*, *Appl. Surf. Sci.* 216(1–4) (2003).

[36] E. Langenberg, D. Saha, M.E. Holtz, J.J. Wang, D. Bugallo, E. Ferreira-Vila, H. Paik, I. Hanke, S. Ganschow, D.A. Muller, L.Q. Chen, G. Catalan, N. Domingo, J. Malen, D.G. Schlom, F. Rivadulla. *Ferroelectric Domain Walls in PbTiO₃ Are Effective Regulators of Heat Flow at Room Temperature*, *Nano Lett.* (2019).

[37] J.P. Killgore, R.H. Geiss, D.C. Hurley. In-Situ Measurement of Atomic Force Microscope Tip Wear by Contact Resonance Force Microscopy (2011).

[38] K.-H. Chung. *Wear characteristics of atomic force microscopy tips: A review*, *Int. J. Precis. Eng. Manuf.* 2014 1510 15(10) (2014).

[39] Y. Xu. *Ferroelectric Materials and Their Applications* - 1st Edition, North Holland, 1991.

[40] S.-R. Jian, H.-W. Chang, Y.-C. Tseng, P.-H. Chen, J.-Y. Juang. *Structural and nanomechanical properties of BiFeO₃ thin films deposited by radio frequency magnetron sputtering*, *Nanoscale Res. Lett.* 8(1) (2013).

[41] A.K. Tagantsev. *Electromechanical Phenomena: Flexoelectric Effect*, *Encycl. Mater. Sci. Technol.* (2011).

[42] P. V Yudin, A.K. Tagantsev. *Fundamentals of flexoelectricity in solids*, *Nanotechnology* 24(43) (2013).

[43] Q. Li, C.T. Nelson, S.-L. Hsu, A.R. Damodaran, L.-L. Li, A.K. Yadav, M. Mccarter, L.W. Martin, R. Ramesh, S. V Kalinin. Quantification of flexoelectricity in PbTiO₃/SrTiO₃ superlattice polar vortices using machine learning and phase-field modeling, *Nat. Commun.*

8(1468) (2017).

[44] D. Lee, A. Yoon, S.Y. Jang, J.G. Yoon, J.S. Chung, M. Kim, J.F. Scott, T.W. Noh. *Giant flexoelectric effect in ferroelectric epitaxial thin films*, Phys. Rev. Lett. 107(5) (2011).

[45] Y. Qiu, H. Wu, J. Wang, J. Lou, Z. Zhang, A. Liu, G. Chai. *The enhanced piezoelectricity in compositionally graded ferroelectric thin films under electric field: A role of flexoelectric effect*, J. Appl. Phys 123 (2018).

[46] B.C. Jeon, D. Lee, M.H. Lee, S.M. Yang, S.C. Chae, T.K. Song, S.D. Bu, J.S. Chung, J.G. Yoon, T.W. Noh. *Flexoelectric effect in the reversal of self-polarization and associated changes in the electronic functional properties of bifeo₃ thin films*, Adv. Mater. 25(39) (2013).

CHAPTER 4

Mechanical Properties of Ferroelectric Domain Walls

Ferroelectric domain walls separate domains with homogeneous ferroelectric polarization. One of its most unique characteristics resides in the fact that they possess different functional properties from those of the domains around them. Additionally, domain walls have a thickness of few unit cells and can be manipulated as and when required by the application of an external electric field. Despite the intensive study of their singular electronic features, very little is known about the mechanical properties of ferroelectric domain walls.

In this chapter, I present an extensive study of the mechanical properties of 180° ferroelectric domain walls with out-of-plane polarization. The nanomechanical properties of the domain walls have been measured by Contact Resonance Atomic Force Microscopy (CR-AFM). I have studied different ferroelectric materials with various morphologies and, in all cases, domain walls demonstrate distinct -softer- mechanical response from the domains they separate. After proving that the softening of ferroelectric domain walls with respect to the neighborhood ferroelectric domains is ubiquitous, I present the quantification of domain walls' stiffness. Finally, a theoretical framework to explain the domain wall mechanical behavior is presented, which supports the view that this effect is common to all ferroelectrics.

4.1 Ferroelectric domain walls

An important appeal of ferroelectric domain walls, besides their nanoscopic size and the fact that can be created, moved, or erased “on demand” with the application of an external field, resides in the contrast between their functional properties and those of the domains. For example, domain walls of classical ferroelectric dielectrics such as $\text{Pb}(\text{Zr}_{0,2}\text{Ti}_{0,8})\text{O}_3$ [1], LiNbO_3 [2] and BaTiO_3 , display higher electrical conductance than the bulk. This also applies to multiferroics such as YMnO_3 [3] or $\text{Cu}_3\text{B}_7\text{O}_{13}\text{Cl}$ [4], and in the case of the room temperature multiferroic BiFeO_3 , it was shown to display not only conductivity but also magnetoresistance at some of its characteristic domain walls [5–8], despite being an insulator (wide bandgap semiconductor). Beyond ferroelectrics, distinctive functional properties of domain walls have also been observed in ferromagnets, antiferromagnets or ferroelastic materials, in which for instance, it has been shown that ferroelastic domain walls of semiconductor WO_{3-x} are indeed superconducting [9]. My research focuses on mechanical response of ferroelectric domain walls.

4.2 Experiments on domain wall elasticity

In **Chapter 3**, the mechanical properties of out-of-plane-polarized ferroelectric domains were investigated by contact resonance microscopy techniques. In this chapter, CR-AFM is used to demonstrate the ubiquitous differential nanomechanical response of domain walls in different types of ferroelectrics. As described in **Chapter 2**, CR-AFM mode is used to obtain information about the mechanical properties of the material. Specifically, resonance frequency is directly proportional to the stiffness of the material; higher resonance frequency corresponds to stiffer material. Here I concentrate on a single topology of domain wall, and thus only 180° ferroelectric domain walls will be examined. The analysis of the results obtained in the frame of this chapter can also be applied to most of the images shown in **Chapter 3**, where domain and domain walls were imaged simultaneously. In order to establish the universality of this phenomenon, multiple ferroelectric materials were investigated, with different morphologies, from single crystals to thin films. The experimental protocol followed is the same as in case of ferroelectric domains: initially PFM mode is used to image the ferroelectric distribution of domains and domain walls on the surface of the material and afterwards, CR-AFM imaging is used to probe the mechanical

properties of domain walls.

4.2.1 180° Domain Walls of LiNbO₃ single crystal

Lithium niobate (LiNbO₃) is a classic ferroelectric with rhombohedral crystallographic structure [10,11]. The non-centrosymmetric structure allows the displacement of positive charges (Li⁺ and Nb⁵⁺) with respect to oxygen atom positions [12]. Below the Curie temperature of $T_c \sim 1210$ °C, LiNbO₃ exhibits a hexagonal structure with polarization restricted along the c-axis (uniaxial ferroelectric). Hexagonal structures favor the formation of 180° domain walls along well-defined orientations in the plane of the crystal, with a relative angle of 60°. This ferroelectric material has excellent piezoelectric, electrooptic and nonlinear optic properties [13]. It is one of the most widely used electrooptic materials [14], and its application has expanded to optoelectronic photovoltaic tweezers [15,16]. The periodically poled LiNbO₃ (PPLN) single crystal studied here is a domain-engineered LiNbO₃ single crystal with bulk antiparallel ferroelectric domains. Due to its trigonal crystal structure [10,17], the ferroelectric domains of PPLN point alternatively to $+c$ and $-c$ direction. PPLN is a common sample used in many laboratories as reference for PFM microscopy: in this case, the sample was provided by Asylum Research company and shows a characteristic pattern of ~ 5 μm oppositely-polarized up and down domains. Full electromechanical characterization of PPLN was achieved using DART PFM and is presented in

Figure 4.1.

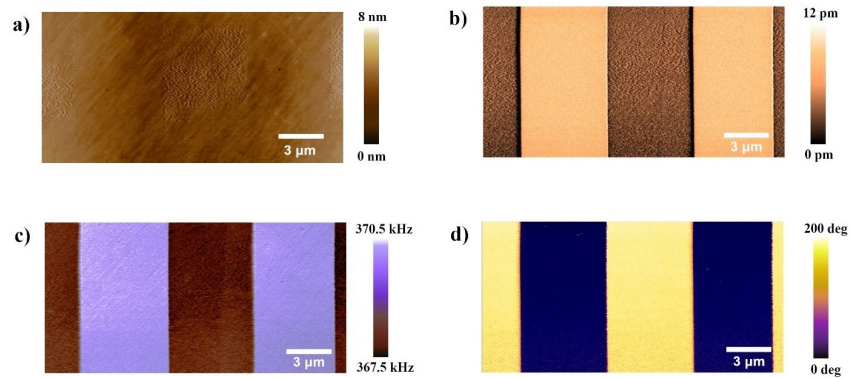


Figure 4.1: a) Topography in contact mode of PPLN in a scan area of 17×8.5 μm . b) PFM amplitude of the same area. c) DART PFM contact resonance frequency and d) the corresponding PFM phase. The crystal is periodically polarized out-of-plane with yellow and purple colour corresponding to domains pointing up and down respectively. The measurement was performed with a soft cantilever with stiffness ~ 3 N/m with PtIr coating (PPP-EFM Nanosensors; Schaffhausen, Switzerland). The ac voltage applied for the excitation of the sample was 3 V while the applied force was ~ 1 μN .

Figure 4.1.a shows the topography of the sample in contact mode. The surface of the sample is smooth with a roughness of 1.2 nm. **Figure 4.1.b** shows the PFM amplitude of the same area, where oppositely-polarized domains appear slightly unequal. This behavior is not an ideal PFM amplitude response, as amplitude should depend only on the magnitude of polarization and not its direction and consequently, one should expect the same amplitude for both domains. This difference in PFM amplitude of oppositely-polarized domains for PPLN samples is pretty common and known to appear due to different reasons, being the most relevant measurement artefacts arising from the long-range electrostatic interactions between the body of the cantilever and the polarization or the laser position on the cantilever during the measurement on resonance [18], as discussed in **Section 3.3**. **Figure 4.1.c** shows the PFM contact resonance while **Figure 4.1.d** shows the PFM phase of the same area, with domains of opposite polarization having a phase difference of 180° . The behavior of PFM contact resonance frequency will be discussed in the next chapter.

The mechanical properties of domains walls were mapped by CR-AFM, where changes in contact resonance frequency are related with changes on the sample stiffness. Details about the CR-AFM mode can be found in **Section 2.4**.

PFM was used to detect the 180° ferroelectric domain walls. In **Figure 4.2**, the PFM phase of PPLN (a) is compared to the CR-AFM image of the same area (b).

Besides the contrast in the contact resonance frequency between up and down domains arising from flexoelectric effects as discussed in **Chapter 3**, an additional more abrupt contrast is observed at the domain walls. At the position of 180° ferroelectric domain walls, distinctly lower values of contact resonance frequency are observed, decreasing up to 400 Hz with respect to the average of the domains, and thus exhibiting softer mechanical properties than the average of the neighborhood domains. In order to prove the correlation between the domain walls and the mechanical softness, cross sections of both PFM phase image and CR-AFM are presented in **Figure 4.2.c**; indeed, the shift from 0° to 180° in the PFM phase determining the presence of the domain wall overlap perfectly with the shift in contact resonance frequency of CR-AFM, confirming that the apparent softening arises from the domain walls of PPLN.

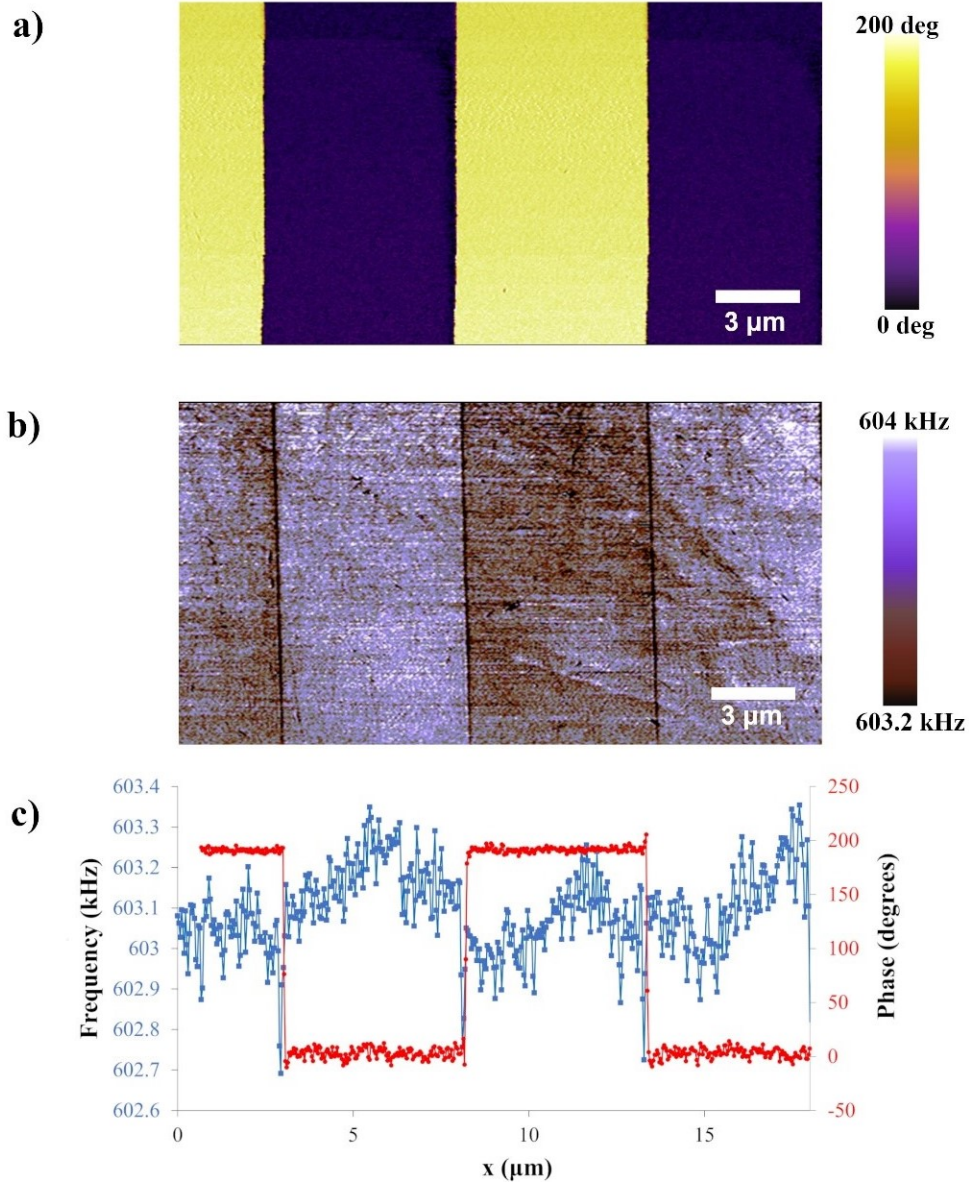


Figure 4.2: a) PFM phase image of periodically poled LiNbO_3 crystal. Ferroelectric domains are polarized out-of-plane pointing up (yellow colour) and pointing down (purple colour). b) The corresponding CR-AFM image. Shifts in frequency correspond to different mechanical properties of the material. It is shown that 180° ferroelectric domain walls that separate oppositely polarized domains appear to be mechanically softer than the domains. CR-AFM was measured using a stiff cantilever with $k \sim 45 \text{ N/m}$ and PtIr coating (PPP-NCLPt Nanosensors; Schaffhausen, Switzerland) and the applied force was $\sim 2.8 \text{ N}$. c) Cross sections of PFM phase and CR-AFM along the x-axis in the middle of the image.

Nevertheless, it has been demonstrated that 180° domain walls in LiNbO_3 single crystals can possess distinguished electrical properties and topological features due to a partial charging [19,20]. In order to discard second order and crossed topological effects on the mechanical properties of such domain walls, the study was expanded to other materials and geometries, with simpler crystallographic structures.

4.2.2 180° Domain Walls of PbTiO₃ thin films

Lead titanate can be easily grown on different type of substrates in the form of thin films. PbTiO₃ shows a tetragonal structure below Curie temperature, with the atoms distorted from their cubic arrangement by small relative displacements along the tetragonal *c* axis [21]. On the other hand, taking advantage of the thin films' morphology, it is possible to write and move domain walls with small electrical voltages at our wish with an AFM tip i.e., via local ferroelectric lithography. Finally, another advantage of thin films is that, with a suitable substrate that imposes compressive strain, it is possible to prevent the formation of in-plane domains so that the film behaves as a uniaxial ferroelectric with only out-of-plane polarization.

The sample under investigation is a PbTiO₃ thin film with thickness of 20 nm, epitaxially grown by reactive molecular beam epitaxy on a single-crystal SrTiO₃ substrate (the growth details can be found elsewhere [22]). Due to large compressive stress exerted by the substrate (-1.36%), only domains with polarization out-of-plane are allowed in the film [22]. Domains of opposite sign of polarization were created after the application of an external *dc* voltage of 5V through the tip. Full electromechanical characterization of PbTiO₃ thin film by DART PFM is reported in **Section 3.3.3**. **Figure 4.3.a** shows a PFM phase image of the film of 2x2 μm, with two ferroelectric domains oppositely-polarized. That means that the domain wall that separates them is an 180° pure ferroelectric domain wall. **Figure 4.3.b** shows the contact resonance frequency of the same area, as measured by CR-AFM. Apart from the shift in frequency between oppositely-polarized domains, which derives from the coupling of piezoelectricity and flexoelectricity, as discussed thoroughly in **Chapter 3**, again significant contrast to lower values of contact resonance frequency arises at the position of the domain wall. **Figure 4.3.c** shows the cross section of PFM phase and CR-AFM on PbTiO₃ thin film respectively, demonstrating that domain walls univocally lead to lower values of contact resonance frequency. Additionally, through section of CR-AFM measurement (**Figure 4.3.c**) it is calculated that in this case the contact resonance frequency of the domain wall is 2.2 kHz lower than the mean value of contact resonance frequency of domains.

As a side note, it is worth to mention that the significant difference in the contact resonance frequency between up and down polarized domains among the single crystal (PPLN) and the thin film (PbTiO₃) observed in **Figure 4.2.b** and **4.3.b** is another example of the size effect

observed for the asymmetry in mechanical properties of ferroelectrics as a function of polarization, extensively discussed in **Chapter 3**. Domain walls, in any case, are softer than both up and down-polarized domains.

Considering the tetragonal symmetry of the unit cell of PbTiO_3 , one way to visualize the transition from up to down domains through a 180° domain wall from the crystallographic point of view is by considering a shrink of the tetragonal unit cell along the c-axis (out-of-plane) to a cubic symmetry at the domain wall position, corresponding to a null ferroelectric polarization, and then back to tetragonal symmetry in opposite direction, as depicted in **Figure 4.3.d** [23]. While the elastic constants of ferroelectric PbTiO_3 is reported to be ~ 289 GPa [24], for the cubic paraelectric phase decrease to ~ 271 GPa [24]. In this sense, it could be expected that the lack of polarization inside the domain wall together with the local change of symmetry for this case lead to a slight softening of the material at this point.

In summary, CR-AFM experiments of PbTiO_3 thin films confirm that 180° ferroelectric domain walls of this tetragonal ferroelectric have also distinct mechanical properties than the surroundings domains in a completely different crystallographic structure than the previous case. This suggests a universality of the relative softness of ferroelectric domain walls, a general phenomenon that does not rely on the composition or sample morphology.

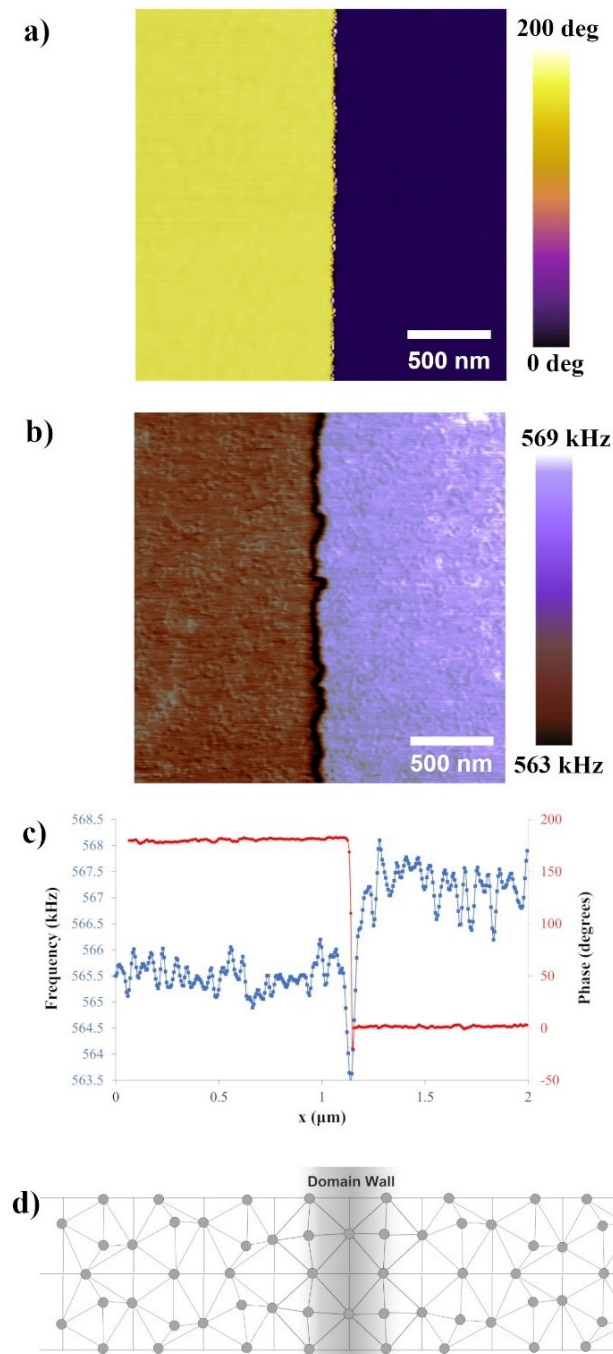


Figure 4.3: a) PFM phase image of a PbTiO_3 thin film on a SrTiO_3 substrate in a scan area of $2 \times 2 \text{ m}$. Domains with opposite out-of-plane polarization are denoted with yellow (up) and purple (down) colour respectively. The domain separating them is 180° ferroelectric domain wall. Measurements were performed with a conductive tip with PtIr coating and $k \sim 2 \text{ N/m}$ (PPP-EFM Nanosensors; Schaffhausen, Switzerland). The applied force was $\sim 60 \text{ nN}$ while the ac voltage applied to excite the sample was 1.5 V . b) CR-AFM image of the same area demonstrating differences in mechanical stiffness of the material. Oppositely polarized domains are mechanically distinct, as explained in previous chapter, but also, domain wall appear softer than both domains. The tip used had $k \sim 45 \text{ N/m}$ (PPP-NCL Nanosensors; Schaffhausen, Switzerland) and the applied force was $\sim 700 \text{ nN}$. c) Cross sections of PFM phase (a) and CR-AFM image (b). d) Sketch of unit cell transformation from tetragonal (domains) to cubic (domain wall) symmetry, taken by [23].

4.2.3 180° Domain Walls of BaTiO₃

In order to verify the generality of domain walls' softness, as suggested by LiNbO₃ and PbTiO₃, I expanded the study to BaTiO₃ ferroelectric single crystals. BaTiO₃ shows the same tetragonal structure [25] as PbTiO₃, but in our sample the polarization domains appeared spontaneously during the phase transition to the ferroelectric state. As described in **Section 3.3.1**, a BaTiO₃ (100) single crystal (CrysTec GmbH) is submitted to the paraelectric-ferroelectric transition in ambient atmosphere that leads to a distribution straight of a/c domains observable by PFM as shown in **Figure 3.3** and **3.4.**, as well as bubble-like c-domains. The coexistence of a/c domains makes BaTiO₃ single crystal the ideal sample for quantification of the experimental results as the known elastic constants of a domains can be used for calibration (this method is described in **Appendix A**) and thus allows the quantification of domain walls' stiffness, as it will be presented later on.

Figure 4.4.a shows the PFM phase of BaTiO₃ crystal over an area of 4x4 μm, where oppositely polarized out-of-plane domains are denoted with yellow (up) and purple (down). The diagonal stripes correspond to in-plane polarized domains, as described on the previous chapter. CR-AFM measurements (**Figure 4.4.b** and **Figure 4.4.c**) display that 180° ferroelectric domain walls show lower values of the contact resonance frequency and thus they are softer than the surrounding domains. Cross section of CR-AFM image (along green line) was used to calculate the exact shift in contact resonance frequency of domain walls compared with the average value of domains, as displayed in **Figure 4.4.c**. From the section it is calculated that the shift in contact resonance frequency between domains and domain walls is $\Delta f = 2.17$ kHz. It is worth mentioning that the contrast between up and down domains, as predicted from the analysis in **Chapter 3**, is not particularly apparent. This is due to the fact that this image includes ferroelastic a-domains, which have a much higher elastic constant than c-domains, and the colour scale was adjusted to optimize the wider range of frequencies associated with the strong a/c contrast, which is much stronger than the c+/c- contrast.

Concluding, 180° ferroelectric domain walls of LiNbO₃ single crystal, PbTiO₃ thin film and BaTiO₃ single crystal appear to be recurrently softer than the domain walls they separate, despite the diversity in their chemical composition and their morphology. Moreover, the softening doesn't seem to depend on the shape of the 180° ferroelectric domain walls, since similar behaviour is

observed for all, linear, crepted, and curved domain walls. Altogether, it provides clear evidence that the phenomenon can be universal.

It is also worth mentioning that the observed softening of domain walls is qualitatively similar, irrespectively of the way in which domain walls were created; the mechanical properties change in the same direction for spontaneously created (as in BaTiO_3 single crystals) and electrically written 180° domain walls, as in case of PbTiO_3 thin films or LiNbO_3 single crystals. Moreover, in contrast with the phenomena discussed in Chapter 3, this softening doesn't seem to be size dependent, since the apparent shift of the contact resonance frequency is of the same order of magnitude for thin films and single crystals.

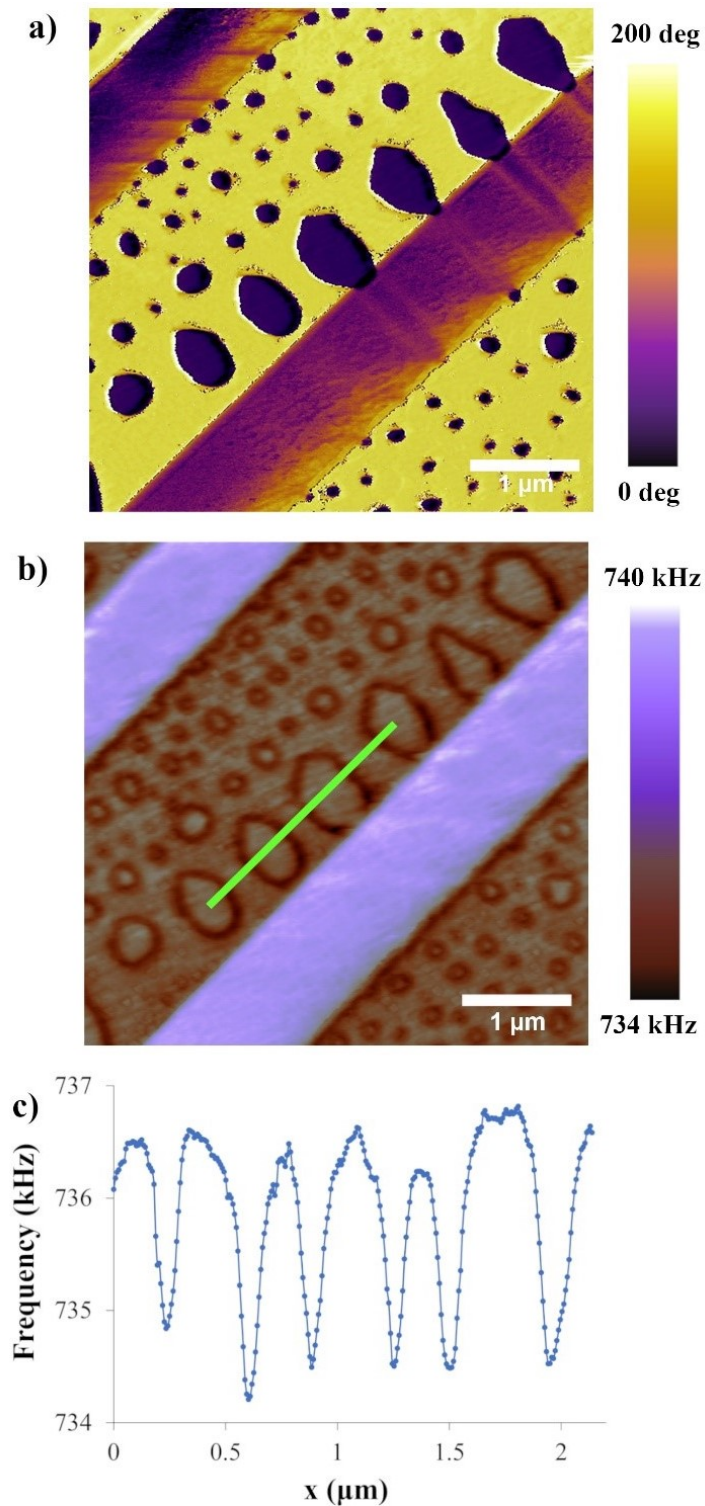


Figure 4.4: a) PFM phase image of BaTiO₃ single crystal over an area of 4x4 μm. Up and down c domains are shown with yellow and purple colour respectively, while diagonal stripes correspond to domains with in-plane polarization. b) CR-AFM measurement of a scan area 4x4 μm, where domain walls appear to correspond to lower values of contact resonance frequency and thus softer mechanical properties. Both measurements were performed with a tip with no coating and $k \sim 45$ N/m (PPP-NCL Nanosensors; Schaffhausen, Switzerland), while the applied force was ~ 700 nN. c) Cross section of CR-AFM image (b) along the green line, showing the changes in contact resonance frequency.

4.3 Quantification of domain wall elasticity

The previous sections show the qualitative study of the mechanical softening of 180° ferroelectric domain walls. The next step is to delve into the quantification of the experimental results. In order to quantify the softening, shifts in contact resonance frequency, as probed by CR-AFM, need to be translated into changes in stiffness, and particularly, into changes in the elastic modulus of the material.

The way to achieve it is to represent the system of the tip in contact with the sample as a system of springs in series. The methodology is described in detail in **Appendix A**. Briefly, the cantilever is represented as an elastic beam with spring constant k_{lever} , and the tip-surface contact as a spring with elastic constant k^* , which depends on both the stiffness of the tip (k_{tip}) and the stiffness of the sample (k_s) (**Figure 4.5**). The contact can be described from a mechanical point of view as an Hertzian contact model [26,27] and also acts as two springs in series, the tip and the sample respectively.

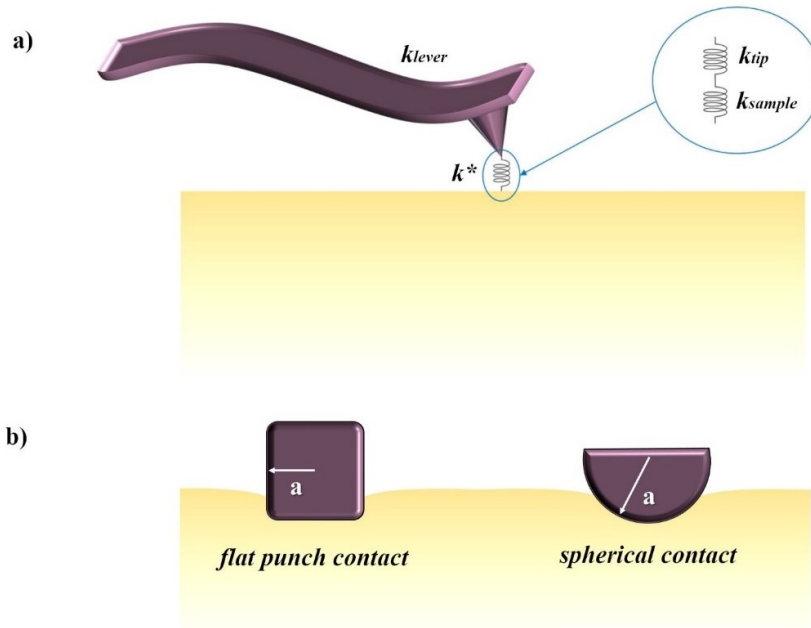


Figure 4.5: a) Schematic representation of the cantilever in contact with the sample. b) Diagram of the tip – sample contact based on the Hertzian model, demonstrating both flat punch contact and spherical contact.

The elastic constants of the system are represented not by Young's modulus but by effective Young's modulus, which correlates the elastic constants of the sample and the tip following

Equation 4.1 [28]:

$$\frac{1}{E_s^*} = \frac{1 - \nu_s^2}{E_s} + \frac{1 - \nu_{tip}^2}{E_{tip}} \quad (4.1)$$

where E_s and E_{tip} is the Young's modulus of the sample and the tip, and ν_s and ν_{tip} is Poisson ratio respectively, for sample and tip. The effective Young's modulus is correlated with the contact stiffness k^* as:

$$E_i^* = \frac{k_i^*}{2a_c} = Ck_i^{*m} \quad (4.2)$$

where a_c is the contact radius of the tip with the sample and m is a factor that depends on the tip shape. If we consider the tip as a sphere in contact with a flat surface, then the contact area between the tip and the sample will depend on the applied force. Note that the applied force can be considered constant during the measurement of one image since a feedback loop activated throughout the scan controls it. In this case, for the tip-spherical approach, $m = 3/2$. On the other hand, when the tip is described as a flat punch, the tip contact radius a_c will be independent of the applied force and will be constant, in which case $m = 1$.

To determine the Young's modulus of the material (E_s), the Young's modulus of the tip (E_{tip}) must be known and the effective Young's modulus (E_s^*) must be calculated from the effective contact stiffness k_s^* and the contact radius a . But if we have a reference sample to compare the measurements with, then we can circumvent the use of the contact radius by applying the following approach:

$$\frac{E_{dw}^*}{E_s^*} = \frac{Ck_{dw}^{*m}}{Ck_s^{*m}} = \left(\frac{k_{dw}^*}{k_s^*} \right)^m \quad (4.3)$$

where sub index dw stands for domain walls and s for a reference known sample. Here I use as reference the average response of c domains to compare the relative decrease of Young's modulus between domain walls and their surrounding domains. In this approach, the only unknown variable is m which depends on tip geometry. Then, from here, and knowing the relative change between the Young's modulus of the tip and the sample, one can calculate the relative change of the Young's modulus at domain walls using the following equation:

$$\frac{E_{dw}}{E_s} = \frac{\frac{E_{dw}^* E_{tip}}{E_s^* E_s} (1 - \nu_{dw}^2)}{\frac{E_{tip}}{E_s} (1 - \nu_s^2) + \left[1 - \frac{E_{dw}^*}{E_s^*} \right] (1 - \nu_{tip}^2)} \quad (4.4)$$

The tip sample contact stiffness k_i^* for the different areas can be calculated using the models settled by Rabe [29] and developed by Hurley and Killgore [30] where k^* is correlated with the experimental values of resonance frequency, as measured by CR-AFM. A detailed description of the method can be found at **Appendix A**. To do so, the cantilever's motion simplified as an elastic beam, is described by a wave equation. The geometrical characteristics of the cantilever, as well as the experimental values of resonance frequencies, both the free resonance frequency (f_1^0) and resonance frequency in contact (f_1), are used to calculate the wavenumber which describes cantilever's motion. Then, the effective contact stiffness k^* , for each value of experimentally measured resonance frequency in contact (f_1), is calculated. The magnitudes of the geometrical characteristics of the cantilever are presented in **Table 4.1**.

E_{lever} (GPa)	b (μm)	w (μm)	Density (kg/m^3)	L (μm)	γ	L_1 (μm)	Tip height (μm)	k_{lever} (N/m)	f_1^0 (kHz)	Tilting angle ($^\circ$)
160	5.34	59	2238	237	0.951	225	13.4	31.53	158	11

Table 4.1: Geometrical characteristics of the cantilever. The cantilever is modelled as a beam with length L , thickness b , density ρ and Young's modulus E_{lever} . The tip is located in distance L_1 from the clamped end of the cantilever, while k_{lever} is the spring constant of the cantilever and f_1^0 the free resonance frequency. The geometrical characteristics of the cantilever were either provided by the manufacturer either measured experimentally by SEM.

The values for the measured contact resonance f_1 and calculated k^*/k_{lever} are shown in **Table 4.2**. Using this elastic constant for c domains [31] in **Equation 4.1**, the effective Young's modulus of the tip is being calculated. Then, the equation is solved again, but this time, the Young's modulus of domain wall is unknown. The results are presented in **Table 4.2**, as well as the calculated values for contact stiffness k^* and effective Young's modulus E^* both for c domains and domain walls.

Considering the calculated values shown above, the measured Young's modulus of domain walls (E_{dw}) appears to be reduced by 7% with respect to that of the c domains in the spherical tip-sample contact approach, meaning that 180° domain walls in BaTiO_3 single crystal are 7% softer than the domains along the c -direction.

	f_1 (kHz)	k^*/k_{lever}	E_{dw}/E_s ($m = 1$)	E_{dw}/E_s ($m = 1.5$)
c domains	736.57	82.57	95.27%	93%
domain walls	734.4	69.93	95.27%	93%

Table 4.2: Experimentally measured contact resonance frequency f_1 on the c domains (average values) and the 180° domain walls separating those on a $BaTiO_3$. The obtained values for the effective contact stiffness k^* using the model described in Chapter 2 for both cases using the parameters of Table 4.1 are shown in the second column. These values are used to calculate the percentage of change of the Young modulus at the domain walls using Equation 4.4, with $t_{ip} = 0.23$, $s =_{dw} = 0.3$, and $E_c = 164.9$ GPa.

4.4 The origin of domain wall softening

After having determined that 180° ferroelectric domain walls are always mechanically softer than the domains around them, despite being ferroelectric and not ferroelastic, the origin of this softening is being examined. The theoretical approach of domain walls' softening was performed by two research groups: group of Quantum Materials Theory of Italian Institute of Technology (IIT) led by Sergey Artyukhin and group of Professor Massimiliano Stengel in the department of Materials Simulation and Theory at the Institute of Materials Science of Barcelona (ICMAB). The obtained results point to at least a couple of intrinsic mechanisms that might be responsible for the distinct mechanical properties of domain walls which will be discussed in detail in **Section 4.4.2** and **4.4.3**.

4.4.1 Domain wall softening due to different factors

Before the discussion of theoretical approaches, it is important to rule out possible effects that may cause domain walls softening. The intrinsic mechanical properties of the domain walls may arise from different origins. To begin with, it has been proposed that ferroelectric domain walls can be non-Ising-type and thus, an in-plane component of polarization exists in domain walls [32–35]. Although there is no experimental evidence of in-plane polarization in 180° ferroelectric domain walls of $BaTiO_3$ single crystal, and despite the fact that even in case of in-plane component, the overall behaviour of domain wall is Ising-like [36], the possibility of a mechanical contribution coming from in-plane polarization at the walls is excluded because in-plane polarization should in fact lead to stiffer, not softer, response. An experimental proof of this can be taken from the in-plane domains in **Figure 4.3**: a domains correspond to higher contact resonance frequencies

and thus are stiffer, in agreement with reported macroscopic measurements [37].

In **Chapter 3** is presented the distinct mechanical response of out-of-plane polarized ferroelectric domains and the polarity-dependence of this phenomenon. In case of ferroelectric domains under deformation the energy cost has two components: the elastic one ($k\varepsilon^2/2$) and the electrostatic one ($P^2/2\chi$). In domain walls the total polarization equals to zero. Consequently, the electrostatic terms disappears and the energy cost of deformation for domain walls depends only on the elastic constants of the material, meaning that domain walls softening is not a polarity-dependent phenomenon.

Another possibility, softening due to local switching effects, can also be ruled out. Albeit it is known that a mechanical load, as the one applied by the AFM tip in contact, can cause flexoelectric assisted switching of the ferroelectric polarization [38], and it is also expected that the coercive field of the ferroelectric should be smaller near the ferroelectric wall [39], no displacement of domain walls over scanning has been observed. Yet, even after multiple scans over the same area, with the maximum mechanical load of 20 μN , no shift was detected in the position of the domain walls. Nevertheless, this does not exclude the possibility of an elastic reversible deflection of the wall towards the tip.

Finally, we need to rule out whether the effect might be due to material's defects, known to be attracted to domain walls [40]. Defects are sample-dependent and the most common ones, such as oxygen vacancies, are difficult to quantify. However, softening caused by material's defects should have the same effect all over the material. That means that 180° domain walls both in a and c-domains should demonstrate the same softness. To examine this possibility, both types of domain walls were mechanically characterized. BaTiO_3 single crystal is an ideal sample to test this hypothesis, because both 180° domain walls of a-domains (in-plane polarization) and 180° domain walls of c domains (out-of-plane polarization) can be found in the same scan area. An advantage of having all the possible directions of polarization and domain walls on a single scan is that the exactly the same values of experimental parameters are ensured and changes in nanomechanical responses may result only from changes in the mechanical properties of the material.

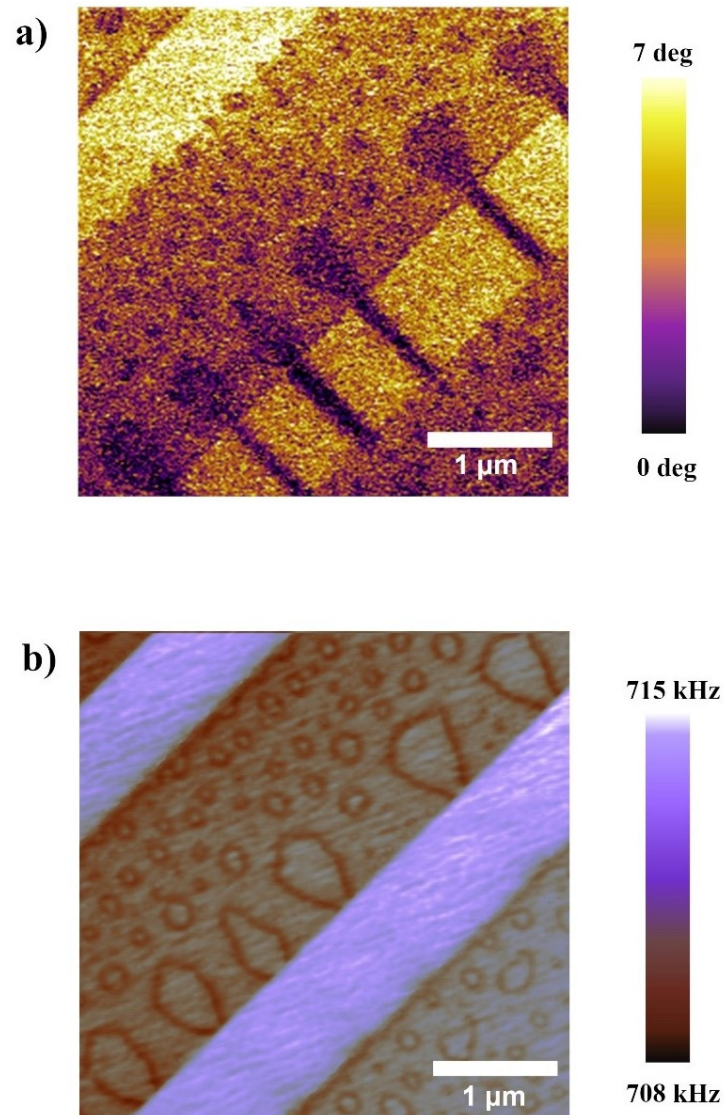


Figure 4.6: a) Lateral PFM phase of BaTiO_3 single crystal where in-plane polarization of the crystal is being probed. b) Corresponding CR-AFM image where 180° ferroelectric domain walls appear softer when the polarization is out-of-plane, but the mechanical contrast disappears in case of in-plane polarized areas. All measurements were performed with a stiff cantilever with no coating and stiffness of $\sim 45 \text{ N/m}$ (PPP-NCL Nanosensors; Schaffhausen, Switzerland), while the applied force was $\sim 700 \text{ nN}$.

Figure 4.6.a corresponds to a lateral PFM phase image of BaTiO_3 single crystal, where in-plane polarization is being probed. In this figure, it is clearly shown how the polarization is being distributed inside the diagonal stripe. Finally **Figure 4.6.b** is the CR-AFM measurement of the whole area, where differences in mechanical properties of the material are proportional to the shift in resonance frequency. While for out-of-plane domains, the 180° walls are softer, when the domains penetrate the in-plane polarized area, the mechanical contrast of the 180° walls disappears. The disappearance of mechanical contrast when the polarization is in-plane,

combined with the fact that we observe the softening of out-of-plane walls in materials with different chemistries, leads to the conclusion that the role of chemical defects is probably less important than intrinsic factors linked to the direction of the polarization. In what follows, I present two physical models, as proposed by our collaborating groups, that provide an intrinsic link between the mechanical softening and the polarization of the domains –and the absence of polarization in the domain walls: (i) dynamic softening due to reversible shift of domain wall, and (ii) reduced depolarization energy on the domain wall, due to absence of piezoelectricity.

4.4.2 Dynamic model for domain wall softening

The first theoretical approach for domain walls softening was performed by the group of Sergey Artyukhin. The behaviour of a ferroelectric material under the tip pressure was studied by describing the energy of the system by the appropriate model of first-principles calculations for BaTiO₃. [41,42]. Free energy density of the system can be described by the Ginzburg-Landau-Devonshire model:

$$f = f_l + f_g + f_q + f_c + f_f + f_{electr} \quad (4.5)$$

$$f_l = a_{ij}P_iP_j + a_{ijkl}P_iP_jP_kP_l + a_{ijklmn}P_iP_jP_kP_lP_mP_n \quad (4.6)$$

$$f_g = G_{ijkl}\nabla_iP_j\nabla_kP_l/2 \quad (4.7)$$

$$f_q = -q_{ijkl}P_iP_j\varepsilon_{kl} \quad (4.8)$$

$$f_c = C_{ijkl}\varepsilon_{ij}\varepsilon_{kl}/2 \quad (4.9)$$

$$f_f = \frac{\Gamma_{ijkl}}{2}(\nabla_iP_j\varepsilon_{kl} - P_i\nabla_j\varepsilon_{kl}) \quad (4.10)$$

$$f_{electr} = \varepsilon_r E^2/2 \quad (4.11)$$

where f_l is the Landau free energy density for uniform ferroelectric polarization P , f_g describes energy penalty for spatial variations of P , f_q describes the interaction between the polarization and strains ϵ_{ij} (electrostriction), f_c is the elastic free-energy density, while f_f denotes the contribution from flexoelectricity, the interaction between strain gradients and the polarization. Γ_{ijkl} is the flexoelectric tensor. The strain ϵ_{ij} is defined as $1/2(\nabla_i u_j + \nabla_j u_i)$ where u are the displacements; summation over repeated indices is implied.

In equilibrium, the integral of the free energy density over the entire crystal is minimized. Inside the ferroelectric domains, the electrostriction term, f_q , generates a spontaneous tensile strain along the polar direction. This tensile strain is reduced at domain wall due to the absence of polarization and leads to a depression of the surface, which is centred at the wall. When the tip is placed in contact with the surface of the material an extra compressive pressure is added, interacting with this pre-existing compressive strain profile. Then the wall moves towards the tip, so that the domain wall depression coincides with the tip compression.

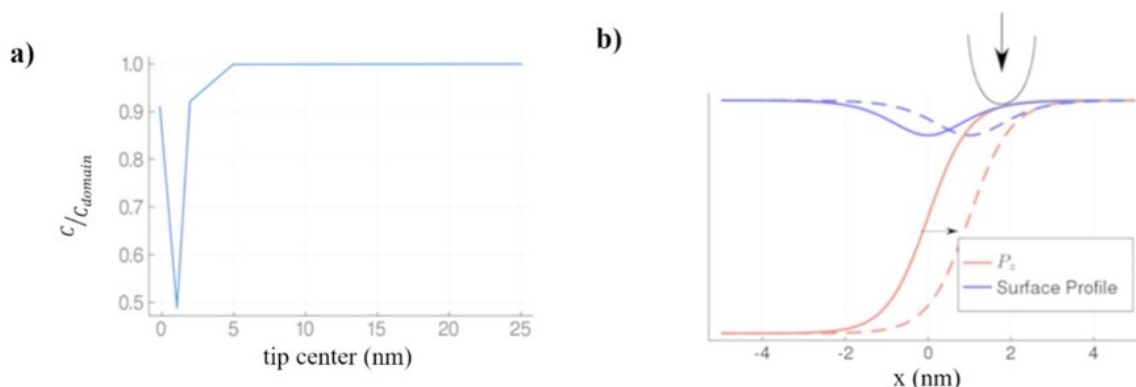


Figure 4.7: (a) Simulated change of stiffness as a function of distance between the CR-FM tip and a domain wall. The softening is maximized slightly away from the domain wall, but within its strain footprint, where the DW sliding mode contribution is important. Experimental situation corresponds to averaging within the tip region. (b) Schematic representation of the sliding mode. The polarization and strain profiles are shifted by dx .

Calculations confirm that domain wall sliding affects the mechanical response of the material [43]. The elastic cost of deformation is smallest not at domain wall itself but adjacent to it. The domain wall is already spontaneously compressed and thus is harder to compress it more. So, compression is achieved by the bending of domain wall towards the tip leading to biggest relative deformation of the material and lower effective stiffness. As the tip moves away from the wall, the stress field of the tip does not interact with the wall and the material recovers its intrinsic stiffness. **Figure 4.8** shows the simulation of strain profiles near and further away from domain

wall.

Concluding, one possible mechanism responsible for domain walls' softening is the reversible shift of domain wall's position, with its spontaneous surface dip, towards the tip, due to the local compressive stress.

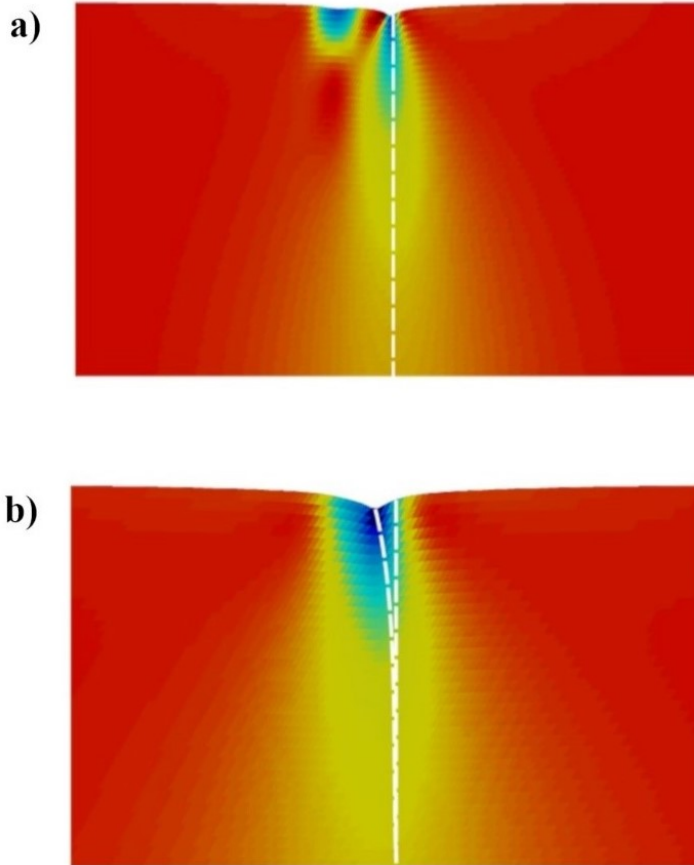


Figure 4.8: Simulated strain profiles shown on a slice of the sample when the tip is near the domain wall (a) or further away (b). The dashed vertical line shows the initial position of the ferroelectric domain wall. The wall slides towards the tip in (a), as shown by the curved dashed line, whereas it does not move in (b)

4.4.3 Static model for domain wall softening

Another possible contribution to a mechanical contrast between domains and domain walls is the impact of depolarization fields, as studied by the group of Massimiliano Stengel. Any force applied over a ferroelectric material, which is also piezoelectric, modifies its polarization and thus has an electrostatic cost of deformation. In case of inhomogeneous deformation ε_{ij} , as the one induced by an AFM tip, the induced polarization due to piezoelectricity, $P_i \sim e_{ijk}\varepsilon_{jk}$, is inhomogeneous too. In this non homogeneously deformed region, the tip pressure induces bound charges ($\nabla P \neq 0$), which create a depolarizing field. The effective stiffness of the ferroelectric

E_s is directly correlated with this depolarizing field as higher fields implies that it is more difficult to deform the material, i.e., the material is stiffer. Consequently, the mechanical response of the material should depend on the depolarizing field and bound charges.

Formation of bound charges can be caused by two main mechanisms. First, by the variation of in-plane polarization, $\nabla_1 P_1 \neq 0$, induced by shear piezoelectricity $P_1 \sim e_{15}\varepsilon_5$. This phenomenon is represented in **Figure 4.9.a**. Another cause of bound charges is the generation of out-of-plane polarization due to longitudinal piezoelectricity, $\Delta P_3 \sim e_{11}\varepsilon_3$, which is unscreened in the case of open boundary conditions and screened under short-circuit conditions, as seen in **Figure 4.9.b**.

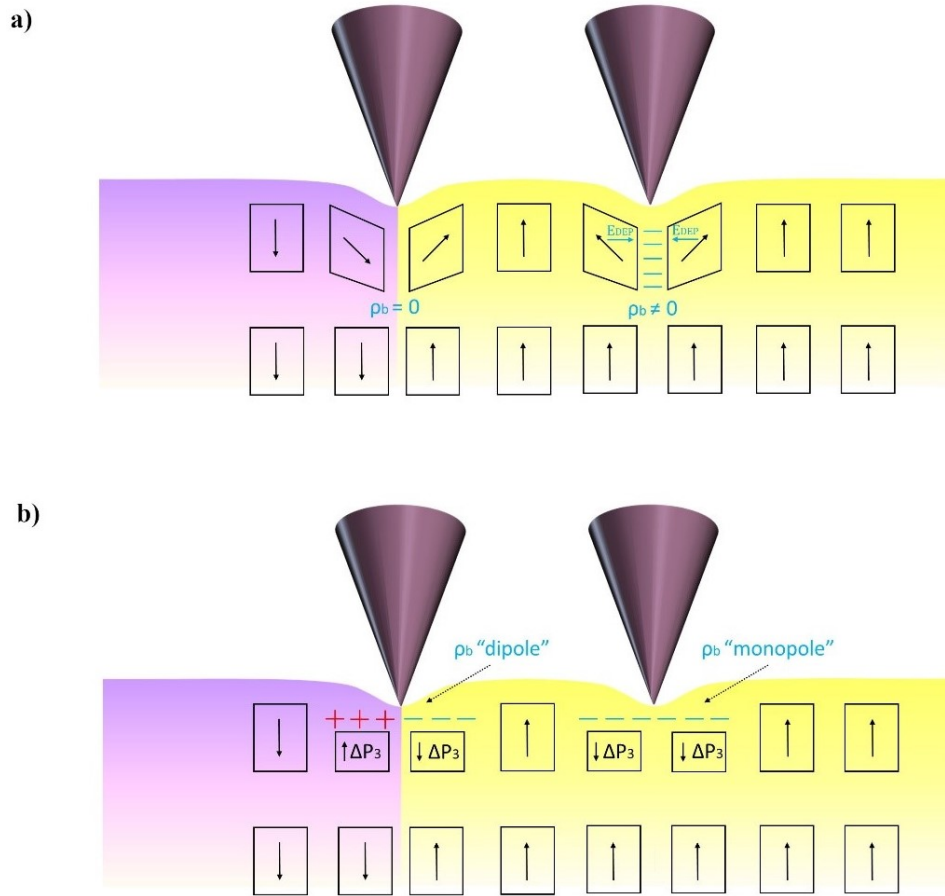


Figure 4.9: (a) Schematic of the “in-plane” mechanism of the bound charge formation: applying the tip to the surface induces in-plane polarization via the shear piezoelectricity: $P_i \sim e_{ijk}\varepsilon_{jk}$, with larger depolarizing electric fields E_{dep} when tip is applied in the bulk domain. (b) Schematic of the “out-of-plane” mechanism of the domain wall softening: applying the tip to the surface induces out-of-plane polarization $\Delta P_3 \sim e_{11}\varepsilon_3 + e_{33}\varepsilon_3$.

Domain walls are the areas where the polarization changes sign between two polar states, and particularly between two antiparallel polar states for 180° ferroelectric domain walls. Therefore,

all the piezoelectric constants e_{jm} alternate their signs across the domain wall, $e_{jm}(P_3 \downarrow) = -e_{jm}(P_3 \uparrow)$ and the distribution of tip-induced bound charges is qualitatively different for domains and domain walls. The in-plane polarization $P_i \sim e_{ijk}\epsilon_{jk}$ for the induced bound charges of a-domains (**Figure 4.9.a**) forms a head-to-head or tail-to-tail pattern with the corresponding bound charges. At a domain wall, on the other hand, the in-plane polarization forms head-to-tail patterns, implying significantly reduced electrostatic energy cost and thus, softer mechanical response. When the out-of-plane polarization configuration is considered (**Figure 4.9.b**), the generated surface charges, when the tip force is applied over a domain, have monopole-like distribution. However, when the force is applied over a domain wall, the bound charges create a dipole-like distribution, leading again to lower energy cost and consequently to softer mechanical at open electric boundary conditions. In both cases domain walls demonstrate lower effective stiffness. It is important though to clarify that this piezoelectric response is polarity-dependent and is qualitatively different from flexoelectricity, which is polarity-independent and thus insensitive to the presence of a 180° domain wall. The present analysis assumes negligible thickness of domain walls which is a reasonable assumption since domain walls' thickness is in order of few Angstrom [44]. This polarity independence is the reason for discarding flexoelectricity from the analysis.

A simplified two-dimensional modeling system was used to prove the discussion above. The contact of the tip with the surface is described again by a force in the out-of-plane direction, low enough to avoid possible effects due to ferroelectric switching of polarization. All simulations were performed for both electric boundary conditions (open and close-circuited). The last case describes more accurately the experimental conditions since AFM tips used in the experiments were conductive and grounded.

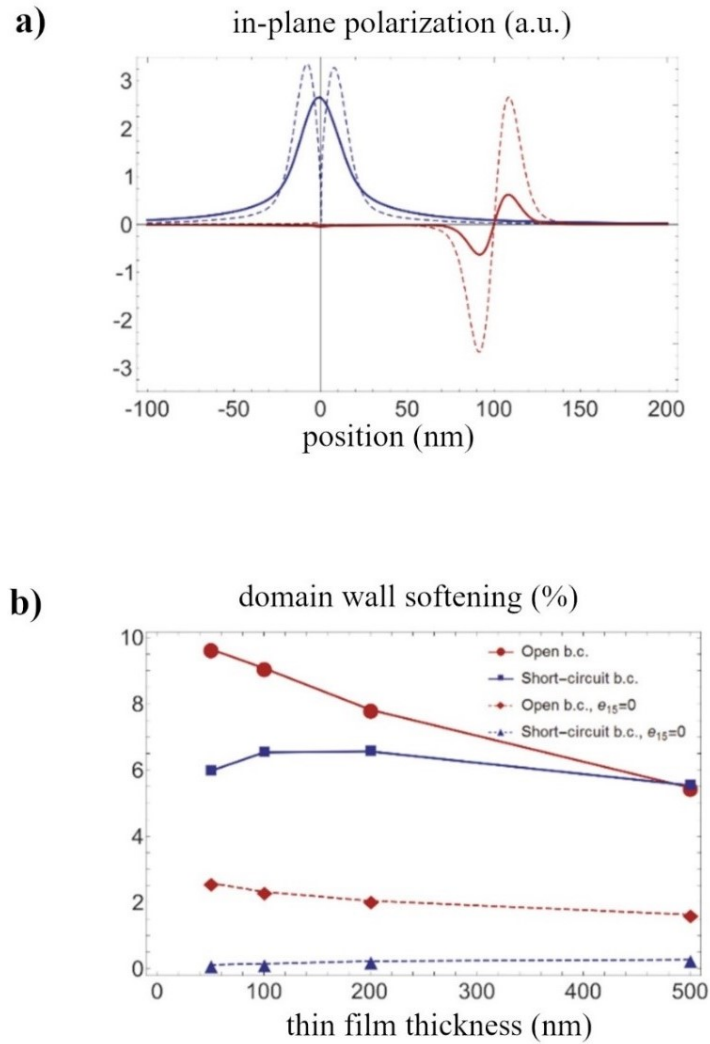


Figure 4.10: a) Manifestation of the depolarizing effect on the tip-induced in-plane polarization P_1 . Solid lines: polarization extracted from finite-element modelling at distance 5nm from the film surface, with the tip applied at the domain wall (blue) and in the bulk domain (red). Dashed lines: polarization expected due to the shear piezoelectric effect $P_1 \approx e_{15}\varepsilon_5$, with shear strain ε_5 extracted at distance 5nm from the film surface. b) Study of the domain wall softening at different electric boundary conditions, values of the shear piezoelectric coefficient e_{15} and film thicknesses.

The simulations are shown in **Figure 4.10.a**, where dash lines correspond to the piezoelectric effect $P_1 \approx e_{15}\varepsilon_5$, while solid lines demonstrate the generated in-plane polarization P_1 , under the AFM tip. Domain walls are positioned at 0 nm. When the force is applied over a domain wall, the generated in-plane polarization is described with good precision by the piezoelectric effect. On the other hand, when the tip is pressing over a bulk domain, the generated polarization is smaller than the one expected by piezoelectricity. This suppression is due to the depolarization cost of the head-to-head configuration. Therefore, domains are accompanied by a harder elastic response, as expected. Specifically, this difference is translated into an apparent domain wall

softening of 5-10% (**Figure 4.10.b**), compared to the stiffness of bulk domains. A further confirmation of the link between the suppression of in-plane polarization and elastic hardening of the domains, is achieved by vanishing the shear piezoelectric constant ($e_{15} = 0$, which is attained by setting the shear electrostriction coefficient $q_{44} = 0$ in **Equation 4.8**) and performing the same calculations in short-circuit conditions. In this way, bound charges, both in-plane and out-of-plane, are removed. The simulations result into vanishing of domain wall softening (0.3%). By setting $e_{15} \neq 0$, the in-plane mechanism of charge formation is reactivated and that leads to an averages 6% increase of the domain wall softening. Applying open boundary conditions add another 2% to the softness of domain walls (**Figure 4.10.b**).

Although it could be expected that out-of-plane piezoelectricity is the main contributor to the electrostatic softening of domain walls, simulation showed that this is not the case. Shear piezoelectricity is responsible for softer mechanical response of ferroelectric walls. The importance of such a finding is estimated if it is considered that, while out-of-plane polarization can be partially screened by the presence of electrodes or adsorbates, or using metallic tips, in-plane polarization cannot be screened. Therefore, the shear piezoelectric contribution to domain wall softening is inevitable, despite the polar axis being out-of-plane.

In summary, the performed simulations have shown that there are two intrinsic mechanisms responsible for the softer mechanical properties of 180° ferroelectric domain walls. The first one, described as the dynamic model, proves that sliding of the domain walls “strain dip” towards the tip can lead to softer effective response near domain walls. The second (static model) relies on the inhomogeneous piezoelectricity generated by the bound charges, which generates head-to-head or tail-to-tail shear polarization in the domains and head-to-tail (lower energy) at the domain walls. Both mechanisms are not mutually exclusive, meaning that both mechanisms can happen simultaneously. Additionally, both mechanisms impact only on the effective vertical elastic compliance (S_{33}), but not on S_{11} and S_{22} , which means that domain wall softening is anisotropic, as observed. This result has been experimentally confirmed as shown in **Figure 4.6.c**; while the shift in resonance frequency is remarkable in 180° domain walls separating out-of-plane polarization, it is almost negligible for 180° domain walls separating in-plane polarization.

References

- [1] J. Guyonnet, I. Gaponenko, S. Gariglio, P. Paruch. *Conduction at Domain Walls in Insulating Pb(Zr_{0.2}Ti_{0.8})O₃ Thin Films*, Adv. Mater. 23(45) (2011).
- [2] M. Schröder, A. Haußmann, A. Thiessen, E. Soergel, T. Woike, L.M. Eng. *Conducting Domain Walls in Lithium Niobate Single Crystals*, Adv. Funct. Mater. 22(18) (2012).
- [3] T. Choi, Y. Horibe, H.T. Yi, Y.J. Choi, W. Wu, S.W. Cheong. *Insulating interlocked ferroelectric and structural antiphase domain walls in multiferroic YMnO₃*, Nat Mater 9(3) (2010).
- [4] R.G.P. McQuaid, M.P. Campbell, R.W. Whatmore, A. Kumar, J. Marty Gregg. *Injection and controlled motion of conducting domain walls in improper ferroelectric Cu-Cl boracite*, Nat. Commun. 8(May) (2017).
- [5] S. Farokhipoor, B. Noheda. *Conduction through 710 Domain Walls in BiFeO₃ Thin Films*, Phys. Rev. Lett. 107(12) (2011).
- [6] J. Seidel, L.W. Martin, Q. He, Q. Zhan, Y.H. Chu, A. Rother, M.E. Hawkrigde, P. Maksymovych, P. Yu, M. Gajek, N. Balke, S. V Kalinin, S. Gemming, F. Wang, G. Catalan, J.F. Scott, N.A. Spaldin, J. Orenstein, R. Ramesh. *Conduction at domain walls in oxide multiferroics*, Nat. Mater. 8(3) (2009).
- [7] Q. He, C.H. Yeh, J.C. Yang, G. Singh-Bhalla, C.W. Liang, P.W. Chiu, G. Catalan, L.W. Martin, Y.H. Chu, J.F. Scott, R. Ramesh. *Magnetotransport at domain walls in BiFeO₃*, Phys. Rev. Lett. 108(6) (2012).
- [8] J.H. Lee, I. Fina, X. Marti, Y.H. Kim, D. Hesse, M. Alexe. *Spintronic Functionality of BiFeO₃ Domain Walls*, Adv. Mater. 26(41) (2014).
- [9] A. Aird, E.K.H. Salje. *Sheet superconductivity in twin walls: experimental evidence of WO_{3-x}*, J. Phys. Condens. Matter 10(22) (1998).
- [10] R.S. Weis, T.K. Gaylord. *Lithium niobate: Summary of physical properties and crystal*

structure, Appl. Phys. A 1985 374 37(4) (1985).

[11] R. BLINC. *Order and Disorder in Ferroelectrics*, Ferroelectrics 301 (2004).

[12] S.C. Abrahams, H.J. Levinstein, J.M. Reddy. *Ferroelectric lithium niobate. 5. Polycrystal X-ray diffraction study between 24° and 1200°C*, J. Phys. Chem. Solids 27(6–7) (1966).

[13] T. Volk, M. Wöhlecke. *Lithium niobate: Defects, photorefraction and ferroelectric switching*, Springer Ser. Mater. Sci. 115 (2009).

[14] J.E. Toney. *Lithium Niobate Photonics*, Artech House, 2015.

[15] M. Carrascosa, A. García-Cabañes, M. Jubera, J.B. Ramiro, F. Agulló-López. *LiNbO₃: A photovoltaic substrate for massive parallel manipulation and patterning of nano-objects*, Appl. Phys. Rev. 2(4) (2015).

[16] A. García-Cabañes, A. Blázquez-Castro, L. Arizmendi, F. Agulló-López, M. Carrascosa. *Recent Achievements on Photovoltaic Optoelectronic Tweezers Based on Lithium Niobate*, Cryst. 2018, Vol. 8, Page 65 8(2) (2018).

[17] E.P. Kokanyan, V.G. Babajanyan, G.G. Demirkhanyan, J.B. Gruber, S. Erdei. *Periodically poled structures in doped lithium niobate crystals*, J. Appl. Phys. 92(3) (2002).

[18] A. Labuda, R. Proksch. *Quantitative measurements of electromechanical response with a combined optical beam and interferometric atomic force microscope*, Appl. Phys. Lett. 106(25) (2015).

[19] A.A. Esin, A.R. Akhmatkhanov, V.Y. Shur. *Tilt control of the charged domain walls in lithium niobate*, Appl. Phys. Lett. 114(9) (2019).

[20] C.S. Werner, S.J. Herr, K. Buse, B. Sturman, E. Soergel, C. Razzaghi, I. Breunig. *Large and accessible conductivity of charged domain walls in lithium niobate*, Sci. Reports 2017 71 7(1) (2017).

[21] R.J. Nelmes, W.F. Kuhs. *The crystal structure of tetragonal PbTiO₃ at room temperature*

and at 700 K, Solid State Commun. 54(8) (1985).

[22] E. Langenberg, D. Saha, M.E. Holtz, J.J. Wang, D. Bugallo, E. Ferreiro-Vila, H. Paik, I. Hanke, S. Ganschow, D.A. Muller, L.Q. Chen, G. Catalan, N. Domingo, J. Malen, D.G. Schlom, F. Rivadulla. *Ferroelectric Domain Walls in PbTiO₃ Are Effective Regulators of Heat Flow at Room Temperature*, Nano Lett. (2019).

[23] G. Catalan, N. Domingo. *Physical properties inside domain walls: Basic principles and scanning probe measurements*, Domain Walls: From Fundamental Properties to Nanotechnology Concepts, Oxford University Press, (2020).

[24] Y. Liu, G. Xu, C. Song, Z. Ren, G. Han, Y. Zheng. *First-principles study of elastic properties in perovskite PbTiO₃*, Mater. Sci. Eng. A 472(1–2) (2008).

[25] N.H. Yusoff, R. Aina, M. Osman, S. Idris. *Dielectric and structural analysis of hexagonal and tetragonal phase BaTiO₃* (2020).

[26] W.C. Oliver, F.R. Brotzen. *On the generality of the relationship among contact stiffness, contact area, and elastic modulus during indentation*, J. Mater. Res. 7(3) (1992).

[27] U. Rabe, S. Amelio, M. Kopycinska, S. Hirsekorn, M. Kempf, M. Göken, W. Arnold. *Imaging and measurement of local mechanical material properties by atomic force acoustic microscopy*, Surf. Interface Anal. 33(2) (2002).

[28] K.L. Johnson. *Contact Mechanics*, Cambridge University Press, 1985.

[29] D. Passeri, F. Marinello. *Acoustic scanning probe microscopy: An overview*, NanoScience and Technology, Springer Verlag, (2013).

[30] D.C. Hurley. *Contact Resonance Force Microscopy Techniques for Nanomechanical Measurements*, Applied Scanning Probe Methods XI: Scanning Probe Microscopy Techniques, Springer Berlin Heidelberg, Berlin, Heidelberg, (2009).

[31] J.M.J. Den Toonder, J.A.W. Van Dommelen, F.P.T. Baaijens. *Relation between single crystal elasticity and the effective elastic behaviour of polycrystalline materials: Theory, measurement*

- and computation, Model. Simul. Mater. Sci. Eng. 7(6) (1999).
- [32] S. Cherifi-Hertel, H. Bulou, R. Hertel, G. Taupier, K.D. (Honorat) Dorkenoo, C. Andreas, J. Guyonnet, I. Gaponenko, K. Gallo, P. Paruch. *Non-Ising and chiral ferroelectric domain walls revealed by nonlinear optical microscopy*, Nat. Commun. 2017 81 8(1) (2017).
- [33] X.K. Wei, C.L. Jia, T. Sluka, B.X. Wang, Z.G. Ye, N. Setter. *Néel-like domain walls in ferroelectric Pb(Zr,Ti)O₃ single crystals*, Nat. Commun. 7 (2016).
- [34] G. De Luca, M.D. Rossell, J. Schaab, N. Viart, M. Fiebig, M. Trassin. *Domain Wall Architecture in Tetragonal Ferroelectric Thin Films*, Adv. Mater. 29(7) (2017).
- [35] J.C. Wojdeł, J. Íñiguez. *Ferroelectric transitions at ferroelectric domain walls found from first principles*, Phys. Rev. Lett. 112(24) (2014).
- [36] D. Lee, R.K. Behera, P. Wu, H. Xu, S.B. Sinnott, S.R. Phillpot, L.Q. Chen, V. Gopalan. *Mixed Bloch-Néel-Ising character of 180° ferroelectric domain walls*, Phys. Rev. B - Condens. Matter Mater. Phys. 80(6) (2009).
- [37] D. Berlincourt, H. Jaffe *Elastic and Piezoelectric Coefficients of Single-Crystal Barium Titanate*, Phys. Rev. 111(1) (1958).
- [38] H. Lu. *Mechanical Writing of*, Stress Int. J. Biol. Stress 59(April) (2012).
- [39] S. Kim, V. Gopalan, A. Gruverman. *Coercive fields in ferroelectrics: A case study in lithium niobate and lithium tantalate*, Appl. Phys. Lett. 80(15) (2002).
- [40] Y. Kim, H. Han, I. Vrejoiu, W. Lee, D. Hesse, M. Alexe. *Origins of domain wall pinning in ferroelectric nanocapacitors*, Nano Converg. 1(1) (2014).
- [41] P. Marton, I. Rychetsky, J. Hlinka. *Domain walls of ferroelectric BaTiO₃ within the Ginzburg-Landau-Devonshire phenomenological model* (2010).
- [42] J. Hlinka, P. Márton. *Phenomenological model of a 90° domain wall in BaTi O₃ -type ferroelectrics*, Phys. Rev. B - Condens. Matter Mater. Phys. 74(10) (2006).
- [43] C. Stefani, L. Ponet, K. Shapovalov, P. Chen, E. Langenberg, D.G. Schlom, S. Artyukhin, M. Stengel, N. Domingo, G. Catalan. *Mechanical Softness of Ferroelectric 180 ° Domain Walls*,

Phys. Rev. X 10(4) (2020).

[44] V.A. Zhirnov. *A contribution to the theory of domain walls in ferroelectrics*, J. Exptl. Theor. Phys. 35(8) (1958).

CHAPTER 5

Mechanical Properties from Electromechanical Measurements

In ferroelectric materials, flexoelectric fields couple to piezoelectric polarization promoting changes on the mechanical properties of ferroelectric materials at the nanoscale, as a function of the direction of their ferroelectric polarization. I have shown that CR-AFM mode exploits this induced mechanical unevenness between oppositely polarized domains and thus can be used as an effective and non-destructive tool to mechanically read the ferroelectric polarization. Additionally, mechanical properties of domain walls have been thoroughly investigated, demonstrating that under the mechanical excitation of the tip, in CR-AFM mode, 180° ferroelectric domain walls are always softer than the surrounding domains. Remarkably, in all the previous chapters I focused on the study of mechanical properties of ferroelectric domains and domain walls using CR-AFM, an AFM based mode in which the tip is essentially excited mechanically: it is the strong strain gradients, induced by the AFM tip, which produce the flexoelectric fields.

The strain gradients induced by the AFM tip during CR-AFM measurements, which are responsible for the induced asymmetry in the mechanical properties of ferroelectrics, are also present in case of Piezoresponse Force Microscopy (PFM). In this mode, the tip is in contact with the sample surface while the sample is excited electrically, not mechanically, with an ac voltage applied between the tip and the sample, and the total electromechanical response of the sample is measured. While PFM amplitude and phase are directly correlated with the magnitude and direction of ferroelectric polarization respectively, when working in resonance mode, the information contained by the PFM contact resonance frequency signal is still unclear. In this chapter, I explore the contact resonance frequency signal of PFM, using advanced

AFM techniques. Band Excitation PFM and CR-AFM are used to study a multi domain distribution of ferroelectric domain walls on a BaTiO₃ single crystal, in terms of mechanical and nanomechanical response, building up their behaviour at the nanoscale and comparing the different information hidden in contact resonance frequency signals. Finally, I use Contact Kelvin Probe Force Microscopy measurements to decouple electrostatic artifacts from mechanical changes emanating from other electromechanical phenomena such as flexoelectricity. It is shown that contact resonance frequency of PFM contains information not only from electromechanical and electrostatic properties of materials but also, and more importantly, from mechanical properties of ferroelectric materials; since the mechanical behaviour of ferroelectrics at the nanoscale has been well established in the previous chapters, here I demonstrate how it is possible to deduct information about the mechanical properties of ferroelectric materials also directly from electromechanical measurements.

5.1 Electromechanical measurements of BaTiO₃ single crystal

The sample chosen to study the mechanical and electromechanical behaviour of ferroelectric domains and domain walls is a BaTiO₃ (100) single crystal (CrysTec GmbH) with a complex distribution of a/c domains. A schematic representation of domains' distribution is shown in **Figure 5.1**. In some areas of the crystal, it is possible to identify c domains with both, up and down polarization directions: it appears as a distribution of bubble-like down polarized domains (purple colour) over an up polarized background (shown in yellow). Additionally, diagonal stripes all over the sample correspond to a domains with in-plane polarization. This sample appears to be ideal for extensive mechanical and electromechanical measurements since all types of domains and domains walls can be included in a single scan.

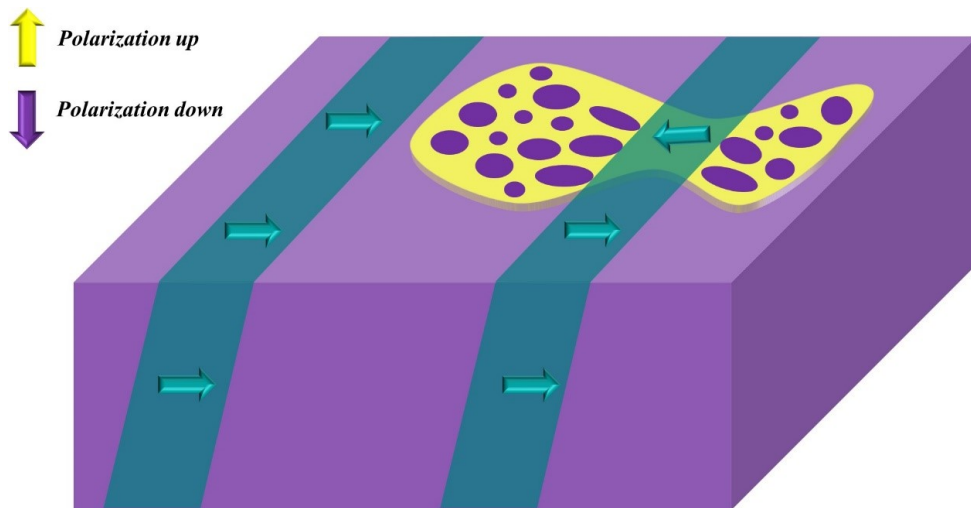


Figure 5.1: Schematic representation of BaTiO₃ (100) single crystal. The crystal is polarized out-of-plane with diagonal stripes of in-plane polarization (a domains). c domains have two possible polarization directions, up (yellow areas) and down (purple areas).

5.1.1 DART PFM and Band Excitation PFM on BaTiO₃ Single Crystal

Initially, DART PFM and Band Excitation PFM were performed on the same area of the sample. In both modes the tip is in contact with the sample and the sample is excited by an ac voltage through the tip. The main difference between these two modes lays on the way that frequency is being tracked. While in case of DART (Dual AC Resonance Tracking) PFM, the contact resonance frequency of the cantilever is tracked using only two excitation frequencies which are used to reconstruct the SHO resonance peak (see **Chapter 2** for experimental details on the

technique), in Band Excitation PFM a wide bandwidth excitation pulse is sent to the sample and the full electromechanical resonance is directly measured.

Figure 5.2 shows the PFM characterization of a BaTiO₃ single crystal as performed by DART PFM over an area of 5 μm . **Figure 5.2.a** corresponds to PFM amplitude image. Since PFM amplitude is proportional to the magnitude of ferroelectric polarization, domain walls, both ferroelastic and ferroelectric are observed with a darker contrast with respect to the domains. **Figure 5.2.b** shows the PFM phase image of the same area. As followed through the whole thesis, up and down polarized domains are denoted with yellow and purple colors respectively. Since the measurement is sensitive only to the out-of-plane polarization (vertical DART PFM measurement), the diagonal stripes that correspond to *a* domains (in-plane polarization) show an arbitrary PFM phase.

The same area of the crystal was characterized by Band Excitation PFM, as shown in **Figure 5.3**. Accordingly, **Figure 5.3.a** and **Figure 5.3.b** show Band Excitation PFM amplitude and phase images (to make the comparison straightforward, the colour scales used for these images are similar to the ones used for DART PFM measurements). Again, the PFM amplitude signal show lower values for domain walls, either ferroelectric or ferroelastic, compared to domains, and the PFM image show that oppositely out-of-plane polarized domains have a phase contrast of 180°. Comparing **Figures 5.2** and **5.3**, it is clear that electromechanical characterization by DART PFM and Band Excitation PFM corresponds to analogous results. However, in contrast with DART PFM [1], Band Excitation PFM measurements are more appropriate to deeply analyse the ferroelectric behaviour of the material and its electromechanical response since it involves a direct measurement of the full PFM electromechanical resonance [2] which can be fitted to a SHO peak function providing useful information about dissipation and also a reliable imaging of Q factor. In general, Band Excitation PFM avoids uncertainties in phase and frequency imaging, as compared to single frequency or DART methods, ending up to the most reliable nanoscale electromechanical AFM based measurement mode nowadays. For all that reasons, the following study on the mechanical and electromechanical properties of the ferroelectric BaTiO₃ is based on Band Excitation measurements. The measurements were performed on a Cypher Asylum AFM (Asylum Research – Oxford Instruments) with Band Excitation capabilities, conducted as a part of a user project at the Center for Nanophase Materials Sciences (CNMS), which is a US Department of Energy, Office of Science User Facility at oak Ridge National Laboratory.

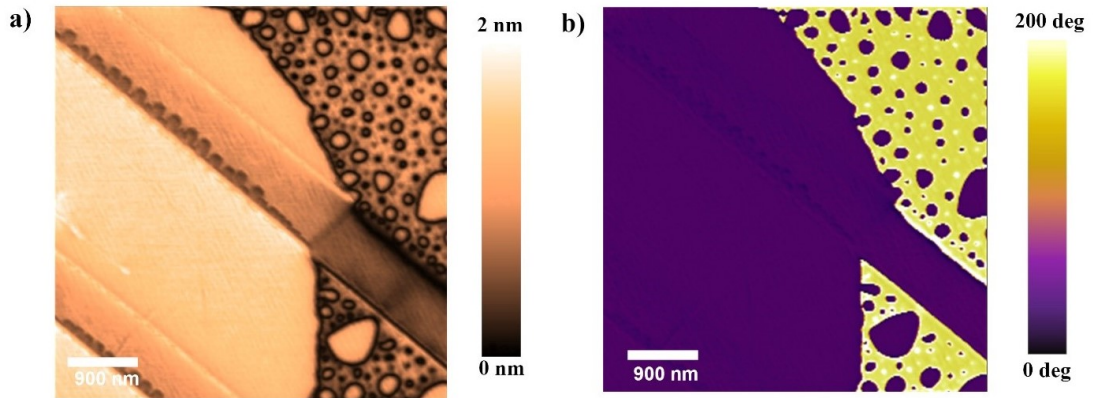


Figure 5.2: a) DART PFM amplitude image of BaTiO₃ single crystal in an area of 5x5 μm. The main area of the crystal is polarized out-of-plane (c domains) while diagonal stripes, appeared with slightly darker colour than c domains, correspond to in-plane polarization (a domains). Domain walls, separating both a-c domains (ferroelastic domain walls), and c domains polarized up and down (ferroelectric domain walls), are denoted with dark colour. b) Vertical DART PFM phase image of the same area. Out-of-plane polarized domains are presented with yellow (pointing up) and purple (pointing down) colour. The measurement was performed with PPP-NCLR tip (Nanosensors; Schaffhausen, Switzerland) with cantilever stiffness $k \sim 28$ N/m and Al coating on the detective side of the cantilever. The ac voltage that excited the sample was 2V and the applied force was $\sim 0,6$ μN.

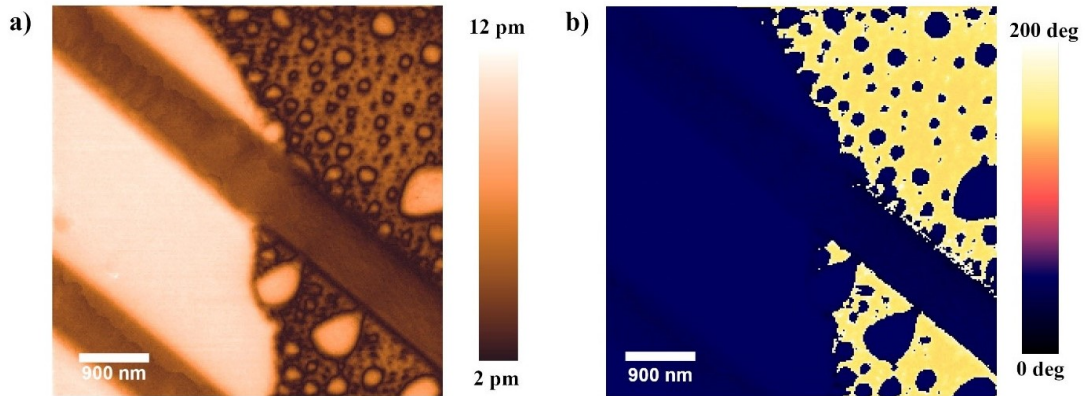


Figure 5.3: a) Band Excitation PFM amplitude image of BaTiO₃ single crystal. The scan area is 5x5 μm. Domain walls appear with darker colour than domains. b) Band Excitation PFM phase image of the same area. Diagonal stripes that correspond to in-plane polarized areas have an arbitrary PFM phase and c domains are denoted with yellow (pointing up) and purple (pointing down) colour. The measurement was performed with PPP-NCLR tip (Nanosensors; Schaffhausen, Switzerland) with cantilever stiffness $k \sim 28$ N/m and Al coating on the detective side of the cantilever. The ac voltage that excited the sample was 2V and the applied force was $\sim 0,6$ μN.

5.1.2 Data analysis of Band Excitation PFM measurements

Band Excitation PFM data require analysis of a large volume of data. Initially, the raw obtained data from Band Excitation measurements at each point of the image is fitted using a single harmonic oscillator (SHO) peak function, giving four observable magnitudes (amplitude, phase,

Q factor and frequency) and for each pixel. The fitting was performed by “Pycroscopy”, a python package for image processing. After the fitting of the data for all four observables, another programming function of Scikit python library, called StandardScaler [3], is used to scale the data. This step corresponds to the usual processing step needed prior to any clustering method. Its function is to standardize the data, so as the mean value is 0 and the variance is 1.

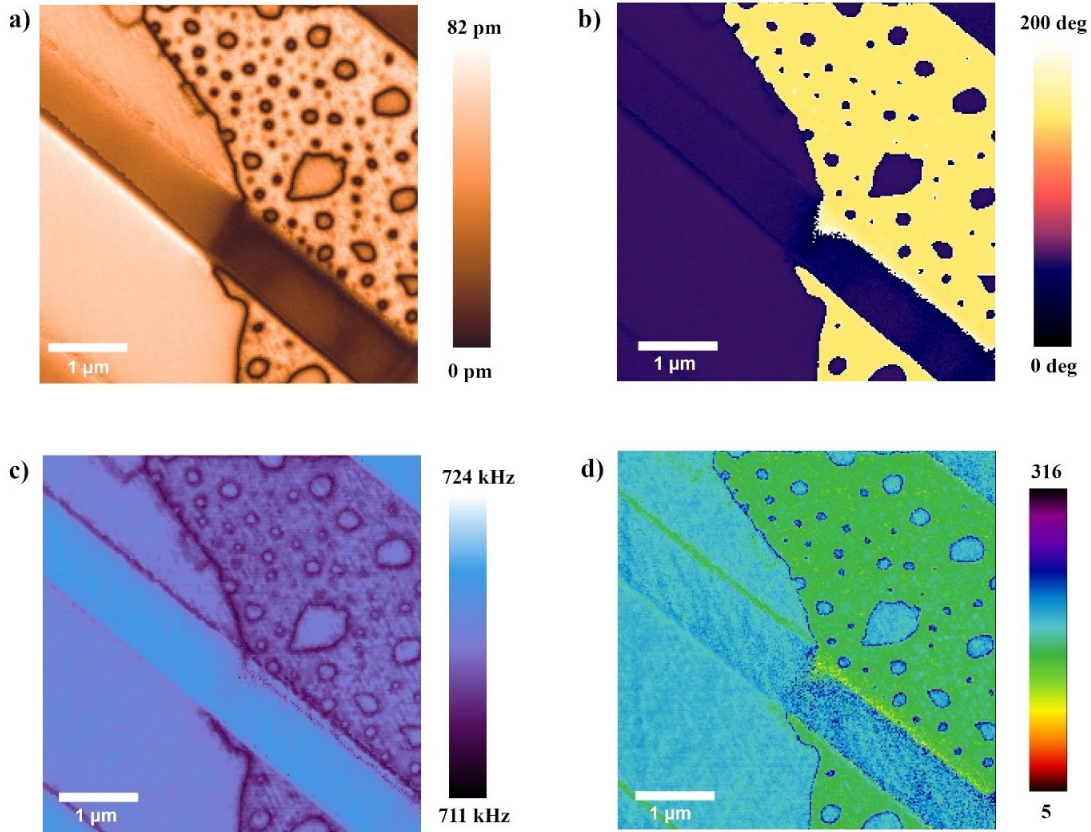


Figure 5.4: SHO fit of Band Excitation PFM data of BaTiO_3 single crystal. The observable magnitudes are amplitude (a), phase (b), frequency (c) and Q factor (d). The scan area is $5 \times 5 \mu\text{m}$. The measurement was performed with PPP-NCLR tip (Nanosensors; Schaffhausen, Switzerland) with cantilever stiffness $k \sim 28 \text{ N/m}$ and Al coating on the detective side of the cantilever. The ac voltage that excited the sample was 2V and the applied force was $\sim 0,6 \mu\text{N}$.

5.1.3 Data analysis of Band Excitation by k-means clustering

To facilitate data analysis process, and also be able to correlate the datasets with physical properties, here we used an unsupervised statistical technique, k-means clustering, as a third step of the workflow to identify the different polarization domains of the sample and its characteristic observables. The clustering of the data which is performed using the scaled parameters for each pixel, ends up to the coordinates of the centroids in the scaled parameter space. Finally, the

centroid coordinates are inversely transformed to the physical space. This analysis was performed by our collaborator Dr Marti Checa.

Optimization of k value

The k-means clustering is a method of vector quantization which is used to divide the i points (or their corresponding N_i vectors) into k clusters, minimizing the variance within each cluster. The equation used in *k-means* algorithms is the following [4,5]:

$$\operatorname{argmin} = \left[\sum_{i=1}^k \sum_{x_j \in S_i} \|x_j + \mu_i\|^2 \right] \quad (5.1)$$

where μ_i is the set of points in S_i .

The clustering is performed as a function of the number of clusters (k). The input parameters, for the case of Band Excitation PFM are four: amplitude, phase, Q-factor and frequency obtained from the fitting of an SHO function to each resonance peak measured for each pixel of the image, and all correlated with physical information about the material. The choice of the number of clusters though can be ambiguous. Increase of number of the clusters may reduce the dispersion of the mean value in a cluster, but also can lead to overfitting of the data. Different methods have been suggested to solve the problem of k -value selection, such as Elbow method and Silhouette coefficient [6]. For the datasets of Band Excitation PFM on BaTiO₃ single crystal, we started with trials for different numbers of clusters (k). **Figure 5.5** shows the obtained results for different k values. For low k values (i.e.: $k = 2$) data tend to cluster with a dominant input feature (**Figure 5.5.a**). For higher values of k (i.e.: $k = 10$), the datasets are clustered around 10 different mean values (**Figure 5.5.i**) which, turns into data overfitting and has no physical meaning.

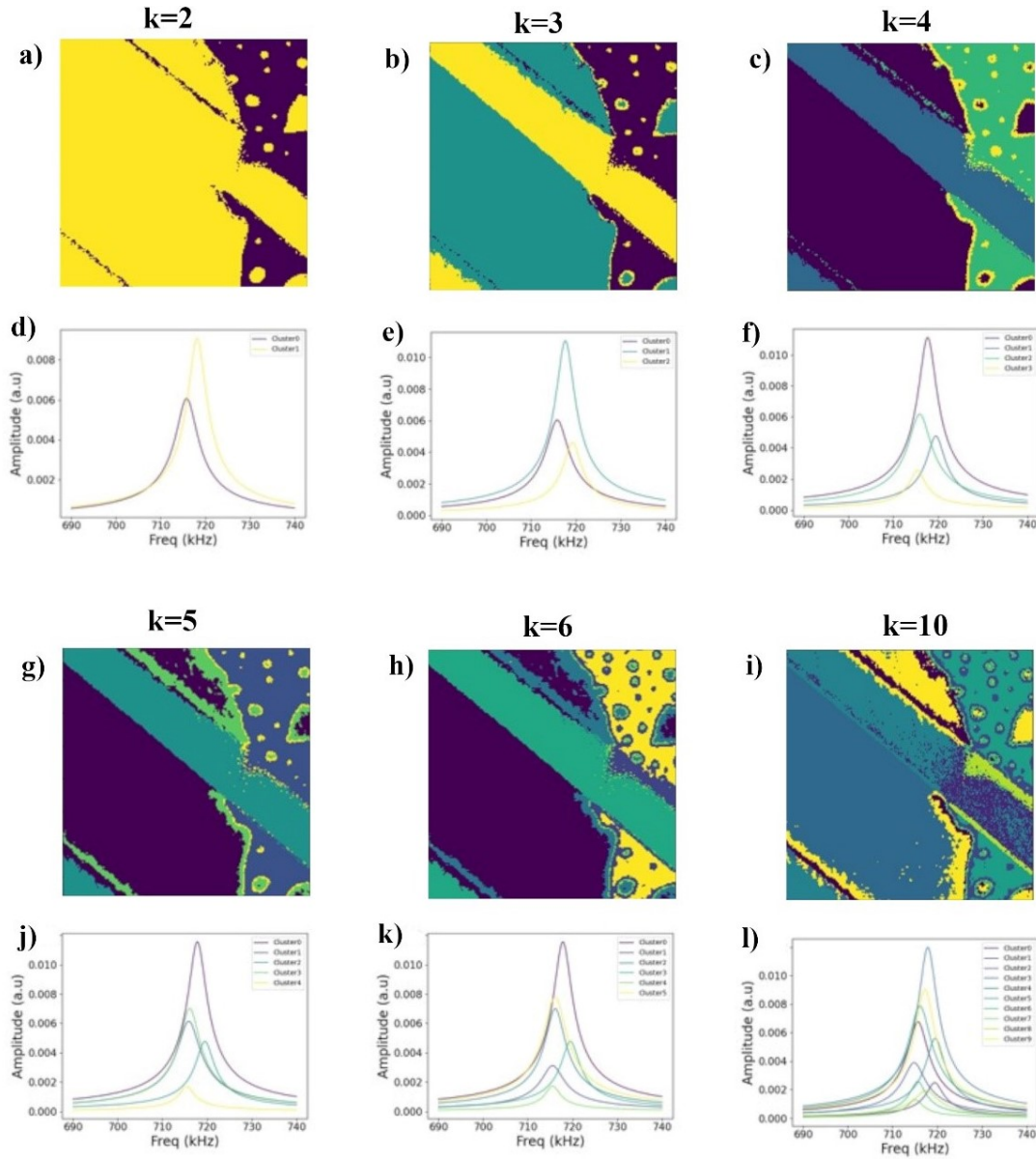


Figure 5.5: Clustering maps for increasing number of k values from 2 to 10 (a,b,c,g,h,i) and the corresponding centroids of the clustered maps (d,e,f,j,k,l).

The choice of an appropriate k value for the dataset of Band Excitation PFM measurements was made by calculating the inertia (the sum of squared distances to the cluster centre in the parameter space) as a function of k . The inertia plot of the k means (**Figure 5.6**) shows the behaviour of k means as we increase the value of k . More specifically, increase of k values lead to a decrease of inertia, as expected, meaning that for higher number of clusters, the error is smaller. This plot helps as an initial approach to the problem of k value selection, but still is not sufficient to define the ideal k . As a second

step, we computed the Silhouette coefficient for k values ranging from 2 to 20. The Silhouette coefficient computes the cohesion and separation of the samples, which stand for the similarity within their own cluster, compared with the other clusters [7]. The formula used to calculate the Silhouette coefficient is:

$$\text{SilhouetteCoefficient} = \frac{b - a}{\max(a, b)} \quad (5.2)$$

where a is the distance inside the cluster and b is the distance between the sample and the nearest cluster that is not a part of it [3]. The values of the coefficient range from -1 to 1, and more efficient clustering corresponds to higher values of the coefficient. **Figure 5.6** is a combined plot of k means inertia and Silhouette coefficient for a range of k values. Based on this plot, it is shown that the optimum value of clusters (k) for Band Excitation PFM measurements on BaTiO₃ single crystal is four.

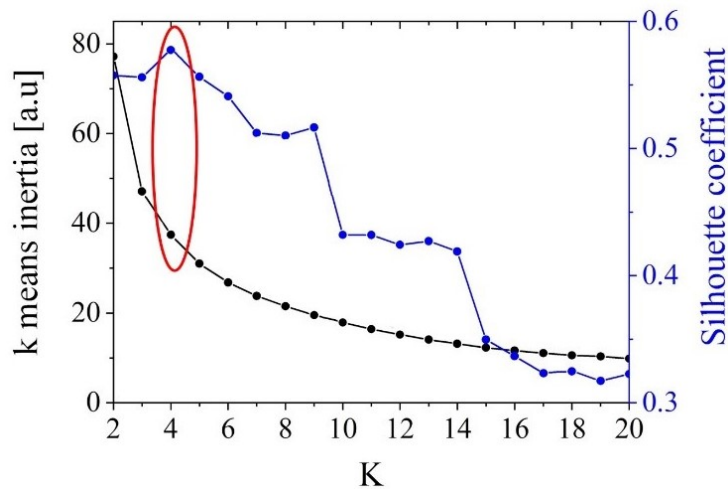


Figure 5.6: Inertia of k means (black plot, left axis) and Silhouette coefficient (blue plot, right axis) as a function of k values. The optimum number of clusters ($k=4$) corresponds to the higher value of Silhouette coefficient.

Centroids calculation and analysis

From the clustering maps shown in **Figure 5.5 c**, it can be observed that the optimized number of the clusters – four – can be correlated to the domains with different direction of ferroelectric polarization and to the domain walls. **Figure 5.7** shows the final image of BaTiO₃ single crystal, of the same scan area as the initial DART PFM and Band Excitation PFM measurements (**Figure 5.2** and **Figure 5.3** accordingly), after performing the above-

described k means analysis for $k=4$. Specifically, the light blue clusters correspond to a domains polarized in-plane, domains polarized out-of-plane with down polarization are gathered in dark blue areas, and the ones with up polarization are identified under the yellow clustered regions. Finally, domain walls clearly pop up in green. From the plot of the corresponding mean SHO function (centroid) (**Figure 5.6.c**) for each cluster, we can also obtain the mean value of the contact electromechanical resonance frequency and the amplitude for each area. The mean observable values for each cluster are presented in **Table 5.1**.

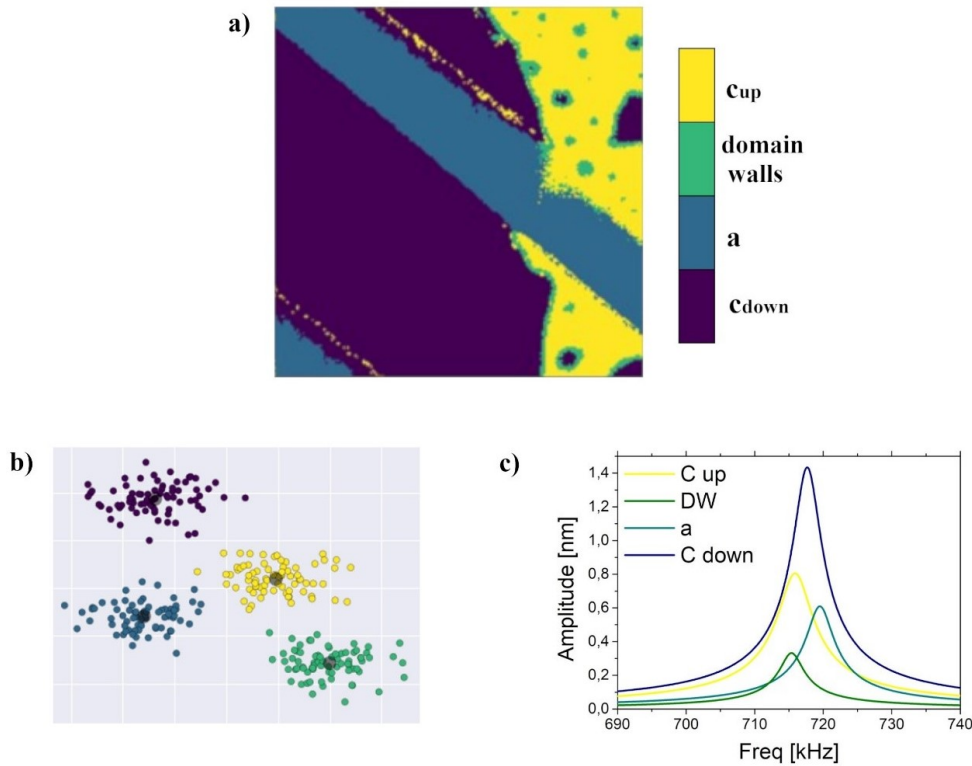


Figure 5.7: k -means clustering map of Band Excitation PFM measurement showing the different polarization domains of the BaTiO₃ single crystal. a) Optimized k -means analysis of the BaTiO₃ surface area with $k=4$ b) Clustering of the observables. c) Plot of the SHO functions averages for each cluster with the inverse scaled centroid coordinates.

	a domains	c domains down	c domains up	domain walls
Frequency (kHz)	719.5	717.7	715.9	715.4
Amplitude (pm)	33	80	15	18
Q value	190	150	179	220

Table 5.1: Values of contact resonance frequency of Band Excitation PFM for different domains and domain walls, as obtained by k means analysis on BaTiO₃ single crystal.

Higher values of contact resonance frequency correspond to a domains while in-plane

and out-of-plane domains demonstrate a small difference in contact resonance frequency values with domains polarized down to correspond to higher values. Accordingly, lower values of frequency and amplitude correspond to domain walls. The values of PFM amplitude, as calculated by k means analysis, are higher for c domains polarized down and lower for up-polarized domains. While a domains correspond to the highest contact resonance frequency values, their amplitude is small as they should not contract/ expand much in the direction vertical to sample's surface. Q factor is also calculated and is inversely proportional to amplitude: lower values of amplitude correspond to higher values of Q factor.

5.2 Mechanical measurements of BaTiO₃ single crystal

5.2.1 Band Excitation CR-AFM on BaTiO₃ Single Crystal

After the characterization of the electromechanical properties of BaTiO₃ using Band Excitation PFM, we proceed to the study of the nanomechanical response of the crystal, using Band Excitation Contact Resonance Atomic Force Microscopy (CR-AFM). Similar to PFM, the operation principle of this mode is same as the DART CR-AFM, but the whole system is vibrated mechanically, and the shifts in contact resonance frequency of the system are directly correlated with changes in the stiffness of the material (details about the mode can be found in **Section 2.4**). However, in this case, the difference between DART CR-AFM and Band Excitation CR-AFM is on the way that the system of the tip and the sample are mechanically excited. While the study of the mechanical properties of ferroelectric domains and domains walls, as described in **Chapters 3** and **4**, were performed by an MFP – 3D Asylum AFM (Asylum Research – Oxford Instruments), Band Excitation experiments were performed on a Cypher Asylum AFM (Asylum Research – Oxford Instruments) as a part of a user project at the Centre for Nanophase Materials Sciences (CNMS): in the first case, the cantilever was mechanically excited by a piezo element placed at the base of the cantilever and in second case, the cantilever was excited mechanically through thermal excitation (a laser is pointing at the base of the cantilever, heating it up and causing its mechanical vibration). Albeit in both cases the excitation

of the cantilever is controlled, in the first case by controlling the applied voltage on the piezo element, and in the second one by controlling the power of the laser beam, thermal excitation by the so-called blue drive mode led to a much clean and well-defined mechanical resonance.

Figure 5.8 shows the mechanical characterization of BaTiO_3 single crystal, as performed by Band Excitation CR-AFM, on the same area where the previous electromechanical measurements were performed (**Figure 5.6.a**). **Figure 5.8.a-d** correspond to amplitude, phase, resonance frequency and Q factor accordingly. Although there is a weak sign in amplitude and phase images, and a stronger response of Q factor, no relevant information is obtained from these images and all the information about mechanical properties is mainly extracted from the contact resonance frequency response (**Figure 5.8.c**) which thus, will be the focus of our study.

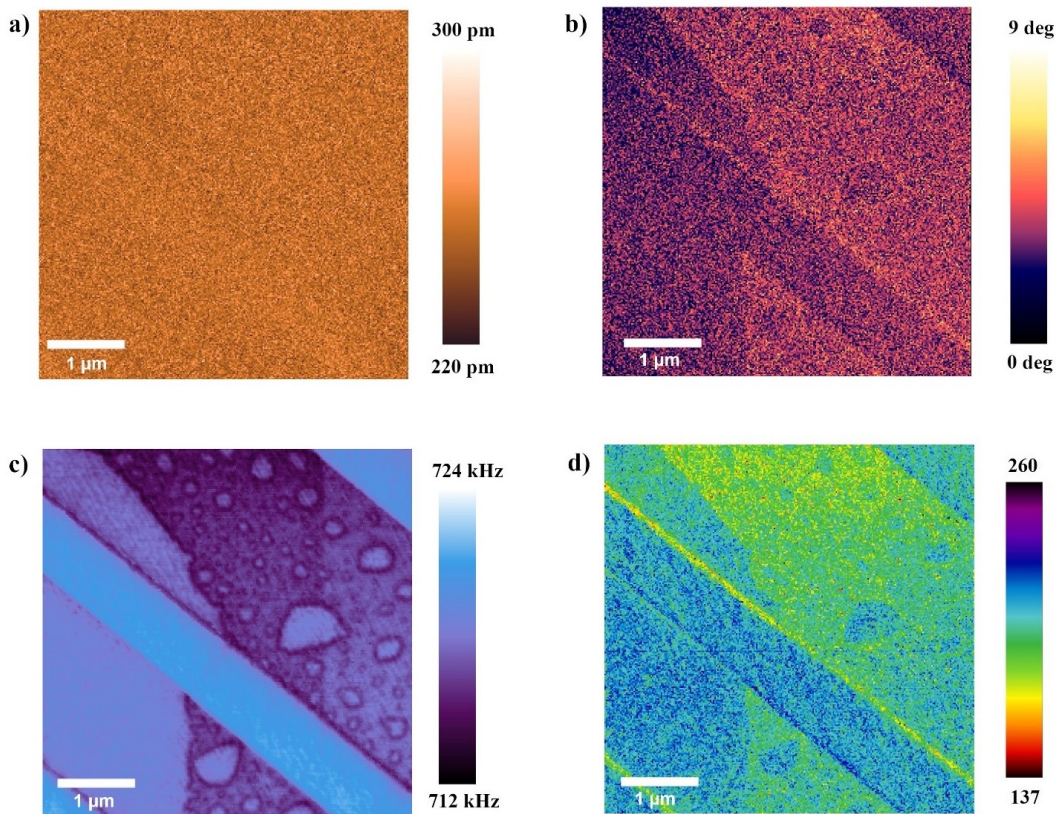


Figure 5.8: Band Excitation CR-AFM measurement on BaTiO_3 single crystal. The scan area is $5 \times 5 \mu\text{m}$. The images correspond to a) amplitude, b) phase, c) resonance frequency and d) Q factor. The measurement was performed with PPP-NCLR tip (Nanosensors; Schaffhausen, Switzerland) with cantilever stiffness $k \sim 28 \text{ N/m}$ and Al coating on the detective side of the cantilever. The applied force on the sample was $\sim 2,6 \text{ N}$.

5.2.2 Data analysis of Band Excitation CR-AFM measurements

In case of Band Excitation PFM measurements, the important observables were four (phase, amplitude, frequency, and Q factor), making the analysis of the obtained data more complex and forcing the use of statistical tools (k means analysis). Contrariwise, in case of Band Excitation CR-AFM, the important observable is only one: contact resonance frequency. This is the reason why the analysis of Band Excitation CR-AFM data is performed by using histogram analysis, as in case of DART measurements.

Figure 5.9 displays the contact resonance frequency as obtained by Band Excitation CR-AFM and the corresponding histogram. Regarding **Figure 5.9.a**, the diagonal stripes, which correspond to in-plane polarized domains, have a higher value of contact resonance frequency, as expected. Additionally, red and light blue colours correspond to up and down out-of-plane polarized domains respectively, showing that there is a difference in mechanical properties between opposite polarized domains. This behaviour is extensively discussed in **Chapter 3**. Finally, dark blue colour, that corresponds to the lower values of contact resonance frequency, correspond to ferroelectric domain walls. The fact that 180° domain walls are softer than the domains that they separate, studied and presented into details in **Chapter 4**, is also confirmed here.

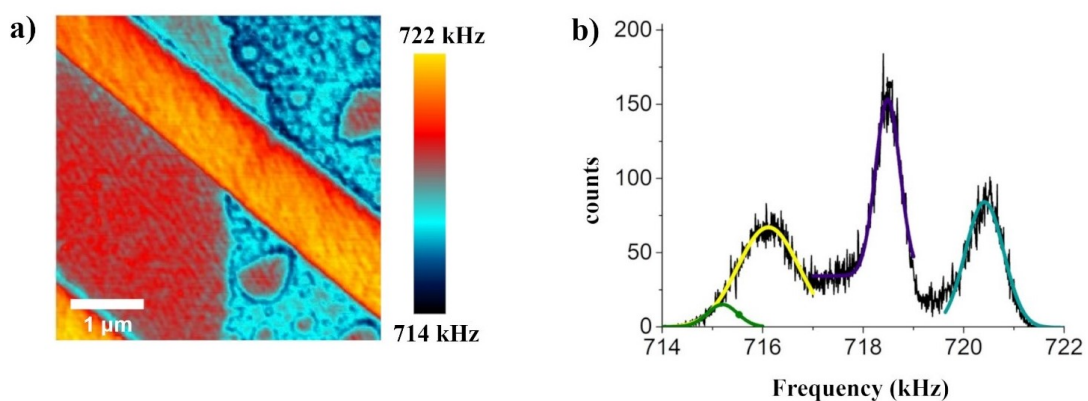


Figure 5.9: a) Contact resonance frequency image of Band Excitation CR-AFM measurement on BaTiO_3 single crystal. Colours in the range of blue correspond to lower values of frequency and thus softer mechanical response of the material. Red- and orange-coloured areas correspond to higher values of contact resonance frequency. The scan size is $5 \mu\text{m}$. The applied force on the sample was $\sim 2,6 \text{ N}$ and the cantilever used is PPP-NCLR (Nanosensors; Schaffhausen, Switzerland) with a stiffness of $k \sim 28 \text{ N/m}$ and Al coating on the detective side of the cantilever. b) Histogram of image (a) showing that there are four mean values of contact resonance frequency.

The histogram of the contact resonance frequency image, as presented in **Figure 5.9.b**, shows the distribution of contact resonance frequency values and the peaks are fitted using the Gaussian equation. The histogram denotes the presence of four characteristic resonance frequencies on the surface of BaTiO₃. Their mean values are presented in **Table 5.2**. Each peak corresponds to areas with different ferroelectric polarization, proving that there are four main polarized areas in the area under study: in-plane domains, out-of-plane domains in both directions (pointing up and down) and domain walls.

	a domains	c domains down	c domains up	domain walls
Frequency (kHz)	720.4 ± 0.4	718.5 ± 0.2	716.1 ± 0.6	715.2 ± 0.4

Table 5.2: Values of contact resonance frequency of Band Excitation CR-AFM for different domains and domain walls, as obtained by the histogram analysis.

Changes in the contact resonance frequency are in accordance with mechanical response of ferroelectric domains and domain walls as discussed in previous chapters. An interesting information we can derive from CR-AFM characterization of the material is the behavior of Q factor. **Figure 5.8.d** shows that up and down polarized domains correspond to different values of Q factor and c domains polarized down (stiffer domains) have higher Q factor. Quality factor (Q) describes energy losses in the system. While in ferroelectrics energy losses can be originated from elastic, dielectric and piezoelectric properties of the material [8], the energy dissipation (and hence the quality factor) of a ferroelectric material under mechanical vibration is proportional to the frequency of excitation [8] with higher frequencies to correspond to higher values of Q factors and less energy dissipation. Meaning that energy loss is inversely proportional to the stiffness of the material, as also seen by the experimental results shown in **Figure 5.8**. One should be careful here as the proportionality of stiffness and quality factor in ferroelectrics is valid only for domains with parallel polarity. The comparison of energy dissipation and quality factors in domain with different orientation of polarization is not straight-forward.

5.3 Quantification of CR-AFM results

Band Excitation CR-AFM was used to study a BaTiO₃ single crystal with a multidomain distribution, in order to map the nanomechanical response of different domains and

ferroelectric domain walls. The value of resonance frequency in the frame of CR-AFM mode, and in contact AFM in general, is directly correlated with the mechanical coupling of the tip and the sample. This coupling can be analogized to a spring (is called contact stiffness (k^*)) and depends on the characteristics of the tip, the sample and their mechanical connection. If we consider that the geometrical characteristics of the tip remain constant over the image, then shifts in contact resonance frequency are proportional to changes in mechanical stiffness of the sample. Thus, it is possible to quantify the experimental results and calculate the difference in Young's modulus over differently polarized areas.

In order to quantify the differences experimentally observed on the contact resonance frequency experimentally in both the Band Excitation PFM and the Band Excitation CR-AFM, different hypothesis can be driven. On one hand, as described in **Chapter 3**, we expect that the AFM tip-induced flexoelectric fields couple to the ferroelectric polarization of the c domains inducing a relative softening or hardening of the domains as a function of the orientation of the polarization. This will be discussed in **Section 5.3.2**. However, in this material, the up-polarized domains contain a distribution of bubble-like down-polarized domains that strongly enhanced the density of domain walls present in this area. Moreover, we cannot disregard the chance that this area contains also sub-resolution domains not detectable individually by the AFM that, due to their associated domains walls, lead to an overall decrease of the stiffness within the up-polarized domain. This scenario will be considered for the quantification discussed in **Section 5.3.3**.

5.3.1 Calibration of the experimental factors

The quantification method for CR-AFM measurements described in **Appendix A** and also used in the quantification of experimental results of **Chapter 4** is applied here. Briefly, all the parameters used are either experimentally measured (e.g., free resonance frequency of the cantilever), or provided by the literature (e.g., elastic constants of silicon) or the manufacturers (e.g., material properties of the cantilever), and the quantification of the experimental results is based on the model of Rabe [9,10] and Hurley [11], where we use the parameters shown in **Table 5.3** to describe the cantilever properties. The cantilever is considered as an ideal isotropic beam and it is represented by a spring with

stiffness k_{lever} and the whole system (cantilever-sample) is represented as two springs in series (k_{lever} and k^*). A factor that should be taken into account in quantification of contact-resonance-enhanced AFM techniques as this one, is the sensitivity of cantilever's displacement. The calibration of cantilever's displacement is usually performed by static means but in general, static and dynamic sensitivities of a cantilever are not equal. This discrepancy is described by shape factor (λ) as introduced by Balke et al. [12]. Shape factor depends on the characteristics of the cantilever and contact stiffness (k^*). Small deviation of shape factor between different values of k^*/k_{lever} indicates accurate measurement of sample's surface displacement and, for type of measurements presented here, it ensures that shifts in contact resonance frequency arise only from changes in sample's stiffness. Calculations of shape factor are performed based on the model provided by Balke [12] and presented also in **Table 5.3**.

E_{lever} (GPa)	b (μm)	w (μm)	Density (kg/m^3)	L (μm)	γ	L_1 (μm)	Tip height (μm)	k_{lever} (N/m)	f_1^0 (kHz)	Tilting angle ($^\circ$)	Shape factor
160	5.34	59	2238	237	0.951	225	13.4	31.53	158	11	1.135

Table 5.3: Parameters used for the quantification of Band Excitation CR-AFM experiments on BaTiO_3 single crystal. The cantilever used is PPP-NCLR (Nanosensors; Schaffhausen, Switzerland) with stiffness k_{lever} . The parameters are the Young's modulus of the cantilever (E_{lever}) and its geometrical characteristics (thickness (b), width (w) and density). The total length of the cantilever is L while L_1 is the distance from the beginning of the cantilever until the spot where the tip is placed. The ratio of the $L_1/(L-L_1)$ is called gamma. Finally, tip height and shape factor are presented while f_1^0 refers to the free resonance frequency of the cantilever.

The equations of Hertz model [9,13] describing the mechanical contact between the tip and the sample are:

$$\frac{1}{E^*} = \frac{1 - \nu_s^2}{E_s} + \frac{1 - \nu_{tip}^2}{E_{tip}} \quad (5.3)$$

$$k^* = 2a_c E^* \quad (5.4)$$

Equation 5.3 correlates the Young's modulus of the system with the Young's modulus of the tip (E_{tip}) and the sample (E_s) and their Poisson ratios (ν_{tip} and ν_s respectively).

Equation 5.4 correlates the effective Young's modulus (E^*) with the contact stiffness (k^*) and the contact radius of the tip (a_c). Considering a spherical tip in contact with the

sample, then the contact radius of the tip can be described as:

$$a_c = \sqrt[3]{\frac{3RF_N}{4E^*}} \quad (5.5)$$

where R is the radius of the tip and F_N is the applied force from the tip to the sample. By substituting **Equation 5.5** to **Equation 5.4** we end up with a relation between effective Young's modulus (E^*) and contact stiffness (k^*), where $E^* \sim C \cdot k^* * 3/2$ (C refers to an experimental coefficient) for a spherical tip radius approximation. While in **Chapter 4** we avoid the use of the tip contact radius by directly comparing the relative change of stiffness between domains and domain walls, in this case we will approach the quantification including the contact radius, by taking advantage of i) experimental measurements with higher level of accuracy in the quantification of the experimental magnitudes such as the contact resonance frequency thanks to Band Excitation the measurements and ii) the use of a domains as reference for calibration purposes.

When considering cantilevers that are slightly tilted with respect to the surface, the tip-sample mechanical coupling is defined by two characteristic stiffnesses, one parallel (lateral stiffness k_{lat}^*) and one perpendicular to the surface (k^*). Lateral contact stiffness (k_{lat}^*) is introduced to the calculations due to the tilting of the cantilever. Since contact stiffness represents the sample-tip contact in the plane vertical to sample's surface, tilting of the cantilever means that lateral forces also affect the contact and are represented by lateral contact stiffness. Lateral forces do not depend on the elastic modulus of the sample (E) but on shear modulus (G) that describes the elasticity of the material in the plane parallel to sample's surface. The effective shear stiffness G^* depends on Poisson ration and the shear stiffness of the tip and the sample (**Appendix A**):

$$\frac{1}{G^*} = \frac{2 - \nu_s}{G_s} + \frac{2 - \nu_{tip}}{G_{tip}} \quad (5.6)$$

$$k_{lat}^* = 8aG^* \quad (5.7)$$

$$c_p = \frac{k_{lat}^*}{k_{lat}} = \frac{4G^*}{E^*} \quad (5.8)$$

The ratio between lateral and normal contact stiffness c_p has already been introduced

in the quantification of contact resonance frequency as described in **Appendix A**.

One of the advantages of using a BaTiO₃ single crystal with such a diversity of domains is to take advantage of the measurements on a domains to calibrate the experimental parameters used for the quantification of the experimental results, since a domains are well known to be stiffer than c domains. The calculations presented here include both the elastic modulus and the shear stiffness of the material. However, the quantification of shear stiffness for a material showing anisotropic distribution of Young's modulus introduces an extra degree of complexity regarding the estimation of the ratio between contact stiffness k^* and lateral contact stiffness k_{lat}^* , since the shear associated with the lateral stiffness of one type of domains will entangle with the elastic modulus of the other type of domains, since a and c domains are perpendicular within each other. This will turn in a different c_p ratio when considering a and c domains as depicted in **Table 5.4**.

	E (GPa)	G (Gpa)	ν_s	1/E*	E*	G* isotropic	$C_p = 4G^*/E^*$ (BaTiO ₃)
BaTiO ₃ a domains [14]	275,1	54	0.3	0.009	108.1	17.197	0.6361
BaTiO ₃ c domains [14]	164.9	113	0.3	0.011	87.28	23.973	1.0987

Table 5.4: Parameters used for the quantification of Band Excitation CR-AFM experiments on BaTiO₃ single crystal, with asymmetric G values for the a and c domains due to the elastic anisotropy between a and c domains. The values corresponding to the tip used here for the calculation of E^* are $E_{tip} = 160$ GPa and $\nu_{tip} = 0.23$.

To calculate the value of contact area a_c we are using the nominal values for E and G for a domains [14] described in the previous section and the value of contact resonance frequency for a domains given in **Table 5.2**. We also need the cantilever's parameters presented in **Table 5.3** and the values for the elastic constant of domains given in **Table 5.4**. The values of contact area are derived by using the model described in **Appendix A** (also including **Equation 5.4**) and are shown in **Table 5.5**.

These values agree with the cantilever geometrical characteristics obtained from SEM images after the measurements, where we could measure a tip radius of the order of ~ 135

nm of diameter, that considering an applied force of $\sim 2.6 \mu\text{N}$ is in full agreement with the expected values.

	f_1 (kHz)	k^*/k_{lever}	a_c (nm)
a domains	720.4	83.59	11

Table 5.5: Experimentally measured contact resonance frequency f_1 of a domains on BaTiO_3 single crystal. The obtained values for the effective contact stiffness k^* using the model described in Chapter 2 and the parameters of Table 5.3 and 5.4 are shown in the second column. These values are used to calculate the tip sample contact area a_c using Equation 5.5.

5.3.2 Antisymmetric flexoelectric coupling with ferroelectric polarization

In ferroelectrics under *inhomogeneous* deformation (as the one caused by an AFM tip) there are two sources of induced polarization: piezoelectricity and flexoelectricity. The two components of the respective polarization can be parallel or antiparallel, depending on the sign of the ferroelectric polarization of the material and associated piezoelectric coefficient signal. As a consequence, we have demonstrated in **Chapter 3** that the same deformation can increase or decrease the total effective polarization of the sample and since the elastic energy of the sample is proportional to the *magnitude* of the electric polarization, one should expect a divergence in Young's modulus of the material, depending on the sign of its ferroelectric polarization. Specifically, the coupling of flexoelectricity and piezoelectricity leads to stiffer nanomechanical response of down-polarized domains, compared to up-polarized domains.

To quantify the observed difference in nanomechanical response of ferroelectric materials induced by the AFM tip in contact, I assume that the elastic constants of c domains found in the literature refers to bulk values under uniform deformations, that is, without the influence of strain gradients. Therefore, the calculated Young's modulus at the nanoscale for the up and down c domains should indeed be smaller and higher respectively than the nominal Young's modulus. The results obtained using the formulas described in **Appendix A** and the parameters shown in **Table 5.3** to **5.4** are presented in **Table 5.6**.

Through the quantification of Band Excitation CR-AFM experiments on BaTiO_3 single crystal we obtain the values of Young's modulus for c domains polarized down and up. For

c down domains is $E_{c\downarrow} = 172.90 \text{ GPa}$ and for up domains $E_{c\uparrow} = 158.66 \text{ GPa}$. That means that the change in Young's modulus between oppositely-polarized domains due to the coupling of flexoelectricity and piezoelectricity is $\sim 8.6\%$. That means that flexoelectricity can induce a relative increase of 4.8% of the Young's modulus on c_{down} domains, and a relative decrease of stiffness of 3.8% for c_{up} domains. Additionally, the decrease of the Young's modulus between nominal c domains and domain walls is calculated to be about 6.7% ($E_{caverage} = 164.90 \text{ GPa}$ and $E_{dw} = 153.8 \text{ GPa}$), which fully agrees with the calculations presented on **Chapter 4**.

Domains	f_1 (kHz)	k^*/k_{lever}	Shape Factor	Young's Modulus (GPa)
a	720.4	83.59	1.135	275.1
c down	718.5	73.12	1.129	172.9
c up	716.1	70.99	1.121	158.7
domain walls	715.2	70.22	1.118	153.8

Table 5.6: Values of Young's modulus and contact stiffness for different polarized areas of BaTiO_3 single crystal, as calculated by the quantification method, when the induced asymmetry due to flexoelectric coupling is taken into consideration. The values of contact resonance frequency are obtained by the analysis of Band Excitation CR-AFM experiments. The low dispersion of the values obtained for the shape factor validate the fact that the contrast obtained emerges from intrinsic different surface mechanical properties.

5.3.3 Domain wall contribution of sub-resolution bubble domains

The distribution of up and down polarized domains on the studied BaTiO_3 single crystal is shown in **Figure 5.3**. The area that is polarized up (yellow area) is full of smaller bubble-like domains with opposite sign of polarization (c down domains). Bubble-like domains vary in size and we cannot exclude the possibility of bubble-like domains with diameter smaller than the spatial resolution of AFM tip (hundreds of nanometres). If we consider that c_{up} domains contain a distribution of sub-resolution bubble-like domains, then their total nanomechanical response might be affected by the higher unknown density of domain walls. Specifically, since we have proven that 180° ferroelectric domain walls are softer than the surrounding domains [15] (see **Chapter 4** for details), the Young's modulus of c_{up} domains could be strongly decreased due to the presence of sub-resolution

domain walls.

In this scenario, I consider that the asymmetry between up and down polarized domains do not arise from strain gradients and the induced flexoelectricity, but from the presence of domain walls in the area of c_{up} domains. The results are presented in **Table 5.7**.

Domains	f_1 (kHz)	k^*/k_{lever}	Young's Modulus (GPa)
a	720.4	87.30	275.1
c down	718.5	75.99	165.54
c up	716.1	73.78	150.81
domain walls	715.2	72.97	145.81

Table 5.7: Values of Young's modulus and contact stiffness for different polarized areas of $BaTiO_3$ single crystal, as calculated by the quantification method, considering the presence of sub-resolution bubble-like domains. The values of contact resonance frequency are obtained by the analysis of Band Excitation CR-AFM experiments. The values of Young's modulus of a domains and c_{down} domains are found in literature [14] and used for calibration.

From the experimental observed shift on the contact resonance frequency, the obtained value for the c_{down} domains of $E_{c\downarrow} = 165.54 \text{ GPa}$ is as expected very close to the theoretical value for bulk c_{down} domains. Based on these calculations, the overall decrease of the Young's modulus of the c_{up} domains due to the presence of domain walls should be of $\sim 11.6\%$, much higher than the relative change due to the induced flexoelectric coupling to ferroelectricity. In this case, the relative difference between c domains polarized down and domain walls, with $E_{c\downarrow} = 165.54 \text{ GPa}$ and $E_{cdw} = 145.81 \text{ GPa}$, is about $\sim 12\%$, also above the measured values in the previous Chapter.

In order to quantify the density of domain walls necessary to recover the experimental softening found in the c_{up} domains, we used a very simplistic model where the resonance frequency measured in the c_{up} domains is a linear combination of the characteristic resonant frequency of the 180° domain walls and the characteristic resonant frequency of the c_{down} domains (assuming there is no flexoelectric coupling, thus pure c_{up} and c_{down} domains should have the same mechanical response) multiplied by the percentage of area that they occupy:

$$A_{up,total}f_{up} = A_{DW}f_{DW} + (A_{up,total} - A_{DW})f_{down} \quad (5.9)$$

where $A_{up,total}$ is the area occupied by c_{up} domains in the image ($\approx 19.3\mu\text{m}^2$), f_{up} , f_{down} and f_{DW} are the resonant frequencies of the c_{up} , c_{down} domains and domain walls respectively (716.1kHz, 718.5kHz and 715.2kHz). Then, the only unknown is the total area that the domain walls occupy (A_{DW}):

$$A_{DW} = \frac{A_{up,total}(f_{up} - f_{down})}{(f_{DW} - f_{down})} = 0.73A_{up,total} \quad (5.10)$$

From this estimation, we obtain that the 73% of the total area of the c_{up} domains should be occupied by the aforementioned sub-resolution domain walls to assume that their presence is the responsible of the apparent global softening of the c_{up} domains, which turns to be a highly unrealistic scenario.

To summarize, we have used two different scenarios to calculate the absolute change of the nanoscale Young's modulus emerging from the observed contrast in the contact resonance frequency, based on two different hypotheses: the coupling of the tip-induced flexoelectric fields to the ferroelectric polarization and the presence of sub-resolution bubble-like domains in our cup polarization area, inducing a high density of hidden 180° domain walls known to be softer than ferroelectric domains. Albeit the calculations obtained for the second scenario make it highly unrealistic, confirming that most probably the observed asymmetry in the nanomechanical response between c_{up} and c_{down} domains arises from the coupling of flexoelectricity and ferroelectricity, we cannot disregard that the real picture could include a combination of both effects.

5.4 Comparison of Band Excitation PFM and CR-AFM

Band Excitation CR-AFM measurements on BaTiO_3 single crystal provided us with information about the nanomechanical response of different domains and domain walls through contact resonance frequency. But mechanical measurements (CR-AFM) do not differ greatly from electromechanical measurements (PFM). In both cases the tip is brought into contact with the surface of the sample applying a constant force. This constant force induces strain gradients which are responsible for the aroused asymmetry in nanomechanical response between oppositely-polarized domains. Therefore, the information about the

mechanical properties of ferroelectric domains should be also hidden in the signal coming from electromechanical measurements.

Figure 5.10 shows the contact resonance frequency of both Band Excitation PFM and CR-AFM measurements on the same area of the crystal. The measurements were performed using the same experimental parameters and same tip. The colour scale in both images is the same for the sake of comparison.

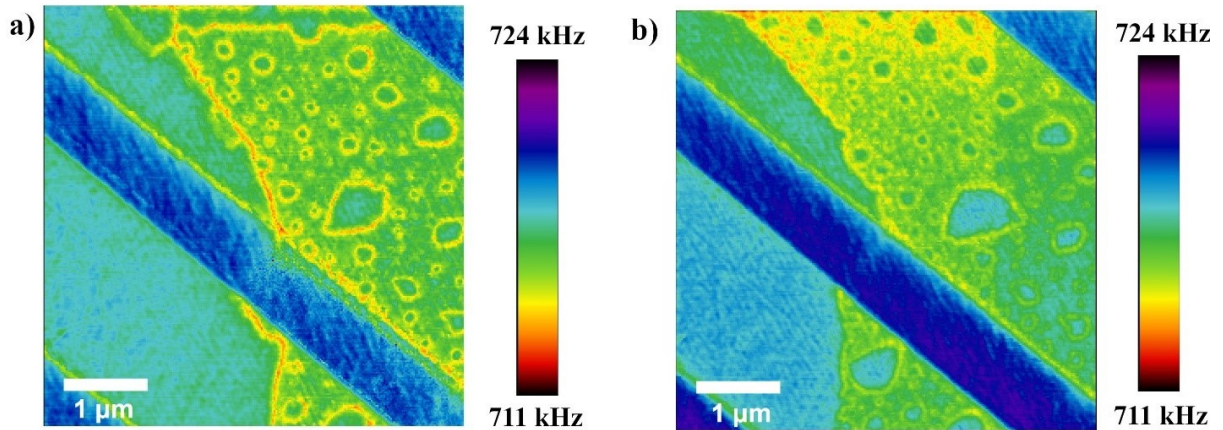


Figure 5.10: Contact resonance frequency of Band Excitation PFM (a) and Band Excitation CR-AFM (b) measurement on BaTiO_3 single crystal. The scan area was $5 \mu\text{m}$. The tip used is PPP-NCLR type (Nanosensors; Schaffhausen, Switzerland) with cantilever stiffness $k \sim 28 \text{ N/m}$ and Al coating on the detective side of the cantilever. The applied force on the sample was $\sim 2,6 \mu\text{N}$.

From the figure above, it is clear that the contact resonance frequency of Band Excitation PFM and CR-AFM behave in a similar way. In order to be able to compare in more detail the response of contact resonance frequency in both modes, it is useful to check the behaviour for each domain (a domains, c_{up} and c_{down} domains) after the SHO fitting. **Figure 5.11** shows the SHO fittings for both measurements for each domain. **Figure 5.11.a** corresponds to Band Excitation PFM measurement, while **Figure 5.11.b** shows the contact frequency of Band Excitation CR-AFM measurement. From the plots of SHO fittings, we can discern that there is a shift in contact resonance frequency, not only between a and c domains, but also between up and down polarized domains for both measurements. Additionally, using the SHO fittings shown here, in combination with histogram analysis, the difference in contact resonance frequency between domains can be calculated numerically. Specifically, for PFM measurements, the difference between up and down domains is $\sim 1.8 \text{ kHz}$, while for CR-AFM measurements, the difference in

contact resonance frequency between oppositely polarized domains have been calculated ~ 2.4 kHz.

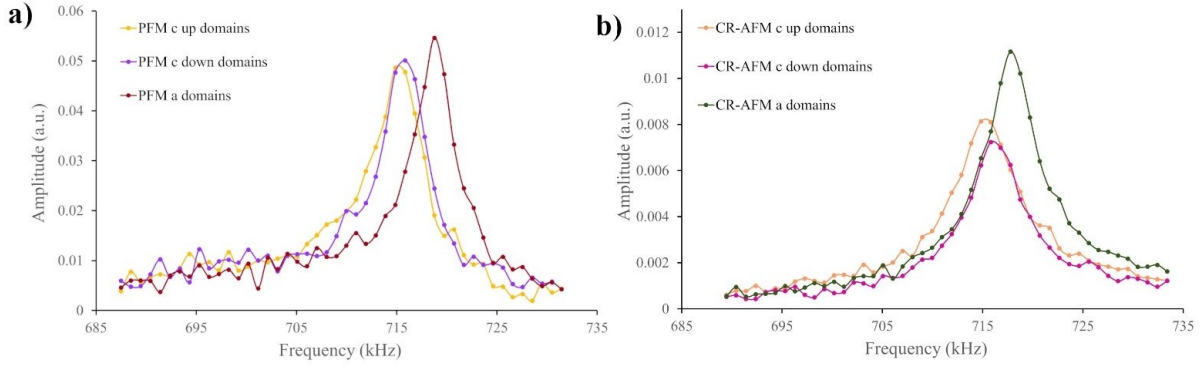


Figure 5.11: a) SHO fitting of Band Excitation PFM measurements on BaTiO_3 for a, c up and c down domains. b) SHO fitting of Band Excitation CR-AFM measurements on the same sample, for every domain.

However, both **Figures 5.10** and **5.11** demonstrate that the behaviour of contact resonance frequency is very similar for mechanical and electromechanical measurements of ferroelectric materials. In this sense, we can state that Band Excitation PFM measurements clearly enclose information about the mechanical properties of materials, and in order to correctly interpret Band Excitation PFM data it is essential to consider not only electromechanical phenomena but also how they are affected by mechanical properties.

It is useful to mention that while both AFM modes are contact modes, meaning that there is always a force applied on the sample (causing strain gradients and flexoelectric phenomena that induce asymmetry in the mechanical response of the sample), there is a main difference between these modes based on the way that the sample is excited: while in CR-AFM the sample is excited mechanically, causing vibration of the system (tip-sample), in case of PFM, the sample is excited electrically with an *ac* voltage through the tip. The magnitude of this voltage is always smaller than the coercive field of the sample, avoiding the switching of ferroelectric polarization. However, this applied *ac* voltage that leads to inverse piezoelectric effect that is being measured in PFM might also be responsible for electrostatic forces created between tip and sample that can perturb the measurements.

Up to now, asymmetries observed in the PFM signal on resonance have traditionally been assigned to uncontrolled electrostatic coupling between the tip and the sample, or

as artifacts emerging from long-range coupling with the cantilever. From all the above, it is to be expected that tip-induced flexoelectric fields will have an impact not only on net mechanical properties, as observable by both, Band Excitation CR-AFM and Band Excitation PFM, but also on net ferroelectric properties. To further investigate its net contribution and decouple the electromechanical total signal from the electrostatic influences on the PFM response, we perform Band Excitation Contact Kelvin Probe Force Microscopy (cKPFM) experiments on BaTiO₃ single crystal.

5.4.1 Contact KPFM on BaTiO₃ Single Crystal

The main idea of cKPFM operation is that for every pixel of the image, multiple hysteresis loops are measured while changing the applied voltage during the readout process. This allows the determination of the response of the sample as a function of bias and provides information about the electrostatic forces between the tip and sample, to be decoupled from the net electromechanical response. The operational principle of cKPFM is described in **Section 2.3**. The main points are explained here briefly.

An *ac* voltage is exciting the sample ($V_{ac} = 2V$ for this measurement), while the tip displacement (D_{ac}) is being measured. At the same time a *dc* voltage is ramped (V_{read}). The purpose of this voltage is to detect the junction contact potential difference, that is, the voltage at which the electromechanical signal disappears. Finally, in order to have information about the charge injection into the sample, an additional *dc* voltage is applied (V_{write}), before recording the response of the sample for every pixel [16,17]. Since cKPFM is also a Band Excitation mode (for this case), the frequency of the *ac* voltage is a range of frequencies around the contact resonance frequency. Additionally, the applied voltages are smaller than the coercive field of the sample, assuring that no switch of ferroelectric polarization will take place.

The linear behaviour of tip displacement (D_{ac}) as a function of the ramped *dc* voltage V_{read} can give us information about the strength of the electrostatic contribution. The corresponding results of cKPFM measurement for a range of V_{read} and V_{write} are shown in **Figure 5.12**.

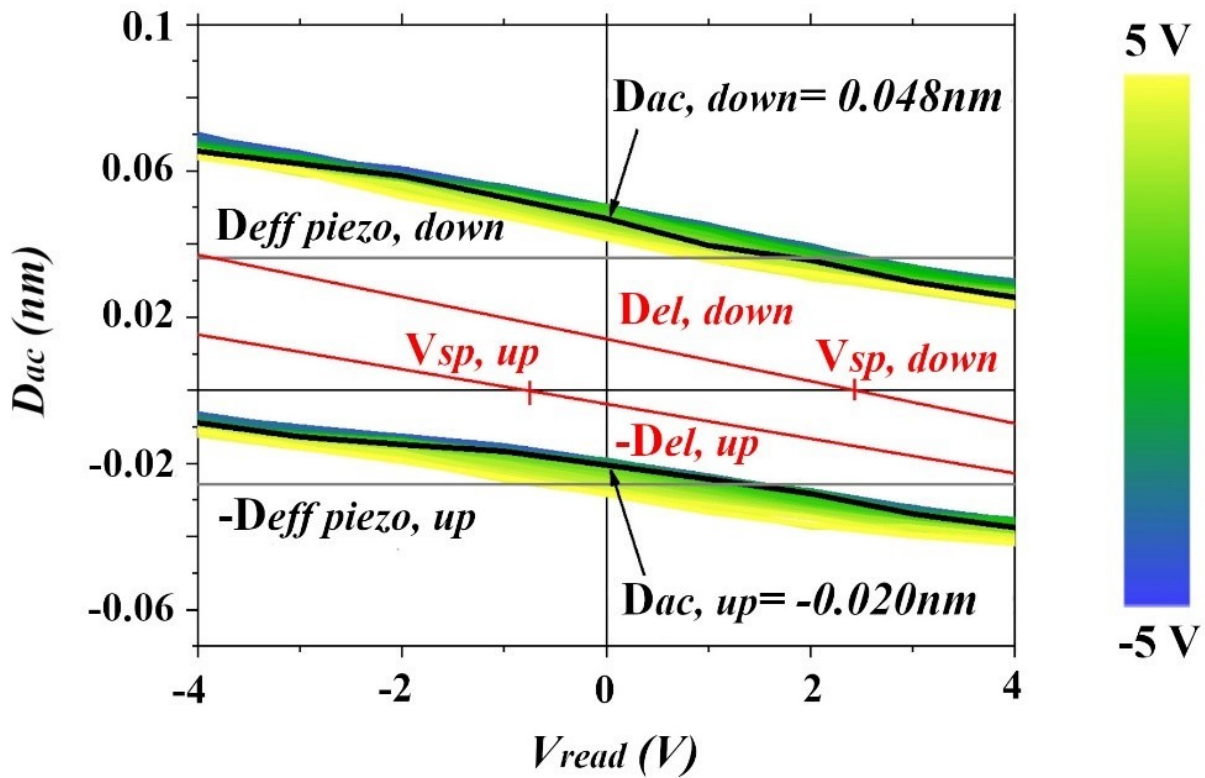


Figure 5.12: cKPFM results on BaTiO_3 . Tip displacement as a function of V_{read} for a range of V_{write} applied, for both up and down domains. Colour scale refers to V_{write} . The expected electromechanical (D_{eff}) response and electrostatic (D_{el}) contributions to the total signal are denoted with grey and red respectively.

Figure 5.12 shows the displacement of the tip for a range of V_{read} (-4 V to 4 V), while V_{write} is being applied before each measurement. The range of V_{write} is from -5V to 5V. The response for $V_{write} = 0$ is shown with black line. The results presented in this figure are for two different pixels of the image, each one corresponding to opposite domain (up and down). The magnitude of displacement for each domain has been calculated for $V_{write} = V_{read} = 0$. The corresponding map of cKPFM is shown in **Figure 5.13.a**. What is interesting is that up and down domains exhibit inequality not only on the magnitude of displacement, but also at the sign of displacement. For up domains $D_{ac} = -0.020$ nm while for down domains $D_{ac} = 0.048$ nm. **Figure 5.13.b** shows the behaviour of each domain over a range of V_{read} but for $V_{write} = 0$, showing that despite the minor dispersion, the slope is homogeneous. The same information can be extracted from the slope map, for $V_{write} = 0$ (**Figure 5.13.c**). Finally, the plot of the displacement values (D_{ac}) for $V_{write} = 0$ as a function of the slope behave in a linear way (**Figure 5.13.d**). This behaviour can

be described by the following equation:

$$D_{ac}|_0 = d_{eff}V_{ac} - m_iV_{surf} \quad (5.11)$$

where m_i represents the slope, and V_{surf} is the contact potential difference between the tip and the sample measured from classical KPFM measurements. For the presented cKPFM measurements, $V_{ac} = 2V$. Based on **Equation 5.11**, the effective coefficient, as well as the surface potential for both domains, can be calculated. The results are presented in **Table 5.8**.

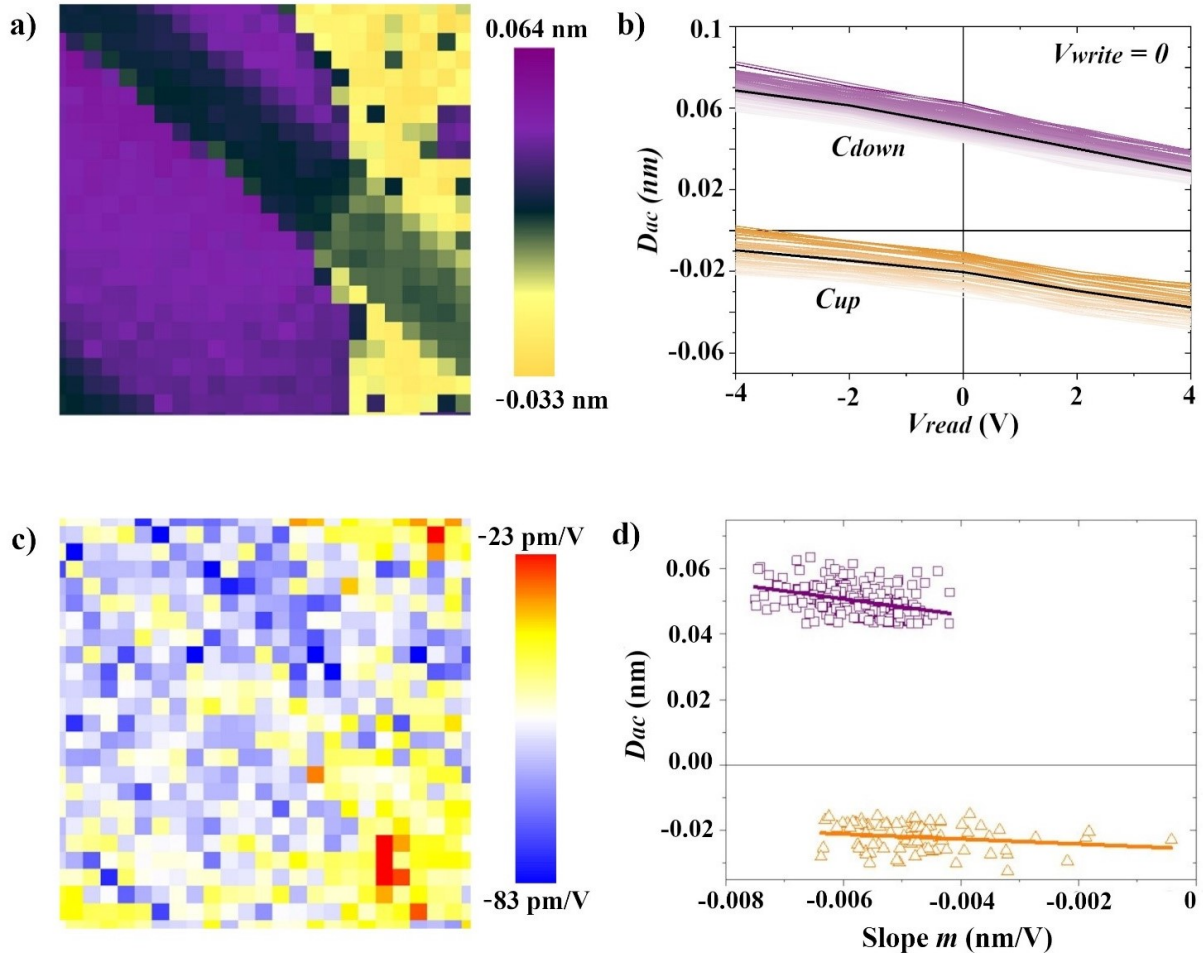


Figure 5.13: a) cKPFM map of $BaTiO_3$ for $V_{read} = V_{write} = 0$, from which the tip displacement (D_{ac}) for each domain (c up and c down) can be calculated. The resolution of the image is 25×25 pixels. b) D_{ac} as a function of V_{read} for $V_{write} = 0V$, for c up and c down domains showing a minor dispersion. c) Map of the slopes (m) calculated as the derivative of D_{ac}/V_{read} for $V_{write} = 0V$. d) Correlation of D_{ac} and the corresponding slope for each point.

Domains	D_{ac}	d_{eff}	V_{surf}
c down	0.048nm	18.1pm/V	2.43V
c up	-0.020nm	-12.85pm/V	0.76V

Table 5.8: Tip displacement (D_{ac}), effective coefficient (d_{eff}) and surface potential (V_{surf}) for BaTiO₃ single crystal as calculated from KPFM and cKPFM experiments.

5.4.2 Calculation of the piezoelectric coefficient of BaTiO₃ Single Crystal

The relative change of the effective polarization due to the flexoelectric coupling to the ferroelectric domains observed in CR-AFM should also induce a change in the values of the amplitude of the BE-PFM measurements, as a decrease (increase) of the total polarization for the c_{up} (c_{down}) domains. This will turn into a change of the effective piezoelectric coefficient, which is proportional to the polarization: one should expect a lower amplitude for the c_{up} domains as compared to c_{down} domains ($d_{up} \neq d_{down}$), as observed in the centroids for the corresponding areas shown in **Figure 5.6**. The asymmetry in the mechanical response should then be also observed in the obtained d_{eff} values. Following the same argument as before, the quantification of the piezoelectric coefficient can be achieved using the analysis of cKPFM results that are presented above. Considering that the flexocoupling coefficient of BaTiO₃ is positive (see **Section 3.4** for details), then the induced flexoelectric polarization is parallel with the induced piezoelectric polarization for c domains polarized down, and antiparallel for c up domains. Then:

$$d_{eff,up} = -d_{piezo} + d_{flexo} \quad (5.12)$$

$$d_{eff,down} = d_{piezo} + d_{flexo} \quad (5.13)$$

The experimental values of d_{eff} were calculated for both domains from the linear fit of **Figure 5.13.d** and are shown in **Table 5.8**. Thus, based on these values and combining **Equations 5.12** and **5.13**, we obtain a piezoelectric coefficient of $d_{piezo} = 15.47$ pm/V and $d_{flexo} = 2.62$ pm/V for the BaTiO₃ single crystal.

5.5 Decoupling of mechanical, electrostatic and piezoelectric properties from electromechanical responses at the nanoscale

In this Chapter, I have demonstrated that resonant PFM measurements depict not only the electromechanical properties of ferroelectric materials but also their mechanical properties, by showing that contact resonance frequency of mechanical (CR-AFM) and electromechanical (PFM) measurements behaves in a similar way. While the contrast pattern of contact resonance frequency response is the same for both measurements and depends clearly on the sign of ferroelectric polarization of the material, the absolute values differ between CR-AFM and PFM. In case of mechanical measurements, shifts in contact resonance frequency can only be attributed to changes of the mechanical response of the material, which have been evaluated to be $\sim \pm 4\%$ of the nominal Young's modulus under the flexoelectric fields created by tip induced mechanical strain gradients. In electromechanical measurements on the other hand, changes in contact resonance frequency can also be caused by electrostatic forces arising between the tip and the sample, leading to an extra term on the tip-sample coupling. However, they embrace the same information about mechanical properties.

These changes in contact resonance frequency of PFM are also accompanied with differences in the corresponding PFM amplitude. While traditionally assigned to tip-sample electrostatic coupling or artifacts, here we have demonstrated that indeed, they are further evidence of the flexoelectric tip-induced effect, in this case with a clear impact on the total electromechanical response. Here, cKPFM analysis was used to decipher the pure piezoelectric response of the sample. Electrostatic contributions on PFM signal make the quantification of mechanical properties through electromechanical measurements complex. However, having well established the mechanical response of ferroelectric materials, based on CR-AFM measurements and widely discussed in **Chapter 3**, and since contact resonance frequency response in CR-AFM and PFM are analogous, as demonstrated in this chapter, we are able to successfully decouple mechanical, flexoelectric, piezoelectric and electrostatic properties of ferroelectric materials from electromechanical measurements at the nanoscale.

These results have a wide impact in the field of nanoferroics, since we have demonstrated here that it is not possible to tackle a rigorous quantification of the nanoscale piezoresponse without considering the global impact of flexoelectricity. In this sense, resonance-based PFM measurements (either DART or preferably Band Excitation) show a clear advantage as compared to single frequency PFM measurements since they singularly capture the influence of mechanical response, which can be depicted separately by studying the contact resonance frequency response.

References

- [1] S. Jesse, S. V. Kalinin. *Band excitation in scanning probe microscopy: Sines of change*, J. Phys. D. Appl. Phys. 44(46) (2011).
- [2] S.M. Yang, L. Mazet, M.B. Okatan, S. Jesse, G. Niu, T. Schroeder, S. Schamm-Chardon, C. Dubourdieu, A.P. Baddorf, S. V. Kalinin. *Decoupling indirect topographic cross-talk in band excitation piezoresponse force microscopy imaging and spectroscopy*, Appl. Phys. Lett. 108(25) (2016).
- [3] F. Pedregosa FABIANPEDREGOSA, V. Michel, O. Grisel OLIVIERGRISEL, M. Blondel, P. Prettenhofer, R. Weiss, J. Vanderplas, D. Cournapeau, F. Pedregosa, G. Varoquaux, A. Gramfort, B. Thirion, O. Grisel, V. Dubourg, A. Passos, M. Brucher, M. Perrot and Édouard Duchesnay. *Scikit-learn: Machine Learning in Python Gaël Varoquaux Bertrand Thirion Vincent Dubourg Alexandre Passos PEDREGOSA, VAROQUAUX, GRAMFORT ET AL. Matthieu Perrot*, J. Mach. Learn. Res. 12 (2011).
- [4] J.A. Hartigan, M.A. Wong. *Algorithm AS 136: A K-Means Clustering Algorithm*, Source J. R. Stat. Soc. Ser. C (Applied Stat. 28(1) (1979).
- [5] J. MacQueen. *Some Methods for Classification and Analysis of MultiVariate Observations*, University of California Press.
- [6] C. Yuan, H. Yang. *Research on K-Value Selection Method of K-Means Clustering Algorithm*, J 2019, Vol. 2, Pages 226-235 2(2) (2019).
- [7] H.B. Zhou, J.T. Gao. *Automatic Method for Determining Cluster Number Based on Silhouette Coefficient*, Adv. Mater. Res. 951 (2014).
- [8] G. Liu, S. Zhang, W. Jiang, W. Cao. *Losses in ferroelectric materials* (2015).
- [9] U. Rabe, S. Amelio, M. Kopycinska, S. Hirsekorn, M. Kempf, M. Göken, W. Arnold. *Imaging and measurement of local mechanical material properties by atomic force acoustic microscopy*, Surf. Interface Anal. 33(2) (2002).
- [10] U. Rabe, S. Amelio, E. Kester, V. Scherer, S. Hirsekorn, W. Arnold. *Quantitative*

determination of contact stiffness using atomic force acoustic microscopy, Ultrasonics 38(1–8) (2000).

[11] D.C. Hurley. *Contact Resonance Force Microscopy Techniques for Nanomechanical Measurements*, Applied Scanning Probe Methods XI: Scanning Probe Microscopy Techniques, Springer Berlin Heidelberg, Berlin, Heidelberg, 2009.

[12] B. Nina, J. Stephen, Y. Pu, C. Ben, V.K. Sergei, T. Alexander. *Quantification of surface displacements and electromechanical phenomena via dynamic atomic force microscopy*, Nanotechnology 27(42) (2016).

[13] W.C. Oliver, F.R. Brotzen. *On the generality of the relationship among contact stiffness, contact area, and elastic modulus during indentation*, J. Mater. Res. 7(3) (1992).

[14] J.M.J. Den Toonder, J.A.W. Van Dommelen, F.P.T. Baaijens. *Relation between single crystal elasticity and the effective elastic behaviour of polycrystalline materials: Theory, measurement and computation*, Model. Simul. Mater. Sci. Eng. 7(6) (1999).

[15] C. Stefani, L. Ponet, K. Shapovalov, P. Chen, E. Langenberg, D.G. Schlom, S. Artyukhin, M. Stengel, N. Domingo, G. Catalan. *Mechanical Softness of Ferroelectric 180 ° Domain Walls*, Phys. Rev. X 10(4) (2020).

[16] N. Balke, P. Maksymovych, S. Jesse, A. Herklotz, A. Tselev, C.B. Eom, I.I. Kravchenko, P. Yu, S. V. Kalinin. *Differentiating Ferroelectric and Nonferroelectric Electromechanical Effects with Scanning Probe Microscopy*, ACS Nano 9(6) (2015).

[17] B. Nina, J. Stephen, C. Ben, M.B. Okatan, I.K. Ivan, V.K. Sergei, T. Alexander "Quantification of in-contact probe-sample electrostatic forces with dynamic atomic force microscopy", Nanotechnology 28(6) (2017).

CHAPTER 6

Conclusions

This thesis studies the mechanical and electromechanical properties of ferroelectric materials at the nanoscale using AFM techniques. The goal of the present thesis was the identification and quantification of mechanical properties of both ferroelectric domain and domain walls and the investigation of their role to the total electromechanical response of the material. The main findings and conclusions of this research are summarized here.

Oppositely-polarized ferroelectric domains have different nanomechanical response with domains polarized-up to be softer than domains polarized-down. This asymmetry in mechanical properties of ferroelectrics under inhomogeneous deformation arises from the coupling of piezoelectricity and flexoelectricity. Strain gradients created by an AFM tip in contact with a ferroelectric material induce flexoelectric fields that interact asymmetrically with domains of opposite polarization, and the asymmetry of this interaction enables a mechanical reading of ferroelectric polarization. I have shown that CR-AFM is an optimal technique to exploit this induced asymmetry and achieve mechanical reading of ferroelectric polarity in a non-destructive way. The results in different materials, from bulk single crystals (LiNbO₃ and BaTiO₃) to epitaxial thin films (BiFeO₃ and PbTiO₃), show that the effect is universal: mechanical contact resonance frequency, as measured by CR-AFM, is always higher for up-pointing domains than the opposite ones.

Another interesting and non-trivial conclusion of this study is that, despite the different composition, elemental charge, or even crystal orientation of the perovskite materials under study (some where 001-oriented, others 111-oriented), the effective flexoelectric coefficient seems to always have the same sign. Considering that the direct measurement

of flexoelectricity in polar materials is inherently complicated, this information is already valuable. In addition, different single crystals have different dielectric constants and thus very different expected flexoelectric coefficients. The results show, as expected, that the mechanical contrast between oppositely-polarized domains is enhanced for materials with larger dielectric constant.

In addition, mechanical reading of ferroelectric polarization is based on tip-induced strain gradients which, by their very nature, relax within a small distance. That means that the relative volume affected by strain gradients (and consequently flexoelectric fields) is increasing when material's thickness is decreasing. Indeed, the results prove that the interaction between piezoelectric and flexoelectric polarization and the resulted mechanical contrast is enhanced in thinner materials. On another practical issue, I have also demonstrated that the mechanical reading of ferroelectric polarization by CR-AFM is influenced by cantilever's stiffness (the stiffer the cantilever, the more sensitive it is to the mechanical asymmetry of the sample). The work contained in this thesis thus comprises both the fundamental and the practical aspects that must be taken into consideration when investigating the nanomechanics of ferroelectrics experimentally.

Moving onto domain walls, I have studied the out-of-plane nano-mechanical response of ferroelectric 180° domain walls using CR-AFM. I show that domain walls always appear mechanically distinct -softer- than the surrounding domains. Studying a range of materials' compositions and morphologies, from bulk materials to thin films, it is shown that mechanical softness of domain walls is a general phenomenon. Taking a step further, mechanical softness of domain walls has been quantified. Describing CR-AFM mode by the appropriate mathematical equations, I was able to quantify the difference in effective Young's modulus between the ferroelectric domains and the domain walls. The origin of domain walls' softness was addressed in a theoretical framework (elaborated by collaborators) which shows that there can be at least two contributing mechanisms: domain wall sliding due to a "strain dip" at the wall and contrast in depolarization contributions between the polar domains and the non-polar domain walls.

Besides its fundamental interest, this discovery may have practical ramifications both for the mechanics of ferroelectrics and for their functionality. For example, the mechanical

detection of ferroelectric domain walls means that they can be probed in a voltage-free manner, which may be useful in the case of conducting ferroelectrics. Also, the mechanical contrast of ferroelectric domain walls is bigger than the contrast between domains so a possible application of domain walls' softness could be a more efficient "mechanical reading" of ferroelectric bits. In general, this work establishes that domain walls are distinct not only functionally but also mechanically, and this mechanical singularity must be incorporated in domain wall physics.

Mechanical unevenness in ferroelectrics arise from tip-induced strain gradients. These gradients though are present not only in mechanical measurements (CR-AFM) but also in the electromechanical ones (PFM). By comparing the contact resonance frequency of Band Excitation CR-AFM and PFM, I show that the signal behaves in a similar way in both cases, and electromechanical (PFM) measurements indeed already contain all the information about mechanical properties of ferroelectrics. Of course, shifts in CR-AFM frequency originate from changes in mechanical response of the sample while shifts in PFM contact resonance frequency are also affected by electrostatics and piezoelectricity, making the disentangling of different contributions and quantification of mechanical properties in electromechanical measurements a complex issue. Using cKPFM to decipher the pure piezoelectric response of the material and having the mechanical response of ferroelectrics well established from CR-AFM, I was able to distinguish contributions of mechanical and electromechanical properties of ferroelectrics in PFM measurements. Finally, it was shown that tip-induced flexoelectric effect is responsible not only for changes in PFM contact resonance frequency but also for changes in PFM amplitude, demonstrating that flexoelectricity has an overall impact in piezoresponse at the nanoscale and, by enlarge, in all the standard microscopy techniques used to characterize ferroelectrics.

To conclude, this thesis shows that contrast in contact resonance frequency of electromechanical measurements depends on the magnitude and sign of ferroelectric polarization and consequently resonance-based PFM measurements can be used to detect the mechanical response of ferroelectric domains and domain walls at the nanoscale.

APPENDIX A

Quantification of tip-sample mechanical coupling

CR-AFM is a suitable technique for mapping elastic properties of materials with high resolution. However, its big asset is the quantification of experimental measurements. Analytical formulas can describe in good approximation the vibration of the cantilever in contact with the sample, resulting in the quantification of elastic constants of the material.

A.1 General equation of motion

Most commonly used cantilevers have rectangular shape or are rectangular with a triangular end but can be approximately considered as rectangularly shaped (**Figure 2.2** shows a SEM image of cantilevers used for the experiments of this thesis). Considering that the length of the cantilever is bigger than its width, then the cantilever can be described as an elastic beam. The vibrational modes of cantilevers with different shapes have been calculated numerically or with analytical approximations [1–3]. In case of rectangular shaped cantilever, the equation of motion for flexural vibrations is [4]:

$$EI \frac{\partial^4 y}{\partial x^4} + \eta_{air} \rho A \frac{\partial y}{\partial t} + \rho A \frac{\partial^2 y}{\partial t^2} = 0 \quad (\text{A.1})$$

The x axis is parallel to cantilever's length, while y axis is perpendicular to it. E is cantilever's Young's modulus and I is the area moment of inertia. I can be calculated by the geometrical characteristics of the cantilever as $I = wb^3/12$, where w and b are width and thickness of cantilever respectively. **Figure A.1** shows a sketch of cantilever for better understanding of its geometrical parameters. Term η_{air} expresses the dissipation caused

by air, ρ is mass density and A the area of cross section.

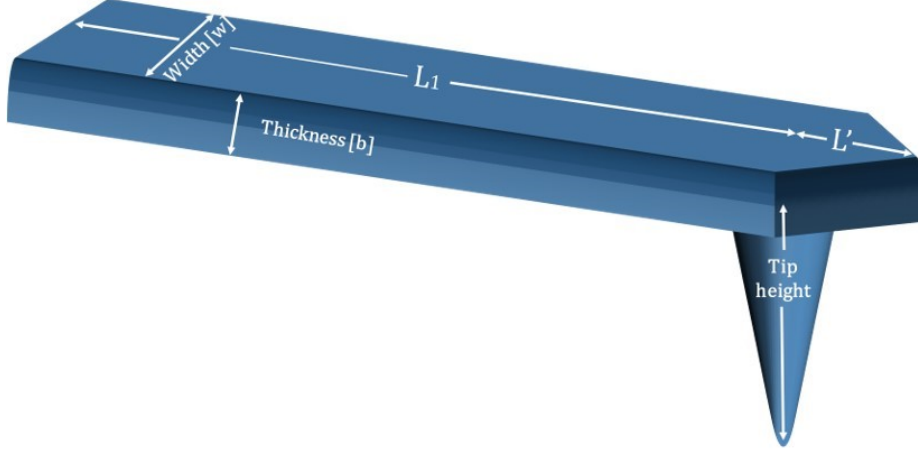


Figure A.1: Sketch of rectangular cantilever with triangularly shaped end.

$y(x)$ describes the deflection of cantilever at any point x and consequently its derivative $(\partial y/\partial x)$ is the slope of the beam. Accordingly, $EI \frac{\partial^2 y}{\partial x^2}$ is torsional moment and $EI \frac{\partial^3 y}{\partial x^3}$ is shear force.

Equation A.1 has an harmonic solution for every specific value of angular frequency ($\omega = 2\pi f$), and in this case, time can be isolated from space, meaning that $y(x, t)$ can be written as:

$$y(x, t) = y(x)y(t) = (a_1 e^{ax} + a_2 e^{-ax} + a_3 e^{iax} + a_4 e^{-iax}) e^{i\omega t} \quad (\text{A.2})$$

Then, $y(x)$ describes the motion of the cantilever at any point x for a value of ω . The general solution of $y(x)$ is:

$$\begin{aligned} y(x) = & A_1(\cos ax + \cosh ax) + A_2(\cos ax - \cosh ax) \\ & + A_3(\sin ax + \sinh ax) + A_4(\sin ax - \sinh ax) \end{aligned} \quad (\text{A.3})$$

where $a_{1, \dots, 4}$ and $A_{1, \dots, 4}$ are constants. $A_{1, \dots, 4}$ can be found by solving **Equation A.3** with proper boundary conditions.

Equation A.1 shows that elastic beam behaves as a wave and by substituting **Equation A.2** to **A.1** we get:

$$EIa^4 + i\eta_{air}\rho A\omega - \rho A\omega^2 = 0 \quad (\text{A.4})$$

Where a is a complex wave number describing the motion of elastic beam and equals to:

$$a_{\pm} = \pm \sqrt[4]{\frac{\rho A}{EI}(\omega^2 \mp i\eta_{air}\rho A\omega)} \quad (\text{A.5})$$

Damping constant expressing dissipation due to air (η_{air}) can be neglected in our case, resulting in the dispersion equation that correlates the resonance frequency (f) with the wave number a for every point x of the cantilever (taking into account that the length of the cantilever from the clamped end till the point of the tip is L):

$$f = \frac{(aL)^2}{2\pi} \frac{1}{L^2} \sqrt{\frac{EI}{\rho A}} \quad (\text{A.6})$$

Equation A.6 is formed considering the geometrical characteristics of the tip and its properties, such as mass density, Young's modulus and area of cross section. Although these characteristics can be provided by the manufacturers, there are often not accurate, introducing significant errors in the calculations. It is then preferable to use equations that contain magnitudes that can be experimentally calculated, such as the length of cantilever that can be measured by SEM. To do so, it is important to introduce calculation of quality factor (Q). The quality factor for different resonances is given by [5]:

$$Q = \frac{\omega_n}{\delta\omega} = \frac{\omega_n}{\eta_{air}} \quad (\text{A.7})$$

where n refers to mode number. The equation above shows that quality factor increases when mode number increases. Additionally, there are studies showing the correlation of resonance frequencies for different modes (from free oscillation to forced flexural vibration) and for different boundary conditions (cantilevers with one clamped end and one free end and cantilevers with clamped end and pinned end) [6]. Based on that, **Equation A.5** and **A.6** can be rewritten as:

$$\begin{aligned} a_{\pm}L &= \pm a_{1,free}L \sqrt[4]{\frac{\omega^2}{\omega_{1,free}^2} \mp i \frac{\eta_{air}\omega}{\omega_{1,free}^2}} \\ &\approx \pm 1.8751 \sqrt[4]{\left(\frac{f}{f_{1,free}}\right)^2 \mp i \frac{1}{Q_{1,free}} \frac{f}{f_{1,free}}} \end{aligned} \quad (\text{A.8})$$

$$\frac{f}{f_{1,free}} = \frac{(aL)^2}{(a_{1,free}L)^2} \quad (\text{A.9})$$

Equation A.9 correlates the ratio of contact resonance frequency with the resonance frequency of cantilever with one free end at first vibration mode with the corresponding wave numbers. These wave numbers are included in **Equation A.3** that describes the motion of the cantilever, independently of time. Since values of contact resonance frequency are indeed the values obtained from CR-AFM experiments, the problem is reduced in finding the proper boundary conditions of general equation of motion (**Equation A.3**) that describe in best approximation the experimental parameters of CR-AFM mode set up.

A.2 Contact forces

Before discussing the boundary conditions describing the flexural vibrations of the cantilever, it is of high importance to describe the contact of the cantilever with sample's surface, as it strongly affects the dynamics of the end of the elastic beam.

In CR-AFM mode, the tip is in contact with the sample. Assuming that the amplitude of oscillation of the tip is very small, the forces between tip and sample can be represented with linear springs and dashpots and the problem can be solved in two dimensions. Additionally, in most AFMs, as the ones used in this thesis, the cantilever is not placed perpendicular to sample's surface but is tilted (in our case the tilting angle is 11°), introducing both normal and lateral forces. **Figure A.2** shows all forces describing the tip-sample contact. The normal and lateral forces are described by linear springs called contact stiffness (k^*) and lateral contact stiffness (k^*_{lat}) respectively, while damping, which can be neglected in the case of our experiments, is represented by dashpots (γ and γ_{lat}). Contact stiffness represents the forces between two bodies and can be calculated by contact mechanics [7–9].

Considering that both tip and sample are elastic anisotropic bodies then Hertzian mechanics can describe the contact between them [7]. The sample is represented as a flat surface while the tip is a sphere with radius R . Considering a constant normal force F_N ,

then the contact radius (a_c) formed between tip and sample is given by:

$$a_c = \sqrt[3]{3F_N R / 4E^*} \quad (\text{A.10})$$

where E^* is the effective Young's modulus, a characteristic magnitude of the contact between two bodies and can be calculated from the Young's modulus (E) and Poisson ratio (ν) of the sample and the tip, using the following equation:

$$\frac{1}{E^*} = \frac{1 - \nu_s^2}{E_s} + \frac{1 - \nu_{tip}^2}{E_{tip}} \quad (\text{A.11})$$

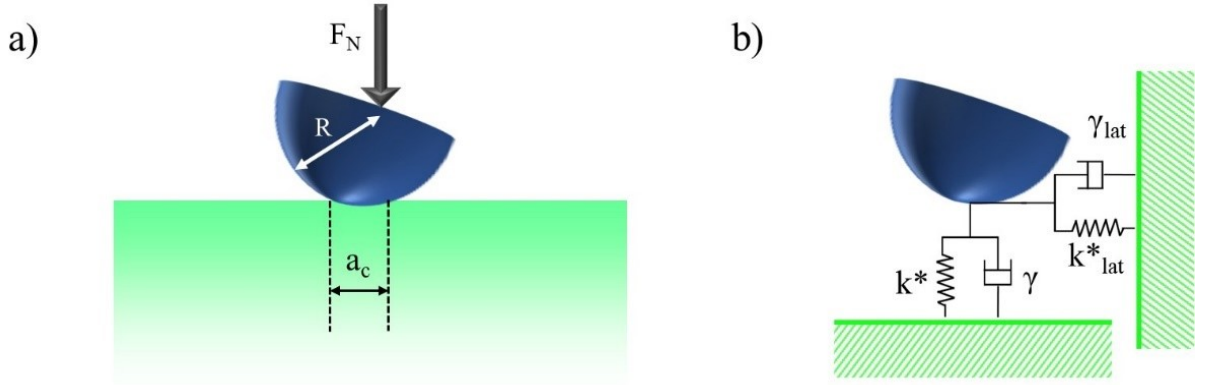


Figure A.2: Schematic representation of tilted tip in contact with sample. a) When the tip is in contact with the sample a static force F_N is applied to maintain good contact while a contact area a_c , smaller than the radius of the tip (R), is formed between the tip and the surface. b) The contact between tip and sample is described by normal and lateral linear springs and dashpots.

Regarding the contact stiffness (k^*), it depends on effective Young's modulus and the contact radius a_c and is given by the following equation [7]:

$$k^* = 2a_c E^* = \sqrt[3]{6E^{*2} R F_N} \quad (\text{A.12})$$

The approach till now is simplistic although approximations are in accordance with the experimental parameters. Before we proceed, there are two main issues that should be addressed at this point. Initially, it is proven experimentally that tips suffer from wearing and spherical shape is not always a realistic representation of tips after scanning in contact [10]. In that case tip can be represented as a flat punch. Nevertheless, the

first part of **Equation A.12** applies in any general case [11]. The second issue is related with the anisotropy of the sample. There are cases that sample is not isotropic, or it is macroscopically isotropic but in range of few nanometres, which is the lateral resolution of an AFM tip, can be anisotropic. Then it is described by two elastic constants and the elastic modulus of **Equation A.11** should be substituted by an indentation modulus (M) that can be calculated numerically [12]. Then **Equation A.11** becomes:

$$\frac{1}{E^*} = \frac{1}{M_s} + \frac{1}{M_{tip}} \quad (\text{A.13})$$

Contact stiffness (k^*) represents the contact in the plane vertical to sample's surface. Hence, tilting of cantilever in combination with flexural vibrations introduce lateral contact stiffness (k_{lat}^*). Lateral contact stiffness depends on effective shear stiffness G^* [7]:

$$k_{lat}^* = 8a_c G^* \quad (\text{A.14})$$

$$\frac{1}{G^*} = \frac{2 - \nu_s}{G_s} + \frac{2 - \nu_{tip}}{G_{tip}} \quad (\text{A.15})$$

where G_s and G_{tip} is shear modulus of sample and tip respectively.

Combining **Equations A.12** and **A.14** is shown that the ratio between contact stiffness and lateral contact stiffness does not depend on the applied normal force (F_N):

$$\frac{k_{lat}^*}{k^*} = \frac{8a_c G^*}{2a_c E^*} = \frac{4G^*}{E^*} \quad (\text{A.16})$$

To conclude, the contact between the tip and the cantilever can be described in good approximation by Hertzian contact mechanics. The contact is represented by a linear spring (contact stiffness k^*) while tilting of cantilever and changes of tip's shape due to wear are included in the mathematical formulas.

A.3 Characteristic equation

After having established the equation that describes the motion of cantilever in contact with sample (**Section A.1**) and have described the mechanics of the contact (**Section**

A.2), the next step is to properly introduce the experimental conditions of CR-AFM measurements as boundary conditions of the equation of motion (**Equation A.3**).

In CR-AFM mode, as used in the experiments presented in this thesis, the tip is in contact with the sample while the cantilever is mechanically excited at its base. If we consider the cantilever as shown in **Figure A.8**, then it can be separated in two sections. First section starts at its clamped end at $x=0$ and finishes at tip position ($x=L_1$) while the second section starts at the free end of the cantilever and ends at tip position ($x=L'$). Each section is described by the corresponding equation $y(x)$ and $y_2(x_2)$. Note that they have opposite directions only for making calculations more convenient. All following equations and conditions are based on the analysis previously described by several seminal works published by U. Rabe [5].

Since the cantilever is mechanically excited, we can consider that at the clamped end of cantilever the promoted vibration has a wave form and can be described as $u_c(t) = u_0 e^{i\omega t}$. Then at $x=0$, the equation of motion should be $y(0)=u_0$. However, the slope at this point should be zero and this is translated into $\partial y/\partial x = 0$. Contrariwise, at tip position ($x=L_1$), the torsional moment and shear forces are non-zero. This condition can be better described if we define a contact function $\varphi(\alpha)$ that contains both contact stiffness and contact damping:

$$\varphi(a) = 3 \frac{k^*}{k_{lever}} + i(aL_1)^2 p \quad (\text{A.17})$$

where k_{lever} is the spring constant of the cantilever and p a damping constant. In our case damping can be neglected ($p=0$). Accordingly, there is the lateral contact function $\varphi_{lat}(\alpha)$ where contact stiffness is substituted by lateral contact stiffness. The ratio between lateral and normal contact function is defined as:

$$c_p = \frac{\varphi_{lat}(a)}{\varphi(a)} \quad (\text{A.18})$$

For the sake of convenience, auxiliary functions T, X and U are defined to properly express

the boundary conditions [13]:

$$\begin{aligned}
 T(a) &= \frac{h^2}{L_1^3} \varphi(a) \sin^2 \theta + \frac{h^2}{L_1^3} \varphi_{lat}(a) \cos^2 \theta \\
 X(a) &= \frac{h^2}{L_1^3} \sin \theta \cos \theta [\varphi_{lat}(a) - \varphi(a)] \\
 U(a) &= \frac{1}{L_1^3} \varphi(a) \cos^2 \theta + \frac{1}{L_1^3} \varphi_{lat}(a) \sin^2 \theta
 \end{aligned} \tag{A.19}$$

where θ is the tilting angle of the cantilever and h is the tip height. Then the boundary conditions of general equation of cantilever's motion for CR-AFM mode can be expressed as:

$$x = 0 : \begin{cases} y = u_0 \\ \frac{\partial y}{\partial x} = 0 \end{cases} \tag{A.20}$$

Substitution of these boundary conditions into general equation of motion (**Equation A.3**) will conclude into a characteristic equation that describes the motion of the cantilever at any point for a given resonance frequency. The calculations and final equations are presented by Rabe [5] and the solution of this characteristic equation is a complex wave number.

Although this analysis is helpful to comprehend how experimental parameters are mathematically expressed in good approximation and sets the base for the following analysis, the solution of the final characteristic equation demands complex calculations that do not allow a direct quantification of experimental results.

A simpler approach is an analytical expression that describes the normalized contact stiffness k^*/k_{lever} as a function of contact resonance frequency [14]:

$$\frac{k^*}{k_{lever}} = 3 \frac{(c_n \sqrt{f_n})^3 cch^+(c_n \sqrt{f_n})}{cch^-(c_n \sqrt{f_n} L_1/L) mix^-(c_n \sqrt{f_n} L'/L) - cch^+(c_n \sqrt{f_n} L'/L) mix^-(c_n \sqrt{f_n} L_1/L)} \tag{A.21}$$

where f_n refers to resonance frequencies of different modes and c_n is a coefficient that can be defined by rewriting the dispersion equation (**Equation A.9**): stiffness k^*/k_{lever} as

a function of contact resonance frequency [14]:

$$aL = \frac{a_{n,free}L}{\sqrt{f_{n,free}}} \sqrt{f_{cont}} = c_n \sqrt{f_{cont}} \quad (\text{A.22})$$

and finally, the abbreviations are:

$$\begin{aligned} cch^\pm(x) &= 1 \pm \cos(x) \cosh(x) \\ mix^\pm(x) &= \sin(x) \cosh(x) \pm \cos(x) \sinh(x) \end{aligned} \quad (\text{A.23})$$

Equation A.21 depends on the geometrical characteristics of the tip (L_1 , L' , k_{lever}), the experimentally measured contact resonance frequency but also the wave number and the contact stiffness (k^*), which are both unknown. It is worth mentioning here that spring constant of the cantilever (k_{lever}) can be calculated by two ways: by its geometrical characteristics since $k_{lever} = Eb^3w/4L^3$ or experimentally, by measuring force-displacement curves. To be able to calculate contact stiffness, one more equation is needed. In case of small damping, normalized contact stiffness is proportional to contact function:

$$\varphi(a) \approx \frac{k^*}{k_{lever}} \quad (\text{A.24})$$

If lateral forces are included, then contact function can be calculated solving this quadratic equation [5]:

$$\varphi(a) = g \pm \sqrt{g^2 - \frac{L_1^2 L_1^4 S_4}{h^2 S_0 c_p}} \quad (\text{A.25})$$

$$\begin{aligned} &L_1 S_1 (\cos^2 \theta + c_p \sin^2 \theta) + L_1^2 S_2 \frac{h}{L_1} (c_p - 1) \sin \theta \cos \theta \\ g &= \frac{+L_1^3 S_3 h^2 / L_1^2 (\sin^2 \theta + c_p \cos^2 \theta)}{2S_0 h^2 / (L_1^2) c_p} \end{aligned} \quad (\text{A.26})$$

S_i are the coefficients of the characteristic equation [5]:

$$\begin{aligned}
 S_0 &= (1 - \cos aL_1 \cosh aL_1)(1 + \cos aL' \cosh aL') \\
 S_1 &= a[-(1 - \cos aL_1 \cosh aL_1)(\sin aL' \cosh aL' - \sinh aL' \cos aL') \\
 &\quad + (1 + \cos aL' \cosh aL')(\sin aL_1 \cosh aL_1 - \sinh aL_1 \cos aL_1)] \\
 S_2 &= 2a^2[\sin aL_1 \sinh aL_1(1 + \cos aL' \cosh aL') \\
 &\quad + \sin aL' \sinh aL'(1 - \cos aL_1 \cosh aL_1)] \\
 S_3 &= a^3[(\sin aL_1 \cosh aL_1 + \sinh aL_1 \cos aL_1)(1 + \cos aL' \cosh aL') \\
 &\quad - (\sin aL' \cosh aL' + \sinh aL' \cos aL')(1 - \cos aL_1 \cosh aL_1)] \\
 S_4 &= 2a^4(1 + \cos aL \cosh aL)
 \end{aligned} \tag{A.27}$$

Equation A.21 combined with **Equation A.25** can be solved to calculate the values of contact stiffness k^* for every experimentally measured value of contact resonance frequency in CR-AFM experiments. Contact stiffness is correlated with effective Young's modulus through **Equation A.12**. In the last equation the unknowns are both Young's modulus of the tip and the sample. In the case where the Young's modulus of the tip is known, then the combination of the above-mentioned equations can be used to extract differences in elastic constants of the material based on shifts in contact resonance frequency. If tip's Young's modulus is unknown, then a reference sample is needed to calibrate the tip, i.e., to calculate its elastic constants. In that case, **Equation A.12** will be solved with E_t as unknown, on a sample with known Young's modulus, and then the same equation will be solved once again for a different area of the sample, or for a different sample, where Young's modulus of the tip is now known and Young's modulus of the sample is being calculated. Despite that Young's modulus of a tip can be found in literature based on its material and consistence, these values may deviate a lot from the actual Young's modulus of the tip. This is the reason why a reference sample or area is preferred in order to calculate tip's Young's modulus, as will be shown in the following chapters of this thesis.

References

- [1] J.A. Turner, J.S. Wiehn "Sensitivity of flexural and torsional vibration modes of atomic force microscope cantilevers to surface stiffness variations ", *Nanotechnology* 12 (2001).
- [2] R.W. Stark, T. Drobek, W.M. Heckl "Thermomechanical noise of a free v-shaped cantilever for atomic-force microscopy", *Ultramicroscopy* 86(1-2) (2001).
- [3] D.C. Hurley, K. Shen, N.M. Jennett, J.A. Turner "Atomic force acoustic microscopy methods to determine thin-film elastic properties", *J. Appl. Phys.* 94(4) (2003).
- [4] W. Weaver, S. Timoshenko, D.H. (Donovan H. Young *Vibration problems in engineering*, Wiley, 1990.
- [5] U. Rabe "Atomic Force Acoustic Microscopy", in: B. Bhushan, H. Fuchs (Eds.), *Applied Scanning Probe Methods II: Scanning Probe Microscopy Techniques*, Springer Berlin Heidelberg, Berlin, Heidelberg, 2006, pp. .
- [6] U. Rabe, K. Janser, W. Arnold "Vibrations of free and surface-coupled atomic force microscope cantilevers: Theory and experiment", *Rev. Sci. Instrum.* 67(9) (1996).
- [7] K.L. Johnson *Contact Mechanics*, Cambridge University Press, 1985.
- [8] O. Piétrement, M. Troyon "General Equations Describing Elastic Indentation Depth and Normal Contact Stiffness versus Load", *J. Colloid Interface Sci.* 226(1) (2000). [9] J.A. TURNER *ULTRASONIC STUDIES OF THE FUNDAMENTAL MECHANISMS OF RECRYSTALLIZATION AND SINTERING OF METALS*, Argonne, IL, 2005.
- [10] S. Amelio, A. V. Goldade, U. Rabe, V. Scherer, B. Bhushan, W. Arnold "Measurements of elastic properties of ultra-thin diamond-like carbon coatings using atomic force acoustic microscopy", *Thin Solid Films* 392(1) (2001).
- [11] W.C. Oliver, F.R. Brotzen "On the generality of the relationship among contact stiffness, contact area, and elastic modulus during indentation", *J. Mater. Res.* 1992 73 7(3) (2011).
- [12] U. Rabe, S. Amelio, M. Kopycinska, S. Hirsekorn, M. Kempf, M. Göken, W. Arnold "Imaging and measurement of local mechanical material properties by atomic force acoustic microscopy", *Surf. Interface Anal.* 33(2) (2002).
- [13] U. Rabe, J.A. Turner, W. Arnold "Analysis of the high-frequency response of atomic

force microscope cantilevers”, *Artic. Appl. Phys. A* (1998).

[14] E. Kester, U. Rabe, L. Presmanes, P. Tailhades, W. Arnold ”Measurement of Young’s modulus of nanocrystalline ferrites with spinel structures by atomic force acoustic microscopy”, *J. Phys. Chem. Solids* 61(8) (2000).

APPENDIX B

Influence of cantilever stiffness on mechanical reading

In **Chapter 3** mechanical properties of out-of-plane polarized ferroelectric domains were investigated, from the scope of fundamental physics. Applying a force with an AFM tip over a ferroelectric domain induces piezoelectric and flexoelectric fields. The coupling of both can lead to an asymmetry in mechanical properties between opposite polarized domains, based on the sign of polarization. The size reduction of the sample can naturally enhance this mechanical contrast, and the overall mechanical behavior is probed by the CR-AFM technique.

However, the measured signal in CR-AFM embeds cantilever's geometrical features which critically determine the total mechanical response of the whole cantilever – sample system. As described in **Section 2.4**, in CR-AFM mode the tip is in contact with the sample and the system is vibrated mechanically. The resonance frequency of the system is being probed, considering that the mechanical and geometrical characteristics of the tip remain invariable during the imaging process, so that changes in resonance frequencies are due to changes of the mechanical properties of the sample. However, geometrical characteristics of the cantilever do affect the total mechanical response. In this appendix is reported the efficiency of mechanical reading of ferroelectric polarization using different types of cantilevers as a function of their mechanical characteristics.

In a simple model, a cantilever in strong coupling with a stiff material, can be described as two springs in series. The cantilever can be approached using an Euler-Bernoulli elastic beam model and the tip-sample mechanical contact is represented by an effective spring k^* connected in series with a dashpot to account for damping [1–6]. The analytical

description of the system can be found in **Appendix A**. This approach discloses the effect of cantilever’s mechanical stiffness related to the sample’s stiffness. First of all, the magnitude of the cantilever’s stiffness has to be appropriately selected as a function of the Young Modulus of the sample to be measured. CR-AFM technique is in general, more appropriate for samples with elastic modulus over 50 GPa. For softer materials, elastic properties are better measured using AM-FM viscoelastic mapping, which, based on a dynamic AFM multifrequency mode, it is able to determine the surface stiffness of materials with elastic modulus of some GPa. Nevertheless, in CR-AFM mode, stiff materials, with elastic constants in the range of hundreds GPa, require evenly stiff cantilevers (with $k_{lever} \geq 20$ N/m). Otherwise, the measured contact resonance frequency will be either completely dominated by either the cantilever or the sample and the technique will not be able to track any changes. Once the cantilever is appropriately selected and considering that cantilever exhibits a constant stiffness during the measurement, the contrast in measured contact resonance frequencies can be taken as indicative of changes on sample’s stiffness. In the performed measurements, it is considered that the geometrical characteristics of the tip do not vary during imaging –at least definitely not during the course of a single line or a single image.

To prove the dependence of sensitivity of mechanical reading of ferroelectric polarization on the cantilever’s stiffness, CR-AFM measurements were performed with different AFM tips. Tips were chosen with approximate same length to facilitate similar mechanical bending shapes, but different stiffness arising from slightly different width and thickness. In this sense, we used two types of cantilevers, as presented in **Table B.1**.

Type	Product Name	L (μm)	b (μm)	w (μm)	k_{lever} (N/m)	f (kHz)	Coating
A	PPP-EFM	225	3	28	~ 2	75	PtIr
B	PPP-NCL	225	7	38	~ 45	170	no

Table B.1: *Types of cantilevers and their geometrical characteristics*

The experiments were performed in two different materials: a periodically poled LiNbO₃ (PPLN) single crystal and a PbTiO₃ thin film of 50 nm thickness on SrTiO₃ substrate.

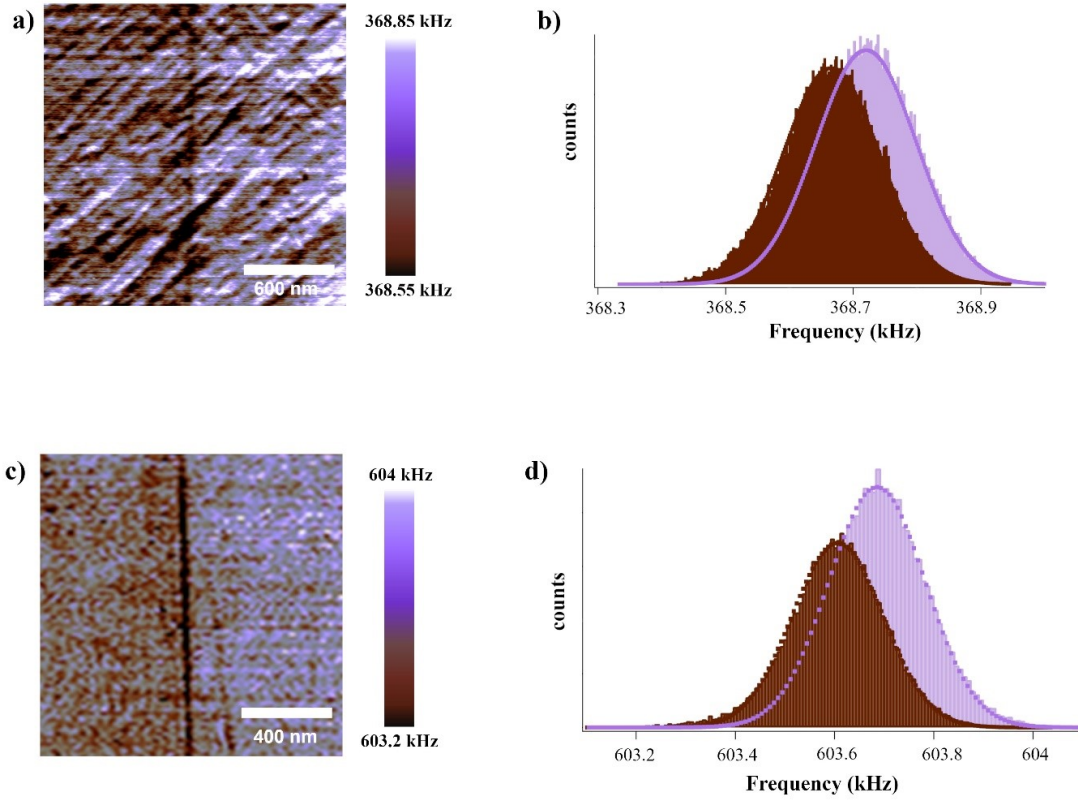


Figure B.1: CRF image of PPLN crystal, as measured by a) a soft AFM tip with elastic constant of ~ 2 N/m (PPP-EFM, Nanosensors), and c) a stiff AFM tip with elastic constant of ~ 45 N/m (PPP-NCL, Nanosensors), under the same applied force (900 nN). The corresponding histograms demonstrate shift in resonance frequency of opposite polarized domains of 50 Hz for soft tips (b) and 250 Hz for a stiff tip (d).

Figure B.1.a shows the CR-AFM image of opposite polarized domains on PPLN crystal, as measured using a soft tip – type A. Accordingly, **Figure B.1.c** shows the same area as measured by a stiff tip – type B. Through histograms of each image (**Figure B.1.b** and **B.1.d** respectively) the difference in resonance frequency values between up and down domains can be calculated. For soft tip, the shift of around 50 Hz can hardly be distinguished, but it rises to 250 Hz for stiffer tips.

On the other hand, the same experiments were performed for PbTiO_3 thin film. The CR-AFM measurement with soft tips (type A) of two oppositely polarized domains is shown in **Figure B.2.a**, and the same measurement using the stiffer tip (type B), is shown in **Figure B.2.c**. In this case, as calculated through the histograms (**Figures B.2.b** and **B.2.d**), the observed contrast between domains reaches roughly 100 Hz using a soft tip

of type A, and rises up to 1.38 kHz, when a stiffer tip is used. Both in single crystals and thin films, besides the size effect based on the dimensions of the ferroelectric samples discussed in **Section 3.4**, it is demonstrated that the mechanical contrast enhances when a stiffer tip is used. These results prove the above-mentioned hypothesis; when the spring constant of the cantilever is lower than the effective stiffness k^* , then most of the energy that should be transferred to excite the contact and the sample is dissipated at the soft cantilever and the probe becomes less sensitive to any sample changes. In other words, the sensitivity of the mechanical reading of ferroelectric polarization by CR-AFM can be strongly improved by choosing the cantilever highest possible cantilever stiffness within the appropriate range.

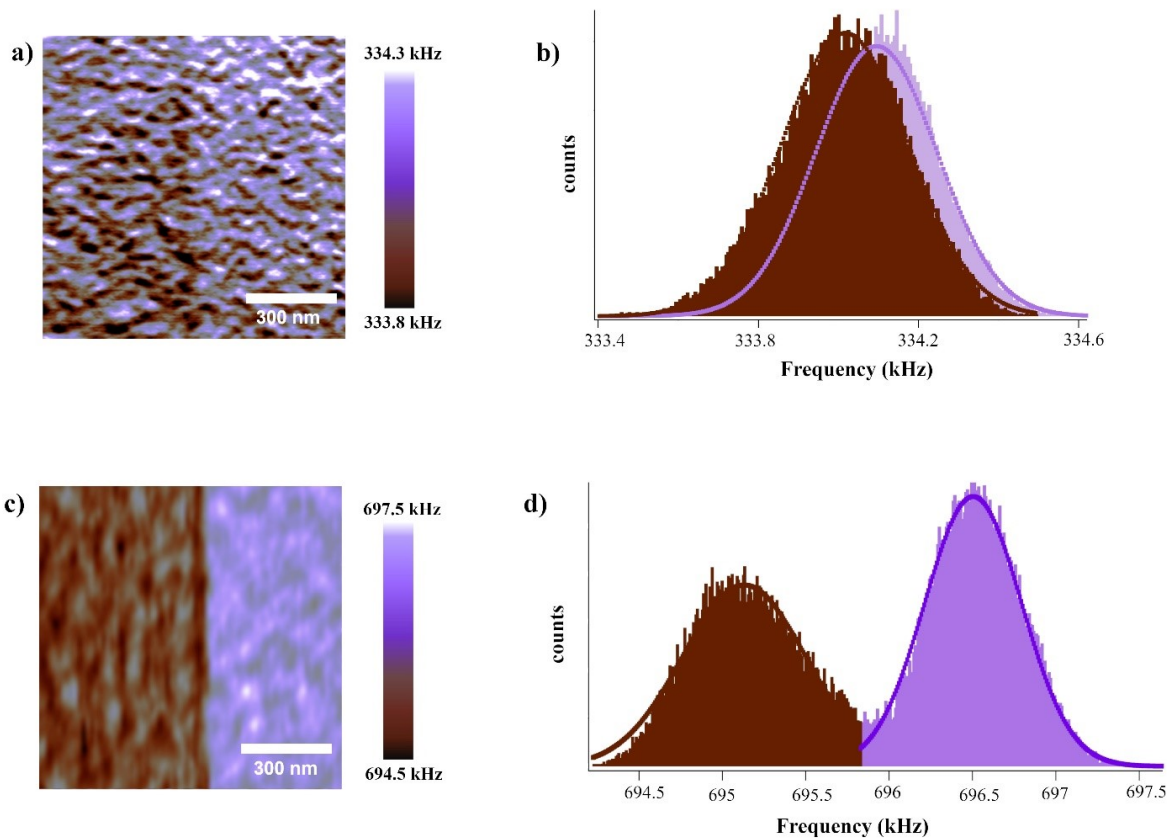


Figure B.2: CRF image of PbTiO_3 thin film grown on SrTiO_3 substrate with thickness of 50 nm, as measured by a soft AFM tip (PPP-EFM, Nanosensors). c) CR-AFM image of the same area of the material as measured by a stiff AFM tip (PPP-NCL Nanosensors) under the same applied force (900 nN) in both cases. The corresponding histograms demonstrate shift in resonance frequency of opposite polarized domains of 100 Hz for soft tips (b) and 1.38 kHz for a stiff tip (d)

References

- [1] U. Rabe, S. Amelio, M. Kopycinska, S. Hirsekorn, M. Kempf, M. Göken, W. Arnold "Imaging and measurement of local mechanical material properties by atomic force acoustic microscopy", *Surf. Interface Anal.* 33(2) (2002).
- [2] V. Nagarajan, J. Junquera, J.Q. He, C.L. Jia, R. Waser, K. Lee, Y.K. Kim, S. Baik, T. Zhao, R. Ramesh, P. Ghosez, K.M. Rabe "Scaling of structure and electrical properties in ultrathin epitaxial ferroelectric heterostructures", *J. Appl. Phys.* 100(5) (2006).
- [3] W.C. Oliver, F.R. Brotzen "On the generality of the relationship among contact stiffness, contact area, and elastic modulus during indentation", *J. Mater. Res.* 7(3) (1992).
- [4] U. Rabe, W. Arnold "Atomic force microscopy at MHz frequencies", *Ann. Phys.* 506(7–8) (1994).
- [5] D.C. Hurley "Contact Resonance Force Microscopy Techniques for Nanomechanical Measurements", *Applied Scanning Probe Methods XI: Scanning Probe Microscopy Techniques*, Springer Berlin Heidelberg, Berlin, Heidelberg, 2009, pp. .
- [6] J.A. Turner, S. Hirsekorn, U. Rabe, W. Arnold "High-frequency response of atomic-force microscope cantilevers", *J. Appl. Phys.* 82(3) (1997).

